Università degli Studi di Ferrara

DOTTORATO DI RICERCA IN
SCIENZE DELLA TERRA

CICLO XXII

COORDINATORE Prof. Beccaluva Luigi

Complete Waveform Inversion Approach To Seismic Surface Waves
And Adjoint Active Surfaces

Settore Scientifico Disciplinare GEO/11

Dottorando	**Tutore**
Dott. Bignardi Samuel	Prof. Santarato Giovanni
_____	_____
(firma)	*(firma)*

Co-Tutore
Prof. Fedele Francesco

Anni 2008/2010

To Silvia . .
To Blek . . .
To All My Family.

Acknowledgements

This section of the dissertation is perhaps the most difficult to write. It is extremely clear in my mind how much I learned from everyone who directly or indirectly collaborated with me during this research effort. There are many people I wish to acknowledge.

To my advisor Prof. Santarato goes my gratitude for guiding me with his suggestions. I am always admired from his experience in Geophysics. His encouragement to spend a period in USA is at the origin of all I was able achieve. Indeed I am grateful to him for trusting my skills and for letting me work all the time I needed to develop and complete this work. Sincere gratitude goes to Prof. Nasser Abu-Zheid for all explanations he gave me on the practical aspects of surface wave testing and more in general on non-invasive investigations.

The period I spent at the Georgia Institute of Technology has meant to me a huge development both professional and personal. I had the chance to work with many brilliant scientists, among them I wish to Acknowledge Prof. Glenn J. Rix for the Scientific collaboration started, for his availability and warm hospitality.

A world of gratitude goes to Prof. Anthony Yezzi and Prof. Francesco Fedele whom I consider good friends in first place. I can say that Prof. Yezzi, during his lectures at the GaTech made me love Mathematics even more than I thought was ever possible. His rigorous approach will remain in my mind as an example to follow. I have to thanks him not only from the scientific point of view but also because he made me to appreciate a lot of small things I had never noted before. Prof. Fedele is perhaps the hardest worker I ever met. He taught me that it does not exist a problem that cannot be solved and actually I repeat the same to myself every time I encounter some difficulties studying something. He was positive, encouraging and full of enthusiasm. Prof. Fedele told once me that, at least once in your life you need to meet that professor who is able to open your mind. I think that with Prof. Yezzi and Prof. Fedele I met two of those. I want to thanks Robin Yezzi, first of all for her warm hospitality and her friendship, second for the help received with the grammar, during the final edit of this text. I cannot forget to thank Keary D. Williams for his availability, hospitality and friendship during all the period I spent in Atlanta.

Abstract

The idea to exploit the dispersive mechanism of surface waves as a probing tool for investigating subsurface structure was introduced about 30 years ago, and afterwards a very intense research field has developed. Currently many methods known generally as Surface Wave Methods exist, and are well established, most of them assuming layered or depth dependent ground models. In most cases the parallel layer assumption is correct because the soil structure is expected to negligibly depart from a layered structure at a typical surface testing scale for engineering and geotechnical purposes however to exploit the amount of information achievable, it is necessary to extend the research, relaxing at least one of the underlying model assumptions. Indeed in classical SWM's, surface waves are assumed to be Rayleigh waves, this means that a parallel layered model has been implicitly assumed. As a consequence search for a soil model geometry other than the assumed one can only result in slight perturbations. The only possible deduction is that overcoming limitations of layered models requires to exploit P and S waves which are indeed general solutions of the elastodynamic problem. Geometry can then be retrived by a complete waveform inversion based on a forward model capable of successfully reproducing all of the features of the displacement field in presence of complex scattering phenomena. In this research effort an inversion approach has been introduced which exploits the Boundary Element Method as forward model. Such approach is appealing from a theoretical point of view and is computationally efficient. Although in the present work a monochromatic signal traveling in a system constituted by a layer over an half space was investigated, this method is suitable for any number of layers, and multi-frequency environments. The boundary element approach can be easily generalized to three-dimensional modeling; moreover viscoelasticity can be introduced by the elastic-viscoelastic principle of correspondence. Finally BEM can be easily implemented for parallel computing architecture. Synthetic cases of high and low impedance Jump were investigated for typical SWM setups and a first example of application on real data was performed. Finally an elegant analytic form of the minimization flow named Adjoint Active Surfaces was obtained combining Computer Vision technique of Active surfaces and the Adjoint Field method.

Contents

List of Figures

List of Tables

Chapter 1

Introduction.

Recent attention concerning terrestrial events has highlighted the need to protect populations against seismic hazard. Intuitively, it may appear that only seismogenic regions are prone to the damaging effects of earthquakes, but observations of catastrophic damages far from earthquake epicenters or connected with relatively low energetic earthquakes has focused the attention on site effect also for apparently quiet regions. Consequently, seismic risk must be evaluated in order to prevent potential loss. Seismic risk is in fact the evaluation of the expected damages produced by a seismic event, in terms of structure, equipment, or business interruption.
One aspect of this rather complex process of evaluation is the subdivision of a potential seismic or earthquake prone area into zones with respect to site effects, so that seismic hazards at different locations within the area can correctly be identified. This last process, known as seismic microzonation,is actually the final step of the ground response analysis, whose primary goal is the prediction of the free field response induced by catastrophic events originated by seismic energy being released in the interior of the rigid Earth. The complexity of the problem requires contributions from disciplines like Seismic Engineering, Structural Geology and Geophysics on a joint pursuit to properly model the various aspects of the problem, from rupture mechanism, seismic waves propagation, to local site effects.

Studying a site response requires a double approach. From one side, field investigations are necessary to estimate the values of the key parameters of the subsurface model. Experimental evidence shows that local effects are tightly bounded to jumps in acoustic impedance of the soil. Structures where a soft material layer lies over an hard bedrock as in the case of top soil over granite, have been recognized as a classically dangerous configurations. Seismic waves traveling through these kinds of

structures meet a jump in soil properties, summarized by the acoustic impedance $Z = \rho V$. As it is well known from physics, waves facing a media discontinuity can be both reflected or refracted. Coefficients of reflection and transmission can be expressed as functions of acoustic impedance. In the case of normal incidence, their dependence on acoustic impedance contrast is quite simple and when $V_{Bedrock} \gg V_{Layer}$ the reflection coefficient is close to one.

In this case, waves traveling in the upper layer toward the interface are almost completely back-reflected and seismic energy is trapped inside the layer. This leads to specific frequencies, ω_r, to constructive interference and a resonance phenomenon, which results in amplification of particle displacement and acceleration at the surface. Generally shear waves cause most of the damage because they propagate stresses able to " cut " structures. For shear wave velocity, $V_S = \sqrt{\mu/\rho}$ a two-layer model with infinitely rigid bedrock, a well known relation holds (sec. 2.17):

$$f_r = \frac{V_S}{4H}(2n - 1) \qquad n = 1, 2, 3, \ldots \infty \qquad (1.1)$$

This clearly indicates the key role played by the shear wave velocity and, in its turn, from the shear wave modulus. It is not surprising that perhaps the most used among parameters to evaluate amplification and resonance of particle motion is the average shear velocity of the first tens meters of depth. Many legislations, including the Italian one, have adopted a depth of 30 m in order to estimate that average value (V_{S30}). Soil parameters have been evaluated from geotechnics with many methods, direct probing, boreholes or ground penetrating cone are probably the most popular approaches. Nevertheless recently non-invasive methods were developed to both extend the punctual geotechnical information and to get the subsurface response where geotechnical methods can not be applied. Finally, non-invasive methods are generally much less expensive which makes them advantageous to employ for gathering data. Among non-invasive testing, the most effective methods to recover information on the shear wave velocity profile vs. depth are those based on the study of surface waves (SWM). In fact SWM includes a whole family of different techniques which share the dispersion of surface waves as the base mechanism.

SWM techniques were developed in the 1980s, but they didn't become popular until after 1990. Today they are widely exploited worldwide to estimate the site response in areas prone to seismic hazard. In general they allow researchers to obtain the 1D layered profile of shear wave velocity. Once the V_S profile has been estimated and the local structure at a site has been discerned in sufficient detail, the dynamic response of the site can be simulated in order to obtain the amplification pattern for

a "project earthquake". This task is usually accomplished by means of numerical simulations and popular software can be cited here, such as SHAKE, in its various versions, EERA, NERA, Deepsoil and other. The collection of source programs by R.B.Herrmann is also popular.

It must be emphasized that between field data and response simulations, the recognition of subsoil properties plays a central role. Among the wide class of software exploited in Geophysics and Geology, here the interest is focused on the class of applications whose purpose is to extract structural information from field data, i.e. to solve the inverse problem. In the modeling stage some different aspects are worthy to be investigated. The first classification is based on the scale of involved distances. A model can be built for long distances in order, for example, to investigate propagation of waves from an earthquake, aiming at the study of the Earth structure. Estimating the structure of the lithosphere, by studying the features of seismograms, belongs to this kind of modeling (Jeffreys & Bullen, 1940; Dziewonski and Anderson, 1981; Kennett & Engdahl, 1991).
On the other hand, reduced scale models can be exploited to simulate regional effects, as for example the scattering pattern in an alluvial valley (Aki, 1988; Bard, 1994) and even more at Engineering/Geotechnical scale, to investigate vibration insulation, soil-structure interactions, etc. (Manolis & Beskos, 1988). Soil can be conceptualized exploiting various approaches. For example, in a geometric setting as a first approximation it is relatively straightforward to model the ground as an half space (Rayleigh explored this model in 1885). Then the need to take into account more complicated, albeit more realistic, features, led researcher to consider piecewise layers or a functional variation of the involved parameters on an otherwise 1D layering (Schnabel *et al.*, 1972; Vucetic, 1986; Idriss *et al.*, 1973; Lysmer *et al.*, 1971), to account for different characteristics on different portions of the subsurface. For the sake of simplicity and to obtain analytic solutions these variations are commonly applied to an only 1D earth. By choosing to forgo methods to obtain an elegant analytic solution, numerical methods such as Finite Element Method (FEM) or Boundary Element Method (BEM) can be exploited, which mesh the soil surface/volume and enable the problem to be solved numerically. As will be described in detail in the subsequent sections, there are assumptions that affect how the model can mimic the underlying physics. In fact, whenever soil constituting materials have to be described, they can be modeled starting from their grained nature, which entails a discrete mechanics approach, or, since wave motion is a phenomenon that usually occurs at a greater scale than particle size, soil materials can be postulated to be a continuum. This latter assumption, after Cauchy in 19[Th], gave origin to modern

solid mechanics. Finally, it can be stated that in continuum mechanics both Eulerian and Lagrangian approaches are possible.

A consequence of the above considerations is that a wide range of models are possible, each one with its own field of application. The modeling effort of this work can in fact be located in the frame of continuum mechanics. Media are assumed to be in regime of very small to small strain, as these terms are defined in sec. 2.2. Isotropy and piecewise homogeneity are also assumed.

1.1   Research objectives

The idea to exploit the dispersive mechanism of surface waves as a probing tool for subsurface structure was introduced about 30 years ago, an historical overview can be found in Park and Ryden (2007), and afterwards a very intense research field has developed. In fact, knowledge of surface waves was highly advanced several years before (Aki and Richards, 1957), but only after 1990 it was intensively developed for engineering and structural purposes. Currently many methods exist, most of them assuming layered or depth dependent ground models, which employ information contained in Rayleigh and Love surface waves to obtain shear wave velocity profiles. General assumptions of these methods are:

- Small Strain Environment.

- Plane Surface.

- Plane Layered Geometry.

- Piecewise or functionally variation of soil elastic parameter with depth.

- Media Elasticity.

- Media Homogeneity.

- Media Isotropy.

Methods based on surface waves analysis are well established, as 1D layered earth and waveguide behaviors are almost fully understood. However, an observation should be made about SWM; these methods are stable and a Vs profile of the subsoil is always obtained. Actually the obtained profile is the layered equivalent of the true situation. In most cases the parallel layer assumption is correct because the soil structure is

expected to negligibly depart from a layered structure at a typical surface testing scale for engineering and geotechnical purposes (few tens of meters). The drawback is that data processing doesn't give any indications about the true subsurface structure, although very recently some progress has been made on this topic (Strobbia & Foti, 2006). As a result, the parallel layer assumption can be very inaccurate when locally complex structures are involved.

To exploit the amount of information achievable, it is necessary to extend the research, relaxing at least one of the above assumptions. Most of reported evidence arises from observation of earthquake damages. It could be objected that scales, at which the geometry of the subsurface structure contributes to the strength of the event, are several orders of magnitude larger than a typical SWM investigation and that at local scale the subsoil can be safely approximated with parallel layer models. Unfortunately the issue is not within scale range, since scattering effects occur at every scale being the ratio λ/d of wavelength λ versus the scatterer dimension d, the most important parameter.

Another issue that must be taken into account is that the assumption of the parallel layers model virtually forbids applications of SWM when the soil is evidently non-planar.

In Conclusion, the goal proposed at the beginning of this research effort was to investigate the possibility of exploiting surface waves recorded in some way at the soil surface and relaxing the constraint of parallel layered structure. To this end an inversion scheme was necessary to invert the data and to obtain the model characteristics, which now were not only elastic media properties but also geometric properties. To build an inversion algorithm requires minimization of an objective function. As a "natural" choice, this coincides with the difference, in the least squares sense, between data and corresponding calculated quantities. It was intuitive to consider as "data" seismograms, but a forward model was necessary to simulate displacements at receivers. On this respect, Fourier space analysis seemed the most effective way since time dependence factors out and complex scattering can be analyzed frequency by frequency independently.

A first semi-analytic attempt has been made for horizontal shear waves which started from the solution of the parallel layer problem at a fixed frequency. For simplicity, the method was implemented for a layer over a half space. The 2D subsoil model was then discretized along the horizontal direction and displacements were

assumed to be a separable function of the coordinates. The depth dependent part of the displacement at each horizontal position was expanded into a linear combination of modal solutions of the local parallel model. The lateral variation was then introduced matching all slices and exploiting an unknown horizontally varying weighting function. This function was obtained semi-analytically by joining the elegant approach of Lagrangian minimization and the numeric spectral method. The tentative model was able to reproduce results of parallel layered environment, and was proved to be effective for interface slopes lower than 20 degrees. This result, despite it generalizing previous work (Gjevic, 1973) by introducing features such as back-reflections, multimodal nature of Love waves, and extending the slopes range beyond the domain of small interface perturbations, was not suitable for inversion and moreover its generalization to Rayleigh waves was too complicate. The method is reported for sake of completeness in sec. 4.2.

A second forward model was then successfully built exploiting the BEM. Motivations about this selection will be fully illustrated in section 4.3.

Finally both forward and inverse procedures were completed, successfully inverting a real set of surface waves data and therefore a novel approach to surface waves data interpretation can be introduced. Consider an initially layered soil structure with piecewise elastic parameters and densities. Data on the surface are compared with the numerical prediction of BEM in a least squares sense and the resulting objective function is minimized allowing the shape of the layers to change. At this stage, constitutive parameters ρ_i, V_{Si}, V_{Pi} are assumed to be known at least in one point of the profile, which means that this information comes from other data (e.g. geotechnical tests). In future developments, a coupled inversion of both shapes of layers and elastic parameters could be implemented, which will be independent on this "a priori" information.

1.2   Dissertation outline

In the proceeding chapters, section 2 is devoted to recall the behavior of real materials and some phenomenological aspect of waves due to underlying geometry of a site.
Section 3 outlines currently popular methods of investigation that exploit surface waves as a main probing mechanism. The main and original part of the present work will begin on chapter 4 where section 4.1 introduces some useful elastodynamic concepts, sec 4.2 and sec. 4.3 introduce respectively the first attempt of forward

model and the final solution adopted to model the elastic wavefield.

Chapter 5 outlines inversion theory and introduces the concept of shape sensitivity. When an inversion algorithm is built, sensitivities of the displacements calculated at receivers due to a change in one point of the discretized buried interface must be calculated and collected in a Jacobian matrix J. Simulated inversions of synthetic data with numerically evaluated J matrix are presented in section 5.2.

Chapter 5.3 will describe a real data application.

Finally, chapter 6 proposes a new multidisciplinary approach. Computer vision concepts introduced only during the last fifteen years are exploited to obtain an inversion algorithm which speeds up computation dramatically.

Sec. 7 not only summarizes the obtained results, but also contains conclusive considerations and a possible perspective of the research.

Chapter 2

Phenomenological aspects.

2.1 Introduction

As it is well known, a modeling process involves simplifications of complex natural phenomena in order to obtain the simplest framework that still retain the " almost intact" the major characteristics of the real environment. In this process of simplifications some assumptions have to be made. In the proceeding sections, some aspects of real soil systems will be considered. This chapter is intended to provide the reader with an overview of some phenomenological aspects which will be useful to understand limitations introduced in classical surface wave approach.

2.2 Dynamic behavior of material

As stated in the preceding section, modeling the soil response requires some assumptions on the constitutive model. The first aspect to be taken into account is how to model the behavior of a material crossed by seismic waves. Investigations on the factors affecting dynamic behavior of material have been conducted during the last 40 years both in the field and laboratory, and detailed classification of the effects of different parameters are available (Vinale *et al.* 1996). A first classification divides parameters influencing materials as intrinsic, proper of the material structure, as for example, granulometry, plasticity, texture and cementation. The so-called state parameters belong in the second class, e.g. effective stress of confinement, stress/strain ratio, stress/strain magnitude, and stress/strain history.

2.2.1   External influence parameters

The second class is of particular interest here. Since cyclic deformations are induced in materials perturbed by seismic wave motion, it is interesting to consider the response of a sample volume in a controlled condition of cyclic strain. For a process of charge-discharge-recharge, the tangential deformation with the aid of only two parameters, i.e. *shear modulus* G and *damping ratio* D, can fully represent the mechanical behavior of the sample. These parameters [1] will be indicated here with $arctgG_0$, $arctgG$
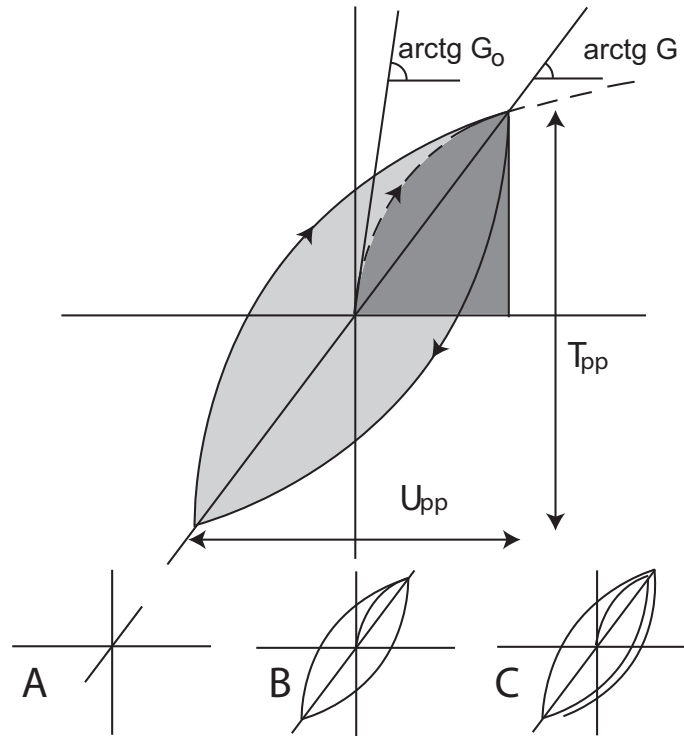
Figure 2.1: Charge-discharge-recharge cycle:
A) Very small strain,
B) Small strain,
C) Intermediate strain.
W_D = light gray., W_s = dark gray.

---

[1]Notation about shear modulus in literature is a little bit confusing. It is indicated with G in Engineering and it coincides with μ Lamé's constant in Physics and Geology

$$G = \frac{T_{pp}}{U_{pp}} \quad (2.1)$$

$$D = \frac{W_D}{4\pi W_S} . \quad (2.2)$$

With reference to fig. 2.2.1, four contiguous classes of mechanical behavior can be identified.

Very small strain

It is the region defined for values of strain smaller than the *linear cyclic shear strain threshold* γ_l. It is characterized by a constant shear modulus $G = G_0$. Within this region the response of the material is linear. Despite the very low strain range, the behavior is not really elastic and the area of the stress-strain loop is not null; nonetheless the cyclic process occurs with dissipated energy close to zero and material behavior is almost perfectly elastic. This weakly hysteric behavior is due to a time lag between the driving strain and the consequent driven stress and is of elasto-plastic type. Values of γ_l vary from material to material, and can range between 0.0001 and 0.01%

Small Strain

Limits γ_l γ_v , where γ_v is the *volumetric shear strain threshold* and is usually one or two orders of magnitude greater; it encloses a region of deformations where behavior is fairly non-linear and dissipative. The stress-strain curve changes as in figure 2.2.1 and dissipated energy can be determined with equations 2.1.

Despite this fact, the mechanic behavior still remains stable with only an initial small degradation. The subsequent behavior remains independent on the history of the material and on the number of cycles. This range is known as material hardening (or softening).

Intermediate strain

Threshold γ_{pf} identifies the next class. Shear and volumetric strains couple and at any cycle in the stress-strain curve a residual deformation always remains. The sample degrades with the number of cycles and energy losses take place over finite periods of time, due to irrecoverable damages to the internal microstructure.

Large strain

When γ_{pf} is exceeded, the sample enters the large strain domain and it is only matter

of time to reach the material failure, which occurs at γ_f threshold.

It must be noted that mentioned thresholds are usually related to laboratory samples which are usually perturbed with respect to the undisturbed field soil; moreover soil parameters are also dependent on the applied stress history, which implies that by investigating samples with different histories, different values of G and D could be obtained. Nonetheless thresholds still remains very useful concept to classify the dynamic behavior of the material.

2.2.2   State parameters

Stiffness and damping ratio have been proved able to characterize the dynamic behavior of the material under investigation. As will be shown in section 2.5, during wave propagation both very small and small strain can be formally described just replacing the real wave speed with its complex analogous. Using these two main parameters is expected to characterize soil behavior in modeling. This approach is commonly accepted and soil parameters are usually assumed constant. However for sake of completeness, it is noteworthy that both G and D are in general functions of the physical characteristics of the media. Recalling fig. 2.2.1 and eq. 2.1, there is an intimate relation between G, D parameters, strain thresholds and energy dissipated. The physical phenomena affecting the former, will also affect the latter one. Earlier descriptions of stiffness dependency were expressed as the following empirical relations (Nardini, 1978):

$$\frac{G_0}{P_a} = Sf(e)\left(\frac{P'}{P_a}\right)^n OCR^k\,, \tag{2.3}$$

where S is the a-dimensional stiffness coefficient which accounts for the soil microstructure, f_e is a decreasing function of void index and it depends on initial consolidation conditions; n, k are empirical indexes accounting for sensitivity of the stiffness with respect to effective stress of confinement and to the degree of consolidation; P_a is the reference pressure which makes eq.2.3 dimensional. Finally, Over Consolidation Ratio (OCR) is defined as the highest stress experienced divided by the current stress.
Eq. 2.3 was then expressible in simplified form depending on particles dimension. This approach was based on subdivision of soils types into coarse and fine-grained and to specialize eq. 2.3 for the two cases. Later works (Dobry & Vucetic, 1987; Vucetic & Dobry, 1991; Jamilkowski *et al.*, 1991; Vucetic, 1994) recognized this subdivision as unnecessary and unified the phenomenological representation exploiting

the plasticity index (PI). Figure 2.2 illustrates the behavior of thresholds with respect to PI.

Finally, within this more recent description frame, the main state parameters and
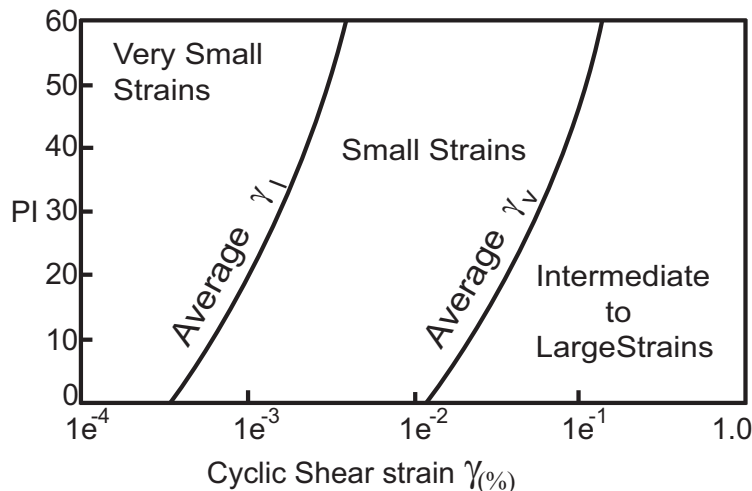
Figure 2.2: Strain thresholds as function of Plasticity Index, (Vucetic, 1994)

their effects on stiffness and Entropy density production can be summarized in tables 2.1 and table 2.2 (Lai, C.G., 1998)

This research effort is focused on the first of these four regions even if all algorithms, treated in following chapters, can be extended to visco-elastic cases by means of the elastic-viscoelastic principle of equivalence.

2.3 Surface waves

Seismic energy released during an earthquake propagates in soil by means of elastic waves. From a mathematical point of view these can be described by Navier's equation, whose general solutions are P waves, also called "Primary" or "Compressional" where particle motion has the same direction of propagation and S, "Secondary waves" or "Shear waves" where particle motion is perpendicular to the wave direction of propagation. Actually these waves propagate inside the media volume, and for that reason are also called "Body waves". During an earthquake seismograms are recorded and P, S waves correspond respectively to the first and second arrival observed. During propagation their amplitude decreases proportionally to r^2 because

Stiffness reduction			
Parameter	effect		Refs.
Increase in Mean Confining pressure	Increase		[59]
Fabric: (Increase in voids)	Decrease		[55][75]
Increase in Strain-Rate	$\gamma < \gamma_l$	Low PI: No effect High PI: Increase	[31]
	$\gamma > \gamma_l$	Increase	[80]
Increase in Duration	$\gamma < \gamma_l$	Negligible effect for Dry Sand and Clayed soil	[123][79]
	$\gamma > \gamma_l$	Differences between drained and undrained conditions	[31]

Table 2.1: Effects of intrinsic parameters on Stiffness

Entropy density production			
Parameter	effect		Refs.
Increase in Mean Confining pressure	Decrease	(Particularly for low PI)	[59]
Fabric: (Increase in voids)	Decrease		[55][75]
Increase in Strain-Rate	Independent on frequency of cyclic excitation within seismic range (0.001-100 Hz)		[123]
Increasie in Duration	$\gamma < \gamma_l$	Negligible effect for Dry Sand and Clayed soil	[123][79]
	$\gamma > \gamma_l$	Differences between drained and undrained conditions	[31]

Table 2.2: Effects of intrinsic parameters on Entropy production

the initial energy is spread on larger and larger spherical surfaces, while amplitude is proportional to r. However the greatest amplitude coincides to the later arrival of surface waves. Since they travel on surface, their amplitude and transmitted energy decrease respectively like $\sqrt{r}$ and r. For this reason, most damages produced during an earthquake coincide with the passage of this latter kind of waves.

Surface waves have been classified as Rayleigh waves(named for Lord Rayleigh, who predicted the phenomenon in 1885) and Love waves(predicted by the mathematician A.E.H. Love in 1911). Indeed, Rayleigh waves arise from the constructive interference of compressional waves and vertically polarized shear waves. Love waves on the other hand arise from horizontally polarized shear wave self interaction. Characteristics of Love and Rayleigh waves such as amplitude of displacements and phase velocity depends on elastic properties of the propagating media. Rayleigh waves, produces in almost any layered or depth-dependent system. On the contrary, Love waves production requires either an increment or a positive jump with depth of acoustic impedance. Despite this attribute, they actually share two interesting properties, namely, both Love and Rayleigh waves traveling in soil with depth-dependent [2] elastic properties are dispersive and multi-modal.

Latter characteristics are easily explained for Love waves (Aki & Richards, 1980). Rayleigh waves propagation on the other hand, being originated by interference of two different kind of waves is much more complex. The practical motivation to limit the scope to Rayleigh waves is that they are widely exploited in most of the surface wave methods discussed in chapter 3.

Basic properties of Rayleigh waves can be understood following the approach introduced by Lord Rayleigh. Let's consider an elastic, homogeneous and isotropic half space; the wave equation

$$(\lambda + \mu)\nabla\nabla \cdot \mathbf{u} + \mu\nabla^2\mathbf{u} + \rho\mathbf{f} = \rho\ddot{\mathbf{u}}, \qquad (2.4)$$

can be solved introducing Helmholtz's decomposition. Free surface boundary conditions and radiative condition at infinity are introduced as well (Richart *et al.*, 1970). If the case of plain strain is assumed (sec. 4.1) the *characteristic Rayleigh equation* 2.5 is obtained

$$K^6 - 8K^4 + \left(24 - 16\gamma^2\right)K^2 + 16\left(\gamma^2 - 1\right) = 0, \qquad (2.5)$$

---

[2]If an elastic, homogeneous, isotropic half-space is considered, Rayleigh waves with different frequency travel with the same velocity and dispersion does not occur. Love waves, on the other hand, cannot produce in such environment.

P wave

Compressions   Undisturbed Medium

Dilatations

S wave

←Wavelength→

Love wave

Rayleigh wave

Direction of Propagation
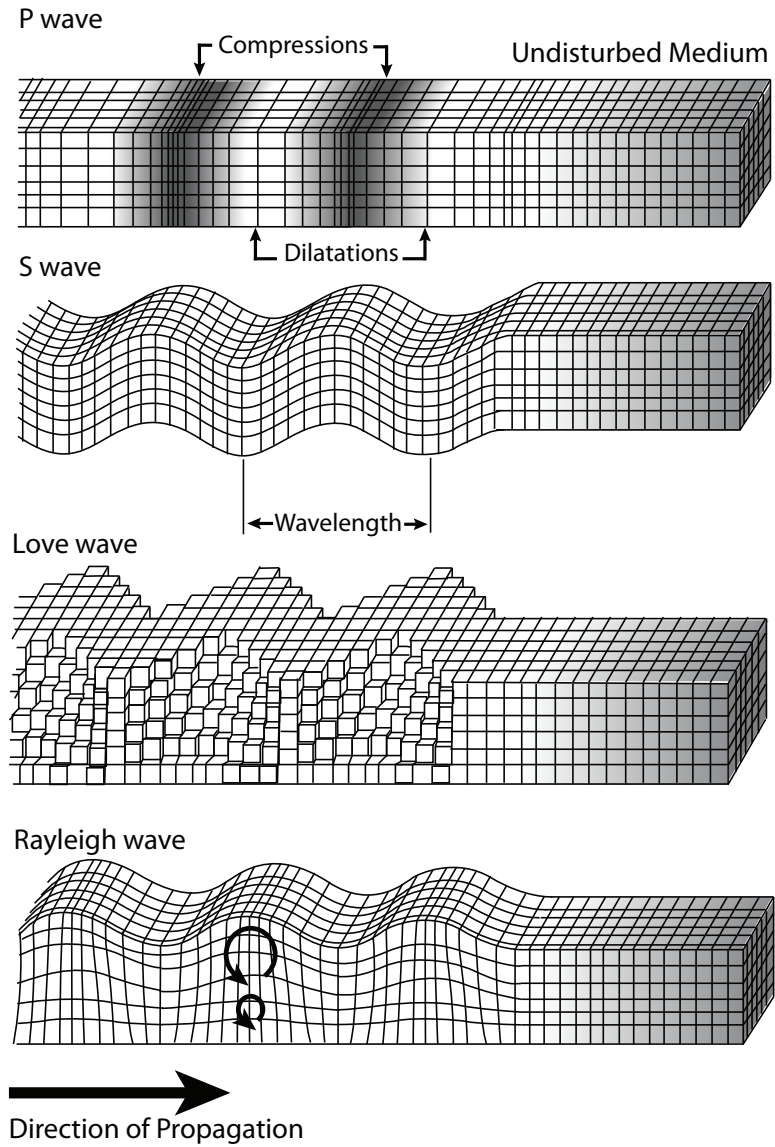
Figure 2.3: Example of P, S, Love and Rayleigh particle displacements (Bolt, 1976)

where $K = V_R/V_S$ and $\gamma = V_S/V_p$ are ratios involving shear, compressive and Rayleigh wave velocities. The latter equation can be solved for K^2 and its roots are a function of the Poisson's ratio. It can be shown that for real media only one root exists and an approximate value is given by (Viktorov,1967)

$$K = \frac{0.87 + 1.12\,\nu}{1 + \nu}\,. \tag{2.6}$$

This leads for values of Poisson's ratios $0 < \nu < 0.5$ to

$$0.87 < V_R/V_S < 0.96\,. \tag{2.7}$$

Assuming far field conditions, displacements can be evaluated and the solution takes the form

$$u_z \propto \frac{b_z}{\sqrt{r}}\,e^{\left(\omega t - kr - \frac{\pi}{4}\right)} \tag{2.8}$$

$$u_r \propto \frac{b_r}{\sqrt{r}}\,e^{\left(\omega t - kr + \frac{\pi}{4}\right)}\,,$$

here u_z, u_r are respectively vertical and radial displacements; b_z, b_r are two functions of mechanical parameters. Further, wavenumber is connected to the velocity by the relation $k = \omega/V_R$. Displacements are depicted in fig 2.4

This simple model expresses some basic features of Rayleigh waves. First of all, the unique root of the characteristic equation 2.5 depends only on ν and not on the frequency; as a consequence, propagation in an elastic half-space is not dispersive. Solution 2.8 shows that there is a $\pi/2$ phase shift between components which leads to an elliptic retrograde motion of surface particles. Displacements are indeed a superposition of a horizontal and a vertical component which propagate with the same velocity, but with different exponential attenuation laws with depth. Consequently motion affects only the shallow portion of material for a depth comparable to one wavelength. Further the retrograde motion is reversed at a depth close to a quarter wavelength.

Formulation become much more complex if mechanical properties of the media are function of depth. In this situation Navier's equation is expressed by

$$(\lambda + \mu)\nabla\nabla\cdot\mathbf{u} + \mu\nabla^2\mathbf{u} + \boldsymbol{e}_j\frac{d\lambda}{dz}\nabla\cdot\mathbf{u} + \frac{d\mu}{dz}\left(\boldsymbol{e}_j \times \nabla \times \mathbf{u} + 2\frac{\partial\mathbf{u}}{\partial z}\right) = \rho\ddot{\mathbf{u}}\,. \tag{2.9}$$

It can be shown that by assuming plain strain and an exponential form of displacement, the elastodynamic problem constituted by eq. 2.9 and above mentioned
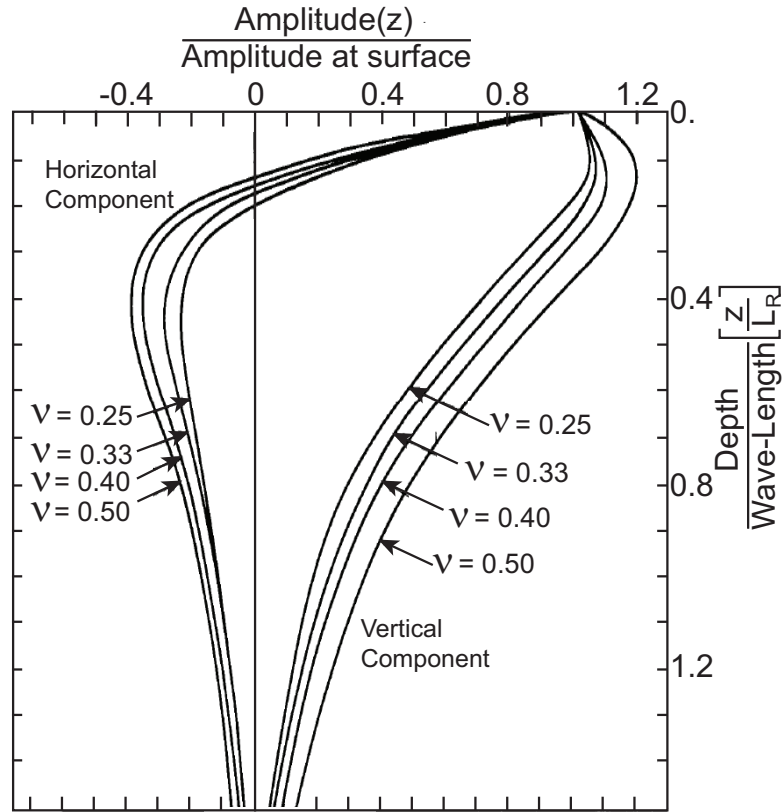
Figure 2.4: Displacements of Rayleigh waves.(Richart *et al.*,1970)

boundary conditions, reduces to an eigenvalues problem. The generalized character-
istic equation is solved once the roots $K(\omega)$ are found. It is noteworthy that now
different modes of propagation exist and they travel with different speed. In general
Rayleigh propagation in vertically heterogeneous media can be solved once the law
of variation of elastic parameters is specified. Due to the impossibility of solving the
problem analytically, different numerical methods have been developed. Some numer-
ical methods of note are the Transfer-Matrix method introduced by Thomson (1950),
and successively improved by Haskell (1953); the Stiffness-Matrix method (Kausel
and Roesset, 1981) and alternative approaches (Kennett 1974, 1979; Kerry, 1981).
Rayleigh waves have been thoroughly investigated and general conclusions can be
summarized.

- The geometrical dispersion phenomenon can be seen as an effect of the depth-

dependent heterogeneity. Given a packet of Rayleigh waves, since wavelength is related to frequency f by the relation $\lambda_R = V_R/f$, high frequency waves sample the shallower soil portion. On the other hand, low frequency waves penetrates deeper into the media and as a consequence their velocity is influenced by both shallow and deep material's mechanical properties. As a consequence the velocity is a function of frequency. It is noteworthy that the shape of the
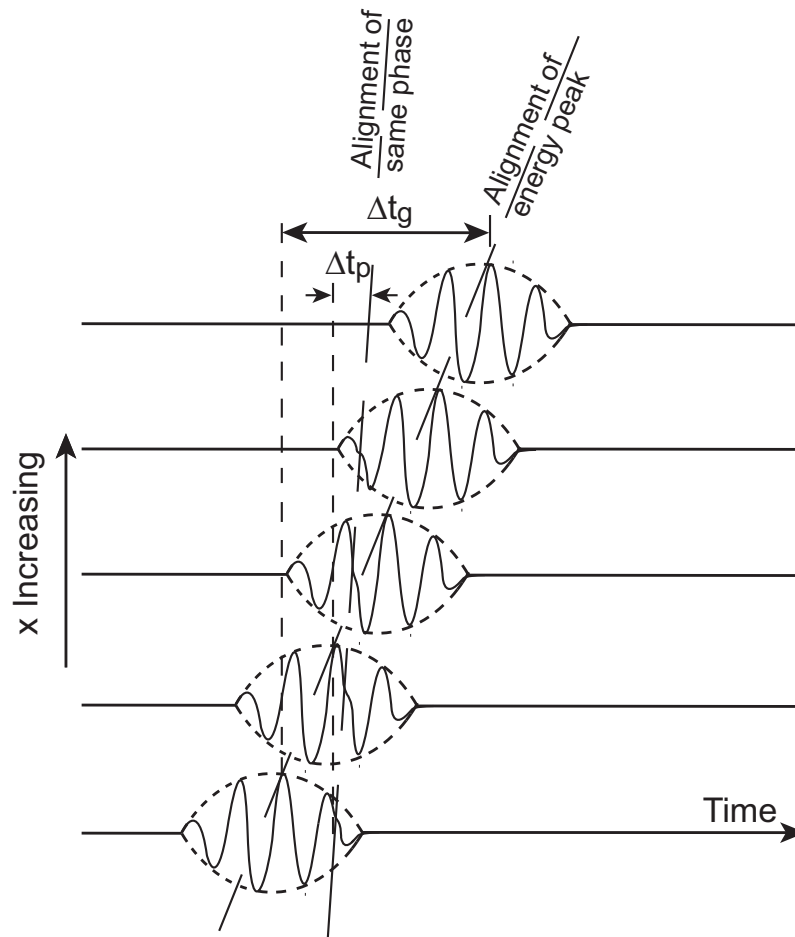
Figure 2.5: Example of dispersion.(Sheriff and Geldart,1995)

dispersion curve, which expresses phase velocity as a function of frequency, is strongly related to the stiffness depth variation. Technically speaking, soils with stiffness increasing with depth are defined as *normally dispersive*, and the opposite is referred to as *inversely dispersive*.

- At fixed frequency many modes of propagation exist with different velocities. It is not possible "a priori" to deduce which mode carries the most part of energy and usually for the same system setup this depends on the frequency (Gukunski & Wood, 1992). However for normally dispersive soils the fundamental mode is usually the most probable candidate.

- The elliptic path of particles is affected from mechanical parameters as well. Elliptic shape is conserved, but in some cases it can be in a prograde sense. The phase shift between components can be different from $\pi/2$ due to dispersive phenomena resulting with axis of elliptic path not necessarily parallel to main reference axis.

- Velocity of a wave packet (group velocity; V_g) is usually different with respect to the phase velocity (velocity of a fixed frequency wave in the packet V_{ph}).

$$V_g = \frac{d\omega}{dk(\omega)} \approx V_{ph} + f\frac{dV_{ph}}{df} \,. \qquad (2.10)$$

Figure 2.5 depicts a typical dispersive phenomenon, where

$$\begin{aligned} V_g &= \frac{\Delta x}{\Delta t_g} \\ V_{ph} &= \frac{\Delta x}{\Delta t_p} \,. \end{aligned}$$

2.4   Topographic effects on wave propagation

It is well known that local topographic features can severely affect the pattern of an incident wavefield. The most striking evidence of these characteristics of wave propagation comes from the observation of damages produced during catastrophic earthquakes. Observation of damage localization after an earthquake suggests that the influence of superficial geometry is particularly strong at the top of reliefs. This phenomenon is due to focalization of seismic waves by the free surface in proximity of the relief edge and to constructive interference between direct and reflected wavefield (Bard, 1982). Experimental investigations are usually limited to seismogram analysis where it is difficult to discern between topographic effects and acoustic impedance variations. On the contrary, model investigation has been a extensive field of research.

Analytical solutions exist (Trifunac, 1971; Wong and Trifunac, 1974), finite-difference, finite-element, and boundary-element numerical methods (Sánchez-Sesma

and Esquivel, 1979; Bard and Bouchon, 1980a, b, 1985; Dravinski, 1983; Bravo *et al.*, 1988; Sánchez-Sesma *et al.*, 1989, Geli *et al.*, 1988; Sánchez-Sesma and Campillo, 1993; Bouchon *et al.*, 1996) or approximate analytical methods (Hudson, 1967; Sabina and Willis, 1975) have been used to model topographic effects.

Some more recent investigations have affirmed once again the importance of these features (Raptakis et al., 2000; Bouckovalas and Kouretzis, 2001; Assimaki and Kausel, 2007). The effort was focused mainly on two-dimensional problems since a three-dimensional investigation involves a much more complicated mathematical and computational effort. The "hill" problem has been extensively investigated especially when it is semi-sine shaped. This configuration is particularly suitable for simulation and widely present in nature. Results regarding hills are often indicated as a function of geometrical parameters, namely height-length ratio or height-wavelength ratio.
For example, Nazari (2010) investigated a sine shaped hill under upward S_H wave propagation. The role of some key parameters, such as the shape ratio, defined as the hill's height (h) to its half width (b), the dimensionless frequency, defined as the height-wavelength ratio and the wavelength was proved to affect amplification at the surface. These results showed that topographic effects are negligible for shape ratios less than 0.1 and for the wave lengths more than eight times larger than hill's width. An increase in shape ratio and dimensionless frequency caused an increase in number of points of de-amplification along the hill's flank with a decrease in de-amplification values for horizontal components of movement. On the other hand an increase in shape ratio and wave length, increased the amplification values at all points for the vertical component of the particle's displacement.

Similar results were published in 1981 by Bard, who investigated P, S_V, S_H amplification on mountains. The amplification amount was found to be much more important for incident S-waves than for P-waves. This fact was actually consistent with the precedent experimental observations (Davis & West, 1973; Griffiths & Bollinger, 1979). Amplification was strongly dependent on characteristics of both the incident waves and the topographic structure. Bard also made some general observations, he noticed that the amplitude spectrum exhibits a rather flat maximum for wavelengths comparable with, or slightly shorter than, the mountain width. Amplification generally decreases with increasing incidence angle; in particular, S_V waves impinging at the critical angle cause a relevant de-amplification at the mountain top. The focusing effect increases with mountain height, and presents a complex dependence on the Poisson ratio. The amplification scheme seemed to be replaced by a de-amplification phenomenon for concave topographies.

Savage (2004) obtained numerical results for Rayleigh waves. He found that for horizontally traveling Rayleigh waves, amplitudes generally increase along ridge flanks up to a maximum at ridge crests. In his model the amplification factor reached 3.8 for an incoming signal of 1 Hz frequency.

Wong (1982) pointed out that the near-surface retrograde motion of Rayleigh waves along the flanks can be addressed for landslide induction.

It must be emphasized that the above findings generally underestimated the real topographic effects because of the three-dimensional nature of the real cases. In spite of the extreme simplicity of the adopted model, these examples clearly show the complex interrelation between kind, direction, frequency and geometric parameters of the incoming wave. Therefore it is not possible to obtain general analytical formulation to relate the factors involved but only a list of guidelines.
In conclusion:

- Seismic motion is amplified at the top of a hill, with respect to its base.

- Top hill amplification depends on the hill's geometrical characteristics, as focalization takes place when incident wavelength has the same order of magnitude of half of the hill base (L).

- Amplification is proportional to H/L rate.

- Interaction between incident and diffracted waves at the hill flank produces fast variations of motion in both amplitude and frequency content, with alternating amplification and de-amplification phenomena.

- Two-dimensional numeric models qualitatively corresponded with data on occurrences of amplification at the top, and complex phenomena at flanks while amplification rates are usually underestimated.

2.5   Alluvial valleys

Amplification effects have also been observed in alluvial valleys as during catastrophic earthquakes. The Mexico City disaster in 1985, for example, belongs to this class. The seismic train produced by the source, roughly 400 km west of Mexico City, produced little damage to the coast and attenuated while entering the inland. Unexpectedly, once it approached the city it suddenly amplified. The Mexico City

shake was severe and in some parts of the city the shaking lasted for several minutes after the wave front passed. Another classic case is the famous seism of Loma Prieta in the Oakland-San Francisco Bay area of northern California. Similar effects have been reported in the Northridge earthquake of southern California. Experimental evidence on alluvial basins elucidated the following phenomenology (Drawinski, 1987; King and Tucker, 1984):

- The response to earthquake motion depends strongly upon the frequency and position of the site within the valley and only weakly on the angle of incidence of the input signal.

- The ratios between the Fourier spectra from soil and the spectra from nearby rock sites, used as a reference, can reach values of apparent amplification up to 10. The behavior is strongly dependent on the frequency and distance of the site from the valley edges.

- The response of a given site presents features which do not depend upon the earthquake location or source characteristics.

- Ground motion varies much more over profiles that span large changes in sediment thickness than over profiles where thickness is almost constant.

Early studies on alluvial valleys suggested that amplification effects are mainly due to a jump in acoustic impedance of the involved media. Resonance effects occur when the frequency of the incident earthquake matches with the natural frequency of a shallow soft layer. By exploiting a simple 1D model this phenomenon can be easily shown. For example, let's consider a 1D wave propagation in a layer over an infinitely rigid bedrock. The complete wave equation 2.11 can be uncoupled exploiting separation of the variables to obtain the one-dimensional wave equation for $f(z)$.

$$\rho \frac{\partial^2 u}{\partial t^2} = G \frac{\partial^2 u}{\partial z^2} . \tag{2.11}$$

Assuming displacement to be represented by

$$u(z,t) = f(z)e^{i\omega t} , \tag{2.12}$$

the general solution for the depth dependent part $f(z)$ corresponds to a linear superposition of opposite propagating waves

$$f(z) = Ae^{i(\frac{\omega}{V_s})z} + Be^{-i(\frac{\omega}{V_s})z} . \tag{2.13}$$

Imposing the free surface condition, corresponding to a condition that the stress tensor timed by unit normal at surface is zero $\boldsymbol{\tau} \cdot \boldsymbol{N} = G\frac{\partial u}{\partial z} = 0$; constants A, B are found to be equal and the final particular solution for displacement is

$$u(z,t) = 2A\cos(\frac{\omega}{V_s}z)e^{i\omega t}\,. \tag{2.14}$$

Transfer function[3] $H_r(\omega)$ of this simple model is obtained calculating the rate of displacements at the top ($z = 0$) with displacements at the layer base ($Z = H$).

$$H_r(\omega) = \frac{2Ae^{i\omega t}}{2A\cos(\frac{\omega}{V_s}H)e^{i\omega t}} = 1/\cos(F)\,, \tag{2.15}$$

where $F = \frac{\omega H}{V_s}$ is called *frequency factor*.
The amplification factor corresponds to $H_r(\omega)$ magnitude, so in this case

$$A_r(\omega) = 1/\left|\cos(F)\right|\,, \tag{2.16}$$

which takes infinite values for periodic values of frequency

$$\omega_r = \frac{V_s}{H}(2n-1)\frac{\pi}{2} \qquad n = 1,2,3,\dots\infty \tag{2.17}$$

$$f_r = \frac{V_s}{4H}(2n-1)\,. \tag{2.18}$$

Frequencies in eq. 2.17 are called *natural* , because they are an intrinsic property of the system. Since $V_s = \sqrt{G/\rho}$ they are affected by all intrinsic and external parameters, discussed in sec. 2.2, which affects the dynamic behavior of the material composing the layer. It is therefore clear how the amplification is tightly bounded to the rise up of standing waves. The above model can be now generalized for the case of a deformable half space. In this case part of the energy is transmitted to the infinite half space and dissipated. It can be shown that the shape of the transfer function is unchanged (Lanzo & Silvestri, 1999), but since now it assumes complex values the amplification is expressed as:

$$A_d(\omega) = 1/\sqrt{\cos^2(F) + \frac{1}{I^2}\sin^2(F)}\,, \tag{2.19}$$

[3]Note that this expression is valid both for displacements and accelerations and is a real function (Roesset, 1970)

which depends now also on the properties of the half space material and $I = \rho^L V_s^L / \rho^{HS} V_s^{HS}$ is the acoustic impedance ratio.

One last generalization can be introduced if the case of a viscoelastic layer is considered. The viscoelasticity assumption introduces a velocity dependent term in the wave equation 2.11, the shape of which changes to

$$\rho \frac{\partial^2 u}{\partial t^2} = G \frac{\partial^2 u}{\partial z^2} + \eta_v \frac{\partial^3 u}{\partial t \partial z^2} , \tag{2.20}$$

and η_v is the *viscosity*, related to the damping ratio of a cyclic excitation by

$$D = \frac{\eta_v \, \omega}{2G} . \tag{2.21}$$

Again, if the general solution has the form 2.12, $f(z)$ must abide by the following equation:

$$(G + i\omega\eta_v) \frac{\partial f(z)}{\partial z} + \rho\omega^2 f(z) . \tag{2.22}$$

Now, it is noteworthy that equations 2.22 and 2.11 present the same functional dependence provided that the *complex shear modulus* $G^* = G(1 + 2iD)$ is introduced. Note that now all previous steps follow without any changes except for the substitution of G with G^*. For the case of an infinite rigid half space, the amplification function is shown in fig. 2.5. For the case of a deformable half space on the other hand, the involved equations are much more complicated and amplification cannot be expressed in a simple form

$$A_d(\omega) = 1/\sqrt{\cos^2(F) + (DF)^2} . \tag{2.23}$$

Due to its simplicity, this classical 1D flat-layer approach has been used extensively by researchers, and in many cases it yielded results in accordance with observations. The informative power of such a simple configuration is incontrovertible, although severe cases such as the Mexico City earthquake demonstrated that it can be seriously inadequate. The effect of replacing the homogeneous layer with a depth-dependent heterogeneous one, is in fact that resonance frequencies are closer and resonance peaks enhanced. In general, it has been achieved that substitution of a depth-increasing stiffness layer with an averaged homogeneous one, entails a serious underestimation of the seismic amplification. Further analysis has been made and can be found in literature. All the modeling effort has been oriented to the direction of numerical computation because of the complexity of the scattering patterns and the basin-specific nature of the problem.
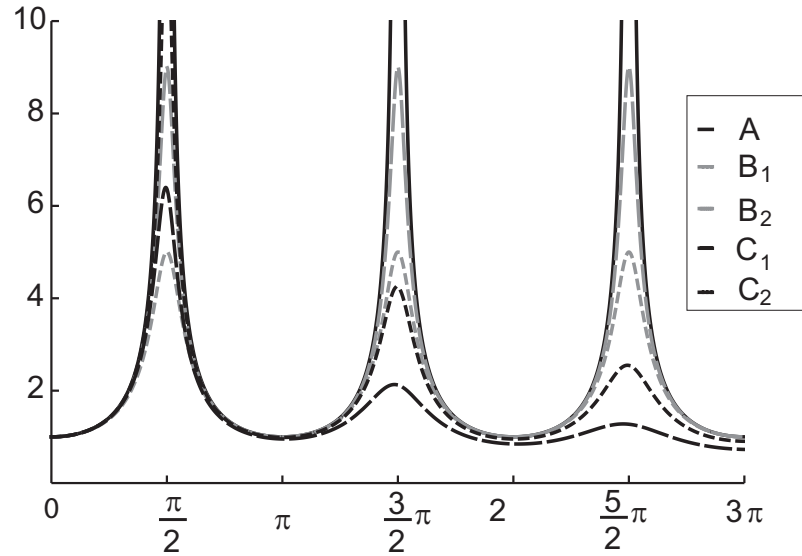
Figure 2.6: Example of resonance:

A) Elastic layer over infinitely rigid half-space.

B_1) Elastic layer over deformable half-space (Eq. 2.19), $I = 9$.

B_2) Elastic layer over deformable half-space, $I = 5$.

C_1) Viscoelastic layer over undeformable half-space(Eq. 2.23), $D = 5\%$.

C_2) Viscoelastic layer over undeformable half-space, $D = 10\%$.

2.6 Alluvial Valley Edges

Dangerous patterns have been individuated whenever a soft layer is situated over a hard bedrock. As stated in the previous section, the displacement field at the surface of an alluvial valley presents complicated features, which locally are strongly dependent on a number of physical parameters, such as frequency and nature of the incident wave, location of the observation point, observed component of the motion, number and shape of the layers, and finally impedance contrast.

As the simple two layer model cannot fully explain the whole situation, many numerical methods were adopted to study the alluvial valley response, in order to investigate the wavefield features which cannot be explained by means of the cited model. Two effects should be taken into consideration and are worthy to be cited. The first one concerns seismic P, S_V and S_H wave focalization at the edge, due to multiple reflections on the oblique interfaces between layer(s) and bedrock. The second phenomenon which can occur, concerns surface wave generation resulting in long lasting shaking. Both phenomena have been addressed to explain observed damages at valley borders. Investigated models cover several different bedrock shapes (Bard & Gabriel, 1986; Aki, 1988, Bard, 1994), nonetheless they are closely related to section 2.4 and generally later numerical models included them as natural boundary conditions.

2.7 Irregular interfaces

As stated above, modeling has been widely adopted, showing results which are "basin-dependent" albeit successful. It has been noted that one of the key parameters is the number of layers considered. Further attempts to improve accuracy lead researchers to speculate also on interface shapes (Dravinski, 2009/07; YU, 2009). Dravinski in particular, numerically investigated functionally corrugate and random interface effects delineating some general characteristics.

- Presence of interface corrugation can produce significant reduction in shallow motion on peaks.

- Reduction strongly depends on the nature of corrugation and on the mean interface profile, namely, deterministic versus random, semielliptical versus semicircular. As a consequence, in case of a functionally described corrugation, reduction can be correlated to the parameters describing its shape.

- The overall effect is dependent on wave nature.

- There is dependence on the average depth of the basin, which is particularly pronounced for S_V incidence.

- The fundamental resonant frequency of a smooth basin is lowered if corrugation is introduced.

This aspect of the problem is still an open area of research.

Chapter 3

In situ testing and Surface waves overview.

Methods available to investigate the elastic properties of a site can be classified into two main families.

- Invasive Testing

- Non-Invasive Testing

The first category usually includes a direct sampling of the subsurface. Ground penetrating cone, boreholes, seismic tomography for example, belongs to this category. Surface wave testing belongs to the non-invasive tests class. They gained popularity during the past twenty years as a low cost alternative to invasive geotechnical testing. The main purpose of surface wave testing is to determine the shear wave velocity (V_s) profile of the subsurface within the shallowest tens of meters. Propagating elastic waves are recorded by means of an array of geophones placed on the ground surface. The signal can be either naturally or artificially generated. In the former case the test is said to be passive surface wave testing, in the latter case it is called active. In passive testing the natural seismic tremors are recorded, which are due to many different causes, both natural, like wind, sea wave motion vibrations from neighbor structures like buildings, trees, etc, and man-made like seismic noise linked to car traffic and trains. Active testing on the other hand focuses on artificial sources like a sledge hammer, a weight drop, an explosion or a fixed frequency electromechanical shaker.

Different methods exist today, and they can be classified according to source employed, number of sensors and array geometry. The data acquired is further

elaborated according to the assumption that the signal is constituted by Rayleigh and Love (sec. 2.3) surface waves. The main characteristic of both kinds of surface waves is that displacement amplitude of particles decreases quickly with depth, at a rate depending on frequency (or wavelength). As a consequence, a wave samples the subsurface to a depth comparable to its own wavelength. This phenomenon of frequency dependence makes the wave train dispersive, because of the variation, generally increasing, of seismic velocity with depth. The dispersion curve can be calculated from wave-trains in the frequency-wavenumber domain by means of a two-dimensional Fourier transform. In the current practice the dispersion curve is then used to estimate a layered soil model where parameters of each layer are thickness (h), density (ρ), shear wave velocity (V_s) and compressional wave velocity (V_p). Steps necessary to accomplish the task can summarized with:

- Acquisition.

- Dispersion analysis.

- Layered-soil reconstruction.

Different methods were developed starting from early 1980s.

3.1   Active methods

3.1.1   SASW method

The simplest and earliest method of this family was developed at the University of Texas (UT) at Austin and today is popular as *spectral analysis of surface waves* (SASW), (Heisey *et al.*, 1982; Nazarian & Stokoe, 1984). The field setup is comprised of an impulsive source and two common velocity geophones placed at a distance d. The impulsive source signal containing a broad spectrum in frequency, usually from 1 to 100 Hz is produced by a sledgehammer drop, and seismograms $\phi_1(t)$, $\phi_2(t)$ are recorded and analyzed by the Fast Fourier Transform algorithm (FFT). Corresponding spectra,$\Phi_1(\omega)$, $\Phi_2(\omega)$ are then combined to form the cross-spectra.

$$Y_{12} = \Phi_1^*(\omega)\Phi_2(\omega)\,,$$

where the asterisk indicates complex conjugation. Phase velocity is then obtained calculating the arc tangent of the cross-spectrum

$$\Theta_{12}(\omega) = arctg\left(\frac{\Im(Y_{12})}{\Re(Y_{12})}\right)\,,$$
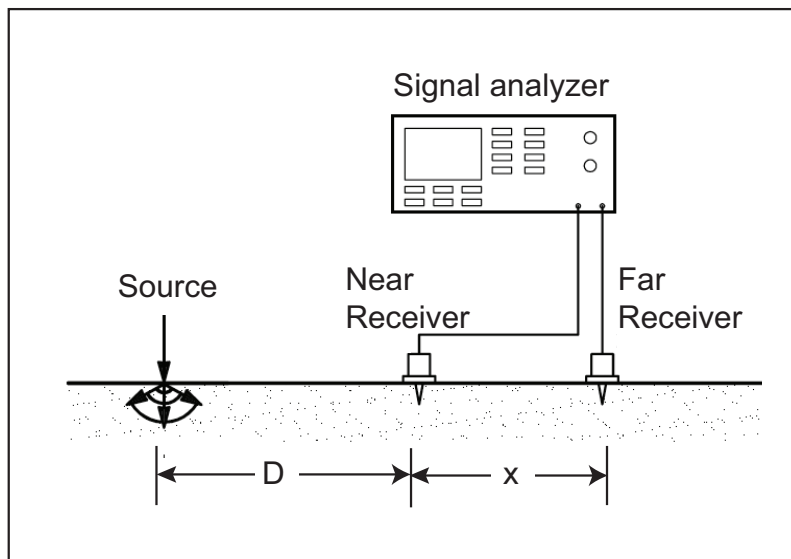
Figure 3.1: SASW field setup

which depends, frequency by frequency, on the lag time between the two geophones placed at the known distance

$$t(\omega) = \Theta_{12}(\omega)/\omega$$

$$V_R(\omega) = \frac{d}{t(\omega)} \, . \tag{3.1}$$

Once the velocity (3.1) has been obtained, the soil profile is reconstructed by an inversion algorithm to produce a layered model, using the relation between the V_R and the above mentioned constitutive parameters of the layered sequence. The use of cross-spectra is based on the implicit assumption that only one mode of propagation is present and therefore the described data processing hides the higher modes This is actually the fundamental Rayleigh mode, therefore it is not surprising that initially the method was focused on increasing its accuracy to isolate this feature. Subsequently many studies examined the possibility of contamination from higher modes (Roesset *et al.*, 1990; Rix *et al.*, 1991; Tokimatsu *et al.*, 1992; Stokoe *et al.*, 1994), and in successive works the concept of *apparent dispersion curve* appeared (Gucunski and Woods, 1992; Williams and Gucunski, 1995). Later evolutions attempted to account for higher modes, unfortunately the two stations scheme is not suitable to capture the complete information present in the wave-train. A compre-

hensive list of the publications on SASW up to early 1990s can be found in the
Annotated Bibliography on SASW by Hiltunen and Gucunski (1994).

3.1.2   MASW method

As previously stated, surface wave nature is multimodal; so in order to collect the
complete information of dispersion curve, an array composed of many geophones is
necessary. The earliest documented applications of multi-channel acquisition pertain
to early 1990s. In the mid-90s at the Kansas Geological Survey the basis of a new
method, the *Multistation Analysis of surface waves* (MASW), was developed which
became popular especially in the field of geotechnical engineering after publications
by Park et al. (1999) who showed the effectiveness of the method. The successive
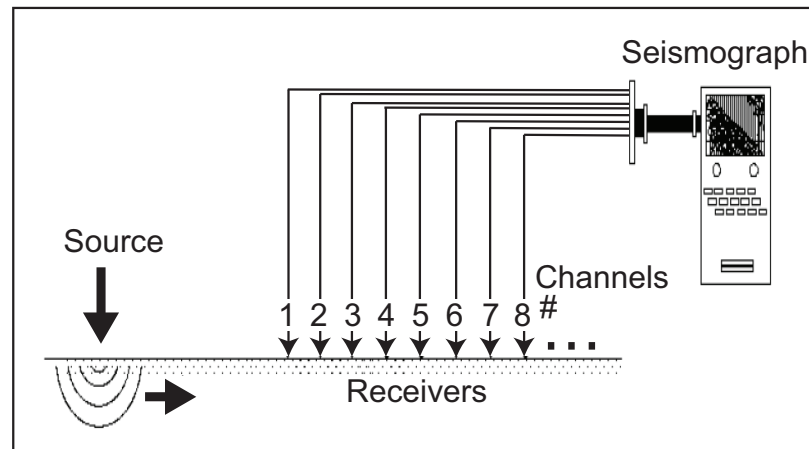
Figure 3.2: MASW field setup, from.......

advancements and developments utilizing this methodology confirmed the advantages
with respect to SASW (Foti, 2000) and brought about a deeper knowledge of the
complex structure of the surface wavefield. The previously reported higher modes
and leaky modes were studied and confirmed in a detailed manner (Ryden *et al.*,
2003; 2004; Ryden and Lowe, 2004).
MASW employs in its turn an impulsive artificial source, to be operated at one
end of the profile of geophones. The data collected exists in a two-dimensional
space,$[\mathbb{R} \times t]$, where one dimension is the space and the second dimension is the time.

The classic analysis is performed by transforming this space into the [*frequency* × *wavenumber*] domain by a double Fourier Transform (*f-k* Transform)(Tselentis & Delis, 1988), but also the alternative approach of *p-τ* transform (Piwakowski *et al.*, 2004) has been proposed which seems promising. Once in the transformed space, the dispersion curves are obtained by individuating the maxima of the 2D transformed data distribution, this is called the *peaking phase*, see fig. 3.3 where the peaking procedure is depicted both for MASW and for REMI (Sec. 3.2.1). These curves are
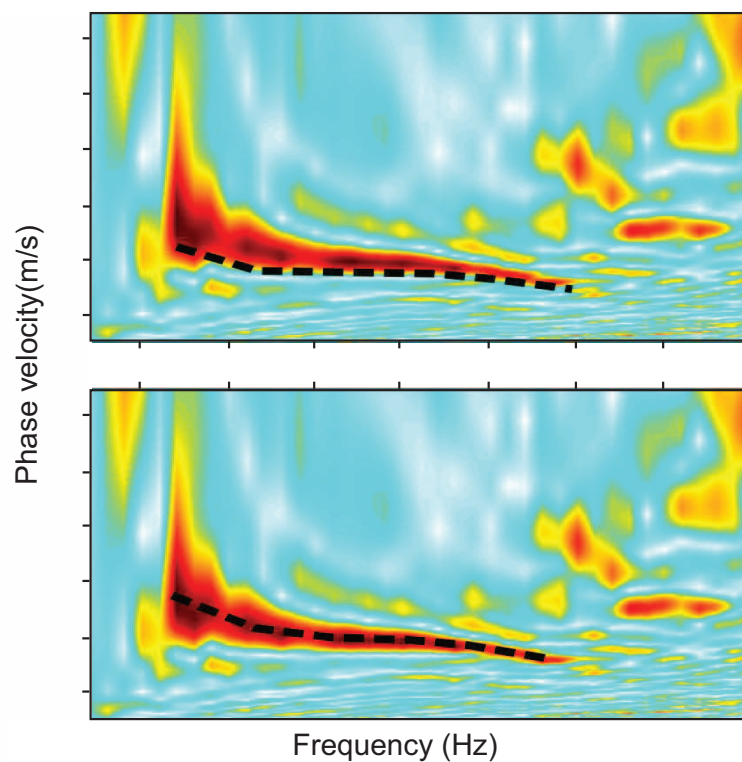
Figure 3.3: Modes of propagation peaking, REMI(Top), MASW(Bottom)

then used as the objective functions for the inversion algorithm. The investigation depth is about a half of the profile length.

3.2   Passive methods

Passive methods exploits natural random seismic noise. It is a matter of fact that the seismic noise (ground roll) was one of principal causes for loss in accuracy of seismic reflection and seismic refraction methods. When the passive methods were first introduced a noteworthy literature about ground roll suppression was already available. It is curious to note how the same knowledge was then employed to study the ground roll.
Passive methods present an advantage with respect to active methods in that they need noise to be exploited and then they can be used in very noisy environments as well. In fact to produce a signal strong enough to overcome the disturbance may require strong sources; the problem increases with increasing planned investigation depth.

3.2.1   REMI method

REfracted MIcrotremors (REMI), first introduced by Louie (2001), is from any point of view quite similar to MASW. It employs the same array of geophones, and the data elaboration is, with a few exceptions, the same. The first difference is that the source is now the natural seismic noise, this implies that the signals impinge the profile coming from random directions. The signal amplitude can be very low as compared to an active test. In order to get a good statistics on the entire possible arrival directions of noise wavetrains, recordings have to last for a longer time, typically 10 to 30 min. The second difference is in the picking phase. The dispersion curves are not associated to the maxima of the f-k transformed space as is for MASW, but to the lower edge of them, in other words the dispersion curve must be willingly underestimated. This is due to the fact that waves reach the array also from directions other than the array orientation and the corresponding phase velocity results will be overestimated if the maximum is considered.
As an example, assume a wave is reaching the array from a direction normal to the array itself, if the far field assumption is made, the wave is plane and it reaches all receivers simultaneously. In this limiting case the obviously wrong conclusion is that the phase velocity is infinity. Figure 3.3 shows how the picking is performed. The investigation depth is about a half of the profile length.

3.2.2   2D array method

This is another method based on microtremors. The field setup is an array of sensors placed circularly, with or without a central receiver. For each couple of geophones

coherence γ is calculated by averaging the normalized cross-spectra with respect to the distance of the couple.

If the recorded noise is a stochastic process, it can be shown (Aki 1957) that the coherence is a function of the frequency and of the distribution of wave velocity under the array.

$$\gamma_{\omega,V_s} = J_0(\frac{\omega r}{V_s})\,, \tag{3.2}$$

where J_0 is the order zero Bessel function. The stochastic process assumption is valid for moderate levels of constant isotropic noise. Comparing calculated coherences with theoretical ones obtained from a model with known density, elastic parameters and thickness, the subsurface model can be deduced. The advantage of this approach is the greater depth of investigation, compared with the MASW. The maximum investigation depth can be evaluated as 2-3 times the radius of the array.

3.2.3   MOPA method

Multi-offset phase analysis of surface waves (MOPA)(Strobbia & Foti, 2006) has been recently introduced as a novel method to assess the quality and reliability of active source, linear spread, multichannel surface wave dispersion. The procedure is based on the linear regression of phase vs. offset data using a statistical approach. Despite the fact that it cannot be considered as an alternative method to conventional SWM's, it is worthy to mention because it allows the estimation of the uncertainties in the dispersion curve, which can propagate through the inversion process to the shear wave velocity profile. The most important advantage is its ability to assess whether significant model errors are present.

3.2.4   Nakamura's Spectral ratio method

Another technique of note is the *horizontal to vertical component spectral ratio method*, currently called the *Nakamura's method* (HVSR). The field setup is usually comprised of by a 3D-components station. Microtremors are recorded and exploited to obtain some structural information. Registration can last from 10 to 30 minutes as was the case for MASW. Even if it does not produce shear waves velocity profiles, it is worthy to mention HVSR, because it is useful to estimate the local seismic amplification. This method is focused on obtaining the resonance frequency of the underground structure. This parameter is important for civil engineering to avoid double resonance effects on new buildings or artifacts. Double resonance effect takes place when the proper frequency of the artifact coincides with the proper frequency

of the subsurface soil structure. Typical amplifying sites are comprised of a soft(low shear wave velocity) layer over a more stiff basement (high shear wave velocity). Explanation of Nakamura's procedure is straightforward if the simplified model 3.4 is considered (Mucciarelli, 1998) along with the following assumption,
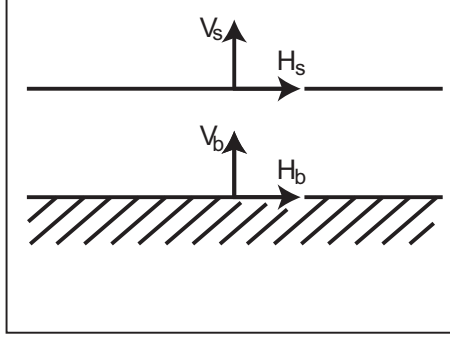
Figure 3.4: Nakamura's simplification of underground structure

- Microtremors are generated by shallow local sources and deep sources are not accounted for.

- Sources at the surface have no effect on the deep interface.

- The vertical component of motion is not influenced by local amplification phenomenon (Castro *et al.*, 1996).

and noting that this model involves four spectra; namely the transformed vertical and horizontal components at the surface, $V^s(\omega)$ $H^s(\omega)$ and corresponding spectra at the bottom $V^b(\omega)$, $H^b(\omega)$. Nakamura's assumptions imply that the vertical components ratio, contains only terms relative to local sources at the surface $A^s(\omega)$ and at the bottom $A^b(\omega)$, while the ratio for horizontal components contains an extra term due to amplification in situ at the surface $\mathcal{S}(\omega)$.

$$
\begin{aligned}
R_v &= \frac{V^s(\omega)}{V^b(\omega)} = \frac{A^s(\omega)}{A^b(\omega)} \\
R_h &= \frac{H^s(\omega)}{H^b(\omega)} = \frac{A^S(\omega)}{A^b(\omega)}\mathcal{S}(\omega)\,.
\end{aligned}
$$

Source terms can be simplified calculating the ratio R_h/R_v. Assuming now that spectral amplitude of horizontal and vertical components are equal, the amplification

factor at the surface can be directly obtained.

$$\mathcal{S}(\omega) = \frac{H^s(\omega)}{V^s(\omega)} \, . \tag{3.3}$$

This function presents peaks which position is well correlated with the proper frequencies of vibration of the stratified structure both under S_H waves propagation and fundamental mode Rayleigh propagation. The amplitude of peaks on the other hand , can be only considered as an indication on the order of magnitude of the real amplification.

Chapter 4

The forward model.

A key element in surface wave testing is the forward model that predicts the displacement field induced by seismic waves, such as Love or Raleigh waves. To date, such subsurface models are oversimplified; lateral variation and wave back scattering are not taken into account and only a few higher modes of vibration are accounted for. The spatial variation of the layers' thickness is usually neglected and so is the fraction of incidental energy of the fundamental mode that is reflected or converted to higher modes which usually are neglected as well or in some cases, only a few are considered. Although layered models have been thoroughly investigated, there are not any practical applications which investigate structures other than horizontally layered or depth varying ones.

One consideration that can be made about the layered model is that the plane waves assumption and boundary conditions leads to systems of equations whose solution is represented by surface waves. This still holds if the interfaces are slightly perturbed away from flatness. Investigations on this aspect can be traced back for fundamental mode of vibration and long waves, as in Gjevic (1973). He showed that a perturbation in layer thickness reflects on horizontal wavenumbers which become spatially varying. Further studies of Hador and Buchen (1999), applied a Lagrangian-based method to both Love and Rayleigh waves and confirmed the observations. On the other hand, methods that exploit coupling of different modes of vibration have been also proposed; Maupin (1987) summarized this class, of so called "Matching Mode Methods".

Unfortunately application of analytical or semi analytical method presents many difficulties when dealing with complex scattering patterns. The major problem, ex-

pecially with steep interfaces is that they destroy the reflection pattern typical of Love and Rayleigh wave generation. This is due to the fact that presence of a srong lateral heterogeneity changes the boundary conditions of the elastodynamic problem and the particular solution of the partial differential wave equation changes as well. Obviously, surface motion still exists, but defining it as Love or Rayleigh surface waves could be seriously imprecise.

In classical SWM's, surface waves are assumed to be Rayleigh waves, this means that a parallel layered model has been implicitly assumed. As a consequence search for a soil model geometry other than the assumed one can only result in slight perturbations. The only possible deduction is that overcoming limitations of layered models requires to exploit P and S waves which are indeed general solutions of the elastodynamic problem. Geometry can then be retrived by a complete waveform inversion based on a forward model capable of successfully reproducing all of the features of the displacement field in presence of complex scattering phenomena.

4.1   Elastodynamic Preliminaries

In the context of elastodynamics we can investigate the deformation of a body in terms of *displacement*, defined as function $\boldsymbol{u}(\mathbf{x}, t)$ of space and time, which denotes the vector distance of the position of a particle at the time t, with its former position at some reference time t_0. This is assumed to be a continuous vector function across all of the domains of reference and can be exploited as a tool to describe the elastic behavior of a body. In fact, when considering displacements of neighboring particles, the concept of *strain* can be mathematically written in terms of a local variation of the displacement function.

The *strain tensor* ϵ, formalizes this concept when displacements are small with respect to the size of the body, and local rotations can be neglected. In matrix notation[1]

$$\boldsymbol{\epsilon} = \frac{1}{2} \begin{pmatrix} 2\,u_{1,1} & u_{2,1} + u_{1,2} & u_{3,1} + u_{1,3} \\ u_{1,2} + u_{2,1} & 2\,u_{2,2} & u_{3,2} + u_{2,3} \\ u_{1,3} + u_{3,1} & u_{2,3} + u_{3,2} & 2\,u_{3,3} \end{pmatrix} ,$$

or in component notation

$$\epsilon_{pq} = \frac{1}{2} \left(u_{p,q} + u_{q,p} \right) . \tag{4.1}$$

---

[1]Commonly partial derivatives are indicated by means of a comma followed by a subscript which identifies the quantity with respect to which the derivative is performed, as an example $u_{i,j} = \frac{\partial u_i}{\partial x_j}$

It can be assumed that strain is produced by a set of forces applied to the body; the tensor relation which connects these two vector fields is called *constitutive relation*, it is a generalization of Hooke's Law of the spring valid for three dimensions and can be written introducing a 3×3 constant tensor C

$$\tau_{ij,j} = C_{ijpq}\epsilon_{pq} \,. \tag{4.2}$$

The most general form of C_{ijpq} requires 81 independent quantities. For our purposes we will restrict it to linear, isotropic and homogeneous bodies, where the tensor constant assumes its simplest form. It was demonstrated by Harold Jeffreys in 1972 [76] that in this case C can be written in terms of two constants called *Lamé modules*

$$C_{ijpq} = \lambda\delta_{ij}\delta_{pq} + \mu(\delta_{ip}\delta_{jq} + \delta_{iq}\delta_{jq}) \,. \tag{4.3}$$

In its final form, the stress tensor is

$$\boldsymbol{\tau} = \begin{pmatrix} \lambda \sum_i u_{i,i} + 2\mu u_{1,1} & \mu(u_{1,2} + u_{2,1}) & \mu(u_{1,3} + u_{3,1}) \\ \mu(u_{1,2} + u_{2,1}) & \lambda \sum_i u_{i,i} + 2\mu u_{2,2} & \mu(u_{2,3} + u_{3,2}) \\ \mu(u_{1,3} + u_{3,1}) & \mu(u_{2,3} + u_{3,2}) & \lambda \sum_i u_{i,i} + 2\mu u_{3,3} \end{pmatrix} \,,$$

with $i \in \{1, 2, 3\}$.
Introducing dilatational and shear wave velocities defined respectively as

$$\begin{aligned} C_p^2 &= (\lambda + 2\mu)/\rho \\ C_s^2 &= \mu/\rho \,, \end{aligned} \tag{4.4}$$

and exploiting Einstein's notation on repeated indexes, it can be written in compact notation as

$$\tau_{ij} = \rho \left(C_p^2 - 2C_s^2 \right) u_{m,m}\delta ij + \rho C_s^2 \left(u_{i,j} + u_{j,i} \right) \,. \tag{4.5}$$

Consider an ideal surface inside a body, and a point $\boldsymbol{p}$ on that surfaceand that the normal vector to the surface in $\boldsymbol{p}$ is directed toward the portion of material which is exerting a force on the material on the other side of the surface, then the stress vector at the point $\boldsymbol{p}$ is given by

$$t_{(\hat{\mathbf{N}})i} = \tau_{ij}N_j \,. \tag{4.6}$$

From the basic concepts of stress and strain, rewriting Newton's second law, the following equation of motion can be derived [4]

$$\rho\ddot{u}_i = f_i + \tau_{ij,j} \,. \tag{4.7}$$

Cycling on index "i", equation 4.7 describes three coupled equations whose solutions represent the three-dimensional motion of particles.

$$\begin{cases} \rho\ddot{u}_1 = f_1 + (\lambda + \mu)(u_{1,11} + u_{2,21} + u_{3,31}) + \mu(u_{1,22} + u_{1,33}) \\ \rho\ddot{u}_2 = f_2 + (\lambda + \mu)(u_{1,12} + u_{2,22} + u_{3,32}) + \mu(u_{2,11} + u_{2,33}) \\ \rho\ddot{u}_3 = f_3 + (\lambda + \mu)(u_{1,13} + u_{2,23} + u_{3,33}) + \mu(u_{3,11} + u_{3,22}) \end{cases} .$$

which can be collected in a synthetic form.

Alternative notations for this equation found in literature are:

$$b_j + (c_p^2 - c_s^2)u_{i,ij} + c_s^2 u_{j,ii} - \ddot{u}_j = 0$$

$$\mathbf{b} + (c_p^2 - c_s^2)\nabla\nabla \cdot \boldsymbol{u}(\mathbf{x}, t) + c_s^2\nabla^2\boldsymbol{u}(\mathbf{x}, t) - \ddot{\boldsymbol{u}}(\mathbf{x}, t) = \mathbf{0} . \qquad (4.8)$$

where ∇ is Laplacian operator and $\boldsymbol{b} = \boldsymbol{f}/\rho$. If Helmholtz decomposition of vectors and forces is assumed then

$$\boldsymbol{u} \;=\; \nabla\phi + \nabla \times \boldsymbol{\xi} \qquad (4.9)$$

$$\boldsymbol{b} \;=\; \nabla\beta + \nabla \times \boldsymbol{B} , \qquad (4.10)$$

eq. 4.8 decouples into scalar and vector independent equations

$$C_p^2\nabla^2\phi + \beta \;=\; \ddot{\phi} \qquad (4.11)$$

$$C_s^2\nabla^2\boldsymbol{\xi} + \boldsymbol{B} \;=\; \ddot{\boldsymbol{\xi}} , \qquad (4.12)$$

and three different two-dimensional approximations can be derived.

- **Anti-plane strain**

    definition: $\quad \begin{cases} u_1 = u_1 = 0 \\ u_3 = u_3(x_1, x_2, t) \end{cases}$

$$\qquad (4.13)$$

    formulation: $\quad \begin{aligned} \ddot{u}_3 &= b_3 + c_2^2 u_{3,ii} \\ t_{i3} &= \rho c_2^2 u_{3,i} \end{aligned}$

$$\qquad (4.14)$$

- **Plane Strain**

    definition: $\quad \begin{cases} u_1 = u_1(x_1, x_2, t) \\ u_2 = u_2(x_1, x_2, t) \\ u_3 = 0 \end{cases}$

$$\qquad (4.15)$$

    formulation: $\quad \begin{aligned} \ddot{u}_j &= (c_1^2 - c_2^2)u_{i,ij} + c_2^2 u_{j,ii} + b_j \\ t_{ij} &= \rho(c_1^2 - c_2^2)u_{\gamma,\gamma}\delta_{ij} + \rho c_2^2(u_{i,j} + u_{j,i}) \end{aligned}$

$$\qquad (4.16)$$

- **Plane Stress**

$$\text{definition:} \quad \begin{cases} t_{ij} &= t_{ij}(x_1, x_2, t) \\ t_{3,j} &= 0 \\ b_3 &= 0 \end{cases}$$

(4.17)

$$\text{formulation:} \quad \begin{aligned} t_{ij} &= \lambda' u_{\gamma,\gamma} \delta_{ij} + \mu \big(u_{i,j} + u_{j,i}\big) \\ \rho \ddot{u}_j &= (\lambda' + \mu) u_{i,ij} + \mu u_{j,ii} + \rho b_j \\ \epsilon_{33} &= -\lambda'/2\mu \, u_{\gamma,\gamma} \end{aligned}$$

(4.18)

with

$$\lambda' = 2\lambda\mu/\left(\lambda + 2\mu\right) \ .$$

4.2 A first attempt: Lagrangian Forward Model

The next model presented partially overcomes the limitations of layered systems. As a first investigation, it focused on the dynamics of Love waves which is attractive from a theoretical point of view and has been studied analytically by several authors (De Noyer, 1961; Knopoff *et al.*, 1967; Wolf, 1970; Lysmer, 1971; Gjevik, 1973), and more recently (Maupin, 1987; Hador-Buchen, 1999). Studies on lateral variation spans over 40 years in literature and many methods have been used. The Lagrangian approach was introduced by Whitham (1967a, 1967b) in the context of water waves investigation.

The present approach stems from a local-mode representation of monochromatic Love waves which is then optimized by the Action Principle. Conservative systems are considered, and the dynamic equations follow from a variational principle based on the Lagrangian for Love waves . The particular case of an homogenous upper soft layer with varying thickness $\eta(x)$ lying over a semi-infinite hard layer, with x as the propagation direction is considered.

The vertical profile of wave displacements at any horizontal position x is represented by a local-mode series involving the propagating eigenmodes allowed by the dispersion relation which depends upon the local thickness $\eta(x)$. The amplitudes of the modes are unknown and assumed spatially varying in x.

Using the Action Principle, the optimal amplitudes satisfy the Euler-Lagrange equations that lead to a coupled-mode system, i.e. a set of coupled second order ordinary differential equations. The local-mode vertical expansion of waves accounts for both the forward and backward propagating modes. Locally, such eigenmodes

are exactly equal to those for a parallel layered media, but their wavelength is spatially varying because of the local layer's thickness variation. All the eigenmodes satisfy the zero-stress condition at the free-surface, and the continuity of the vertical stresses at the interface between the two layers. Such local-mode representation is exact for a flat interface, and it is a good approximation for weakly varying sloping interfaces. However, for very steep interfaces the wave field nearby the interface is poorly represented and wave energy is not generally conserved, because each eigenmode in the wave expansion violates the normal stress continuity on the interface between the two layers, and so does the wave field comprised of a linear superposition of modes. The purpose is to test the applicability of a mode matching based on Lagrangian minimization formulation to Love-wave propagation through non-parallel media, allowing for reflections.
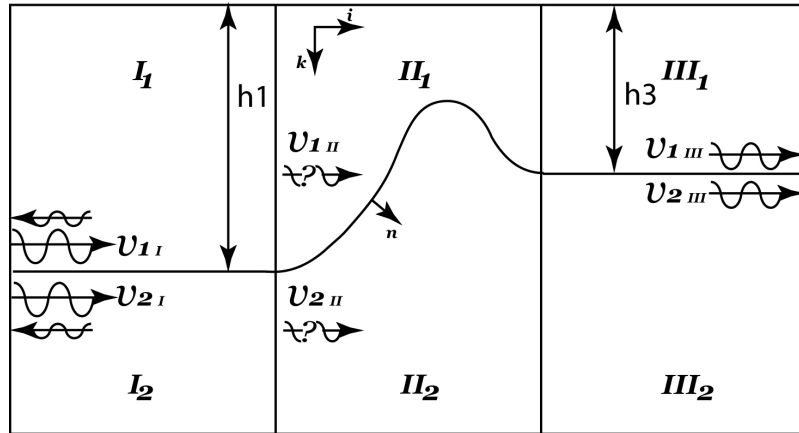
Figure 4.1: Model set up and geometry.

4.2.1   The transmission problem

Consider a laterally heterogeneous media as shown in Figure 4.1 where x and z are, respectively, a horizontal and a vertical coordinate. Let the upper and the lower layers have densities ρ_1 and ρ_2, respectively. The upper layer has a free boundary at $z = 0$ and the lower layer is assumed to be infinitely deep. The media is divided into three different vertical zones I $(x < -L)$, II $(-L \leq x \leq L)$ and III $(x > L)$, respectively.

Further, the two layers are assumed to extend horizontally to infinity and in the far field zones I and III the layers are parallel. In the intermediate zone II

the upper and lower layer are separated by a varying interface $z = \eta(x)$. Zone I is excited by an incident monochromatic plane wave that generates a displacement field $v_{in}(x, z, t)$ that propagates in the x-direction. As it passes through zone II, it undergoes reflections and only part of its energy is transmitted to zone III where the wave displacements $v_{III}(x, z, t)$ propagate undisturbed. The cumulated effect of all the reflections in zone II yields a reflected back-propagating wave displacement $v_R(x, z, t)$ through zone I, and the total wave field in zone I is $v_I = v_R + v_{in}$. The displacements of these waves are normal to the plane through the axis x and z (Jeffreys, 1962). The linear elastic equation of motion 4.19 is assumed to hold in all regions.

$$-\rho \frac{\partial^2 v_{II}}{\partial t^2} + \mu \nabla^2 v_{II} = 0. \tag{4.19}$$

where $\nabla = \partial_x \, \hat{x} + \partial_z \, \hat{z}$, $\hat{x}, \hat{z}$ are the unit vectors of x and z, and ρ and μ are soil parameters which are piecewise functions in both x and z given by

$$\rho(x, z) = \begin{cases} \rho_1, & 0 \leq z \leq \eta(x) \\ \rho_2, & z > \eta(x) \end{cases}, \qquad \mu(x, z) = \begin{cases} \mu_1, & 0 \leq z \leq \eta(x) \\ \mu_2, & z > \eta(x) \end{cases}.$$

At the free-surface $z = 0$, the zero-stress boundary condition is imposed, as well as zero stress at $z \to \infty$

$$\mu \frac{dv_{II}}{dz}\bigg|_{z=0} = 0 \qquad \mu \frac{dv_{II}}{dz}\bigg|_{z \to \infty} = 0. \tag{4.20}$$

The continuity of both displacements and normal stresses to the interface $z = \eta_{(x)}$ requires vanishing jumps

$$[v_{II}]_{z=\eta} = 0, \qquad [\mu \nabla v_{II} \cdot \boldsymbol{N}]_{z=\eta} = 0, \tag{4.21}$$

where $\boldsymbol{N}$ is the unit vector normal to the interface η, that is

$$\boldsymbol{N} = \frac{1}{\sqrt{1 + \left(\frac{d\eta}{dx}\right)^2}} \left(-\frac{d\eta}{dx} \hat{x} + \hat{z}\right). \tag{4.22}$$

and $[f]_{z=\eta} = \lim_{\epsilon \to 0} (f(\eta + \epsilon) - f(\eta - \epsilon))$ is the jump operator .

Continuity of stresses and displacements at the common boundaries of zones I-II ($x = -L$) and zones II-III ($x = L$), respectively is also required, as follows:

$$(v_{II} - v_I)|_{x=-L} = 0, \qquad \mu \left(\frac{\partial v_{II}}{\partial x} - \frac{\partial v_I}{\partial x}\right)\bigg|_{x=-L} = 0, \tag{4.23}$$

$$(v_{III} - v_{II})|_{x=L} = 0, \qquad \mu \left(\frac{\partial v_{III}}{\partial x} - \frac{\partial v_{II}}{\partial x}\right)\bigg|_{x=L} = 0.$$

4.2.2   Action Principle for Love waves

Consider the Lagrangian density

$$\mathcal{L} = (\mathcal{T} - \mathcal{K} - \mathcal{B}) \,, \tag{4.24}$$

where $\mathcal{T}$ and $\mathcal{K}$ are the kinetic and potential energy densities, respectively, as follows:

$$
\begin{aligned}
\mathcal{T} &= \frac{1}{2} \int_0^\infty \rho \left(\frac{\partial v_{II}}{\partial t} \right)^2 dz, \\
\mathcal{K} &= \frac{1}{2} \int_0^\infty \mu \, |\nabla v_{II}|^2 \, dz,
\end{aligned}
\tag{4.25}
$$

and

$$
\begin{aligned}
\mathcal{B} = & \; [\mu \, v_{II}]_{z=\eta_{(x)}} \left(\frac{\partial v_{II}}{\partial z} - \frac{\partial v_{II}}{\partial x} \frac{d\eta}{dx} \right) \Bigg|_{z=\eta_{(x)}} \\
& - \int_0^\infty \mu \frac{\partial v_I}{\partial x} \left(v_{II} - \frac{v_I}{2} - v_{in} \right) \Bigg|_{x=-L} dz \\
& + \int_0^\infty \mu \frac{\partial v_{III}}{\partial x} \left(v_{II} + \frac{v_{III}}{2} \right) \Bigg|_{x=L} dz,
\end{aligned}
\tag{4.26}
$$

In appendix A it is shown that the boundary value problem (4.19 - 4.20 - 4.21 - 4.23) is the minimizer of Action, that is

$$\delta \int_{t_1}^{t_2} \int_{-L}^{L} (\mathcal{T} - \mathcal{K} - \mathcal{B}) \; dx \; dt = 0 \,, \tag{4.27}$$

where δ denotes variational differentiation.

4.2.3   Wave expansion and dynamics

Mode expansion for zones I and III

Assume the thickness of the upper layer is equal to d. The standard representation of the wave field v_p is given in the form

$$v_p(x, z, t) = \sum_n A_n \; f_n(z; d) \; e^{i(k_n x - \omega t)} \; + \; c.c. \tag{4.28}$$

where the wave numbers k_n satisfy the dispersion relation

$$\tan\left(i\nu_1 d\right) = -\frac{\mu_2 \nu_2}{i\mu_1 \nu_1} \tag{4.29}$$

$$\nu_i = \sqrt{k^2 - \frac{\rho_i \omega^2}{\mu_i}} = \sqrt{k^2 - \frac{\omega^2}{\beta_i^2}}$$

and $f_n(z; d)$ are the eigenfunctions of the Sturm-Liouville problem

$$\frac{d^2 f_n}{dz^2} - \nu_i^2 f_n = 0, \tag{4.30}$$

with the requirements of continuity for both displacements and vertical stresses at $z = d$, as follows

$$[f_n]_{z=d} = 0, \qquad \left[\mu\frac{df_n}{dz}\right]_{z=d} = 0, \tag{4.31}$$

and zero-stresses at the free-surface, as follows

$$\left.\frac{df_n}{dz}\right|_{z=0} = 0. \tag{4.32}$$

From (4.28) the incident and reflected components of the displacements $v_I = v_{in} + v_R$ in zone I can be defined respectively as

$$v_{In} = \sum_n I_n\, e^{ik_{n_I}(x+L)}\, f_n(z; d_1)\, e^{-i\omega t}\ +\ c.c., \tag{4.33}$$

$$v_R = \sum_n R_n\, e^{-ik_{n_I}(x+L)}\, f_n(z; d_1)\, e^{-i\omega t} + c.c.,$$

where $d_1 = \eta(-L)$, I_n and R_n are constant amplitudes. Further, in zone III we can define v_{III} as

$$v_{III} = \sum_n T_n\, e^{ik_{n_{III}}(x-L)} f_n(z; d_3)\, e^{-i\omega t}\ +\ c.c., \tag{4.34}$$

where $d = d_3 = \eta(L)$, and T_n is the amplitude of the transmitted wave.

Local-mode wave representation for zone II

Given the depth of the upper layer $d = \eta(x)$ at x, the local wave numbers $k_n(x)$ and the associated eigenmodes $f_n(z; \eta)$ can be computed from the dispersion relation

(4.29) at every x. Thus, the wave field in zone II can be formally represented by the eigenmode series (4.28) for parallel layers as

$$v_{II}(x, z, t) = \sum_n A_n(x)\ f_n(z, \eta)\ e^{i\left(k_{n_{II}}(x)\ x - \omega t\right)},\qquad (4.35)$$

where now both k_n and f_n are spatially varying because of the interface depth variation $d = \eta(x)$. Consequently, the Sturm-Liouville problem (4.30) can be considered as a continuous family of problems with parameter $d = \eta(x)$. Hereafter, mode amplitudes $A_n(x)$ are assumed to be an unknown function of x and their optimal values are deduced via the Action Principle. Note that (4.35) satisfies the continuity of displacements at the interface since $[f_n]_{z=\eta} = 0$ at any x, but the normal stresses are not continuous. Indeed, from (4.35) and (4.31)

$$\left[\mu \nabla v_{II} \cdot \boldsymbol{N}\right]_{z=\eta} = -\frac{d\eta}{dx}\left[\mu \frac{\partial v_{II}}{\partial x}\right]_{z=\eta}.\qquad (4.36)$$

Consequently, the total energy density $\mathcal{E} = \mathcal{T} + \mathcal{K}$ is also not conserved in x and from (4.25) one can show that

$$\frac{d\mathcal{E}}{dx} \propto \frac{d\eta}{dx}\left[\mu \frac{\partial v_{II}}{\partial x}\right]_{z=\eta}.\qquad (4.37)$$

Said that, the local-mode representation (4.35) can be optimized by exploiting the Action Principle (4.27) to find the best mode amplitudes, $A_n(x)$, that minimize the residuals (4.36) and (4.37). For mild varying interfaces, i.e. $d\eta/dx << 1$, such an approach yields good approximations for the wave solution. However, for steep interfaces, i.e. $d\eta/dx >> 1$, the residual (4.36), and so (4.37), can be large since the local-mode representation (4.28). To obtain the final shape of the problem, a linear system of equations is built by plugging the wave representation (4.35) in the Action formula (4.27).

4.2.4   Numerical solution via spectral methods

The final system of equations is arranged in matrix form

$$\mathbf{E_1}\ \mathbf{D}^2\bar{\mathbf{a}} + \mathbf{E_2}\ \mathbf{D}\bar{\mathbf{a}} + \mathbf{E_3}\ \bar{\mathbf{a}}\ = \bar{\mathbf{p}}$$

where the matrices $\mathbf{E_j}$ contains the constants of the differential equation system, for each mode and each discretization point x_n; see appendix B.

Matrix $\mathbf{D}$ represents the derivation operator and can be written by $\mathbf{D_1}$, $\mathbf{D_2}$ matrices which are respectively the derivation and double derivation matrix for the system. The structure is based on the derivation matrix $\mathbf{D_c}$ for Chebyshev-spaced grid points [136].

$$\mathbf{D_1} = \begin{pmatrix} \mathbf{D_c} & 0 \\ 0 & \mathbf{D_c} \end{pmatrix} \quad \mathbf{D_2} = \begin{pmatrix} \mathbf{D_c^2} & 0 \\ 0 & \mathbf{D_c^2} \end{pmatrix}$$

Explicitly the final matrix structure has the form:

$$\mathbf{E_1}\ \mathbf{D_2}\ \bar{\mathbf{a}} + \mathbf{E_2}\ \mathbf{D_2}\ \bar{\mathbf{a}} + \mathbf{E_3}\ \bar{\mathbf{a}} \quad = \quad \bar{\mathbf{p}}$$
$$\mathbf{M}\ \bar{\mathbf{a}} \quad = \quad \bar{\mathbf{p}}$$

with solution

$$\bar{\mathbf{a}} \ = \ \mathbf{M^{-1}}\bar{\mathbf{p}}$$

with

$$\bar{\mathbf{a}} = \begin{pmatrix} A_{1(-L)} \\ A_{1(x_2)} \\ \vdots \\ A_{1(x_{n-1})} \\ \overline{A_{1(L)}} \\ A_{2(-L)} \\ A_{2(x_2)} \\ \vdots \\ A_{2(x_{n-1})} \\ \overline{A_{2(L)}} \\ \vdots \end{pmatrix} \quad \bar{\mathbf{p}} = \begin{pmatrix} I_1 \\ 0 \\ \vdots \\ 0 \\ 0 \\ I_2 \\ 0 \\ \vdots \\ 0 \\ 0 \\ \vdots \end{pmatrix}$$

There is a function A_n for each mode in the expansion. Solutions are obtained via the spectral method, and inserting boundary conditions directly in $\mathbf{E_j}$ matrices.

4.2.5   Applications

The mode was tested for the following set of parameters:

$$\rho_1 = 1600\ Kg/m^3 \quad \beta_1 = \ \ 400\ m/s \tag{4.38}$$
$$\rho_2 = 2400\ Kg/m^3 \quad \beta_2 = 1500\ m/s \tag{4.39}$$

Interface reference depth was fixed at $H = 1.2$ km and the spatial extension of the model is $2L = 6$ km.

To assess reliability, the algorithm was tested on a parallel layer environment and theoretical values were reproduced; then the varying interface was modeled by an half sine-shaped buried hill (see Figure 4.2) with a change of depth equal to 10% H and waves propagate at a given frequency $\omega = 8Hz$. At such a frequency, besides the fundamental mode, 5 higher modes are admissible.

In Figure 4.3, the phase velocity $C_x(x) = \omega/k_n(x)$ of each mode was computed from the analytical model (solid line) and is compared against their "parallel-layered" counterpart (dash line) based on the local wavenumber k_n computed from the dispersion relation 4.29 using the variable upper layer depth $d = \eta(x)$.

Here the wavenumber

$$k_n(x) = k_n(x) + x\frac{dk_n}{dx} + \frac{d\theta_n}{dx} \ , \tag{4.40}$$

where $\theta_n = \tan^{-1}\left(Im(, A_n)/Re(A_n)\right)$ is the phase of the complex amplitude A_n. The numerical phase velocity of each mode exhibits a slightly "ringing" phenomenon near a $2k_n$ wavenumber if compared to the smoother "parallel-layered" counterpart, this is due to the fact that the latter does not account for back-reflections.

Note that the phase velocity of the fundamental mode does not vary laterally and it is almost equal to the speed of SH waves in the upper layer. Indeed, its wavelength ($\lambda \approx 320$ m) is smaller than the interface depth and the fundamental mode is almost insensitive to the presence of the interface. However, lateral inhomogeneity weakly affects the lowermost higher modes which tend to increase their speed as they propagate over shallower regions of the upper layer shortening their wavelengths. Further, figure 4.4 reports the spatial variation of the magnitude of the weighting functions A_n. Note that the amplification of higher modes in the region where the thickness of the upper layer decreases as expected.

The magnitude of the total surface displacements v_{II} in region II and the associated normalized spectrum are plotted respectively in Fig. 4.5 and 4.6 respectively.

4.2.6   Conclusions on the model

This very simplified model presented accounts for many features not yet present in the previous work of Gjevic (1973), namely back-reflections and higher mode coupling. The wave-field was obtained by a matching mode procedure based on Lagrangian minimization. Results of previous works were confirmed.

This method has been proved useful to extend the range of applicability from "weak perturbation" of the interface to moderate slopes. The present model could
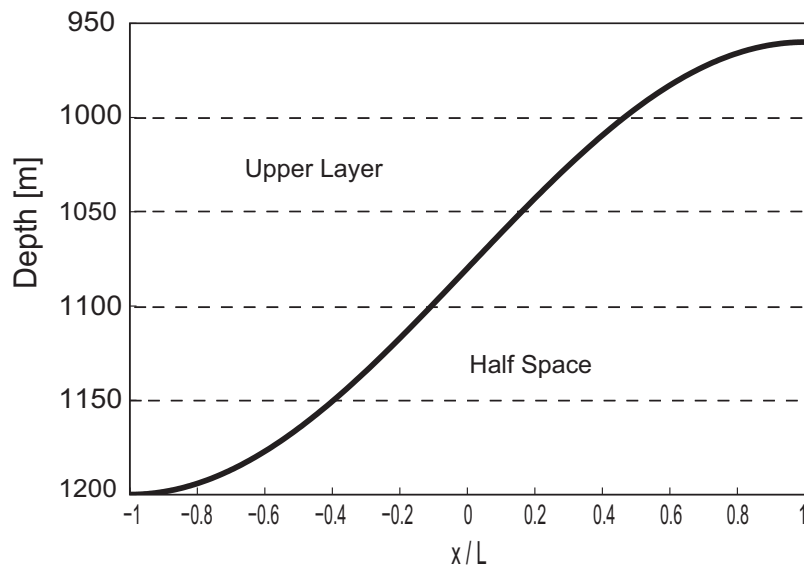
Figure 4.2: 10% slope Interface
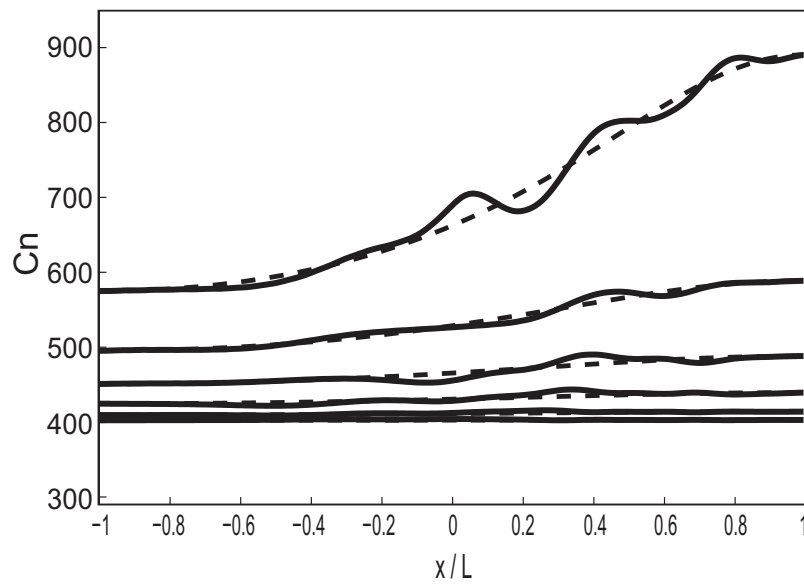
Figure 4.3: Mode velocityes
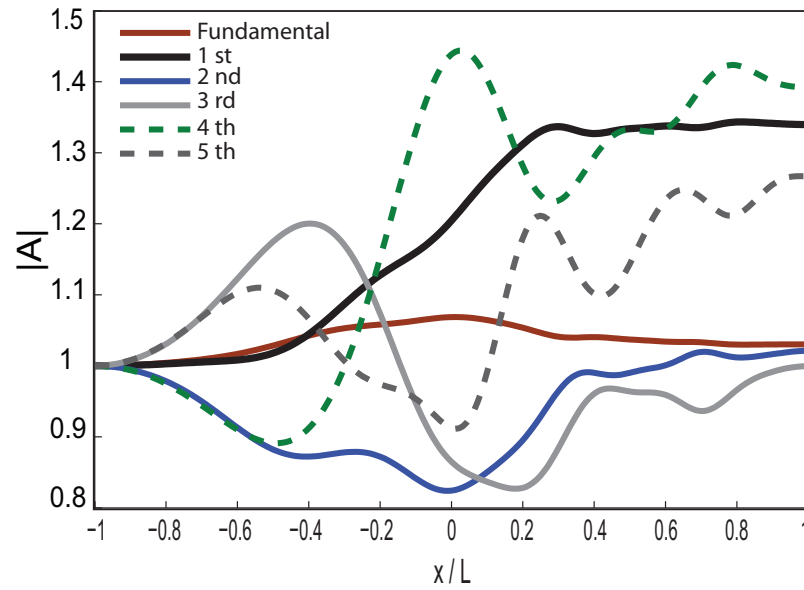
Figure 4.4: Weighting function amplitudes
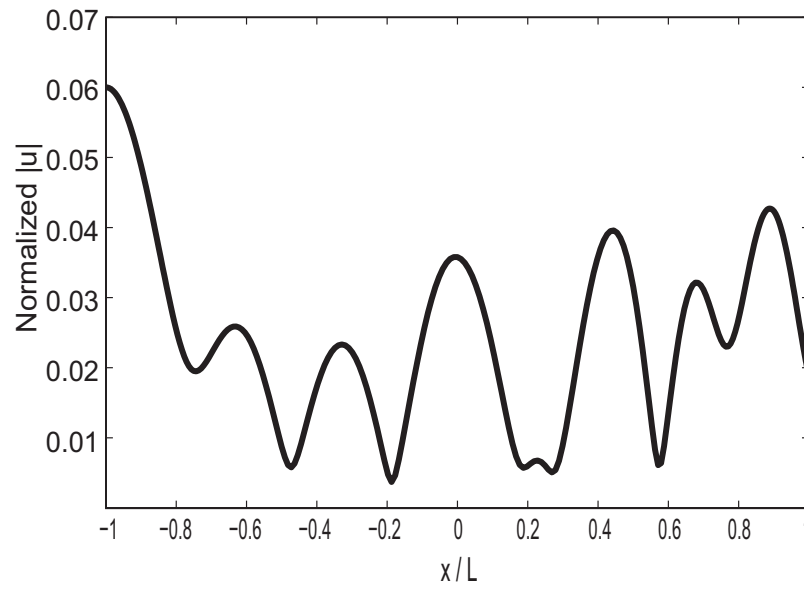
Figure 4.5: Displacement amplitude
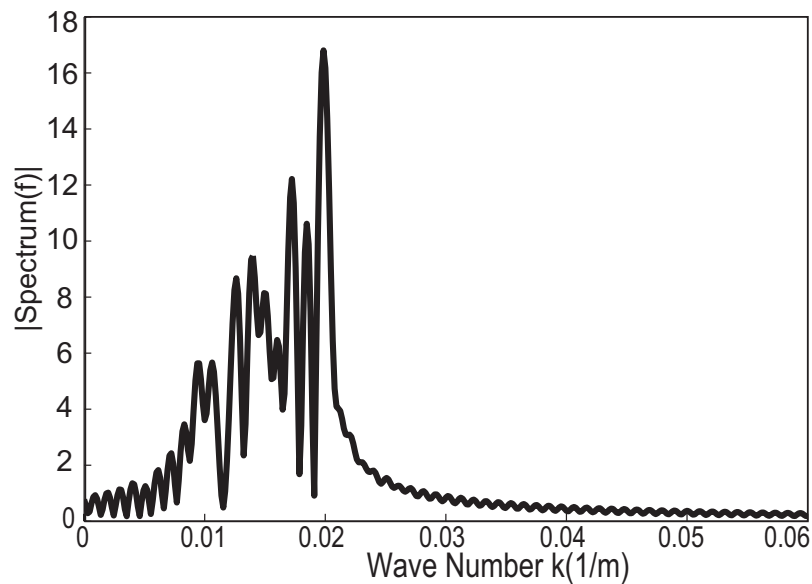
Figure 4.6: Signal spectrum

be generalized for a greater number of layers and since limitations depend strongly on assumed initial ansatz,the use of different functions could broaden the field of applicability. Despite these results and the elegant approach utilized, the drawbacks of the previously mentioned limitations and to difficulty of extending the approach to Rayleigh waves as are the reason that a new model, based on the boundary element method has been adopted.

4.3 The B.E.M. based forward Model.

As a second model for surface displacements calculation, the Boundary Element Method was exploited. The theory of BEM is widely covered in the literature. Early applications date back to 1960 for potential problems. Today, the use of integral boundary equations connected with a boundary discretization is very popular and applications can be found for general potential problems (Brebbia, 1992) as well as for elastostatic (Katsikadelis, 2002) and elastodynamic (Beskos, 1985; Manolis & Beskos ,1988; Dominguez, 1993).

BEM seemed to present the most attractive features to model ground displace-

ment for many reasons. First of all, if we bear in mind that surface waves data are acquired at the free surface and in general an active source is placed on the surface as well, exploiting a method which only requires discretization of boundaries is very appealing. Sources and receivers can be assumed to coincide with the nodes of the discretized soil surface and the solution is directly obtained when nodal displacements are evaluated. As a second point, alternative methods such as FEM or FDM[2], require the discretization of the whole domain. Infinite domains are approximated by the truncation and insertion of an artificial adsorbing boundary. The mathematical machinery of BEM, instead revolves around the Green's function; this assures that radiative conditions are satisfied without the need to deploy a mesh to approximate it. This feature makes it extremely easy to deal with infinite or semi-infinite domains where waves traveling to infinity must fade (Dominguez, 1991). A linear system of equations can be written for each piecewise portion of the subsoil regardless of its shape and different portions can be matched imposing suitable matching boundary conditions (Beskos, Katsikadelis,2002).

As a conclusive consideration, although in the present work a monochromatic signal traveling in a system constituted by a layer over an half space has been investigated, this method is suitable for any number of layers, and multi-frequency environments. The boundary element approach can be easily generalized to three-dimensional modeling; moreover viscoelasticity can be introduced by the elastic-viscoelastic principle of correspondence. Finally BEM can be easily implemented for parallel computing architecture.

4.3.1   The BEM framework

The key step of the BEM is to transform an elastodynamic problem from its differential formulation into an equivalent integral formulation. A differential formulation can be defined more precisely as:

> **Definition 1** *: **Differential Elastodynamic problem***
> *Consider an homogeneous, isotropic elastic body with volume Ω and bounded by a regular surface Γ. The differential elastodynamic problem is defined by the equation of motion 4.41, boundary conditions 4.42 and initial con-*

---

[2]FEM: Finite Element Method; FDM: Finite Difference Method;

ditions 4.43

$$\ddot{u}_j = b_j + (c_p^2 - c_s^2)u_{i,ij} + c_s^2 u_{j,ii} \qquad (4.41)$$

$$
\begin{aligned}
t_{(\hat{\mathbf{N}})i}(\mathbf{x}, t) &= p_i(\mathbf{x}, t); & \mathbf{x} \in \Gamma_t \\
u_i(\mathbf{x}, t) &= q_i(\mathbf{x}, t); & \mathbf{x} \in \Gamma_u
\end{aligned}
\qquad (4.42)
$$

$$
\begin{aligned}
u_i(\mathbf{x}, 0^+) &= u_{0i}(\mathbf{x}); & \mathbf{x} \in \Omega \\
\dot{u}_i(\mathbf{x}, 0^+) &= v_{0i}(\mathbf{x}); & \mathbf{x} \in \Omega ,
\end{aligned}
\qquad (4.43)
$$

where $\Gamma = \Gamma_u \cup \Gamma_t$.

A fully analytical solution can be obtained only in few cases of simple geometry; for complex situations the only feasible approach is numerical. The most effective way to find numerical solution is to translate the differential equations system into an equivalent integral form. The classic strategy is to exploit some form of an integral theorem, in particular as it will be shown soon, for P-SV plain strain and 3D cases, the *Reciprocal theorem* [3] is exploited. This is the dynamic version of the classical reciprocal theorem of Betti-Rayleigh of elastostatics, it was established first by Graffi in 1947 for bounded domains and thus sometimes it is also referred in literature as *Graffi's Reciprocal Theorem*(Graffi, 1946-47). Subsequently it was extended to unbounded domains by Wheeler and Sternberg (1938).

Definition 2 : *Elastodynamic State*
Let Ω *be a spatial region with boundary* Γ, *and* Δ_t *a time interval.*
If $\boldsymbol{u}$ *and* $\boldsymbol{t}$ *are, respectively, a vector-valued and a symmetric second-order tensor valued function defined on* $\Omega \times \Delta_t$, *the ordered pair* $\mathcal{S} = [\boldsymbol{u}, \boldsymbol{t}]$ *is called* elastodynamic state *on* $\Omega \times \Delta_t$ *with the displacement fields* $\boldsymbol{u}$ *and the stress field* $\boldsymbol{t}$, *corresponding to a body force density*[4] $\tilde{\boldsymbol{f}}$, *mass density* ρ, *irrotational wave speed* C_p *and equivoluminal wave speed* C_s, *provided that*

- $\boldsymbol{u} \in \mathcal{C}^{2,2}(\Omega \times \Delta_t)$, $\boldsymbol{u} \in \mathcal{C}^{1,1}(\Gamma \times \Delta_t)$,
  $\boldsymbol{t} \in \mathcal{C}^{0,0}(\Omega \times \Delta_t)$, $\tilde{\boldsymbol{f}} \in \mathcal{C}^{0,0}(\Omega \times \Delta_t)$.

---

[3]In principle this is not the only choice, each integral relation connecting two elastodynamic states could be exploited as well (Manolis & Beskos, 1988).

[4]In definitions 2, 3 and theorem 1, the symbol $\tilde{\boldsymbol{f}}$ refers to a density of force for unit of mass; do not confuse with $\boldsymbol{f} = \rho\tilde{\boldsymbol{f}}$ which indicates volume density force

- *Constants ρ, C_p, C_s are subject to*

$$\rho > 0\,, \qquad C_p > \frac{2}{\sqrt{3}}C_s > 0\,.$$

- $\boldsymbol{u}$,$\boldsymbol{t}$ *and* $\tilde{\boldsymbol{f}}$ *satisfy equations 4.8 and 4.5*

The class of all elastodynamic states satisfying the above conditions is denoted by

$$\mathcal{S} \in \mathcal{E}\left(\tilde{\boldsymbol{f}}\,, \rho, C_p, C_s; \Omega \times \Delta_t\right)\,.$$

Definition 3 : **Quiescent past State**
we say that $\mathcal{S}$ is an elastodynamic state of quiescent past, and denote that

$$\mathcal{S} \in \mathcal{E}_0\left(\tilde{\boldsymbol{f}}\,, \rho, C_p, C_s; \Omega \times \Delta_t\right)\,,$$

when

$$\Delta_t = \Delta_t^\infty \quad and \quad \boldsymbol{u} = \boldsymbol{0} \; on \; \Omega \times \Delta_t^-\,.$$

Theorem 1 : **Graffi's Reciprocal Theorem**
Consider a regular region Ω with the boundary Γ, and two distinct elastodynamic states

$$\begin{aligned} \mathcal{S} &= [\boldsymbol{u}\,, \boldsymbol{\tau}\,] &\in& \quad \mathcal{E}\left(\tilde{\boldsymbol{f}}\,, \rho, C_p, C_s; \Omega \times t^+\right) \\ \mathcal{S}' &= [\boldsymbol{u}', \boldsymbol{\tau}'] &\in& \quad \mathcal{E}\left(\tilde{\boldsymbol{f}}', \rho, C_p, C_s; \Omega \times t^+\right)\,, \end{aligned}$$

defined on the same region with initial conditions in Ω

$$\begin{aligned} \boldsymbol{u}(\mathbf{x}, 0) &= \boldsymbol{u_0}(\mathbf{x}) & \dot{\boldsymbol{u}}(\mathbf{x}, 0) &= \boldsymbol{v_0}(\mathbf{x}) \\ \boldsymbol{u}'(\mathbf{x}, 0) &= \boldsymbol{u_0'}(\mathbf{x}) & \dot{\boldsymbol{u}}'(\mathbf{x}, 0) &= \boldsymbol{v_0'}(\mathbf{x})\,, \end{aligned}$$

then for $t \geq 0$

$$\begin{aligned} \int_\Gamma \left[\boldsymbol{t}_{(\hat{\mathbf{N}})} * \boldsymbol{u}'\right](\mathbf{x}, t)\, d\Gamma + \int_\Omega \rho &\left\{\left[\tilde{\boldsymbol{f}} * \boldsymbol{u}'\right](\mathbf{x}, t)\right. && (4.44) \\ &\left.+ \boldsymbol{v_0}(\mathbf{x}) \cdot \boldsymbol{u}'(\mathbf{x}, t) \, + \, \boldsymbol{u_0}(\mathbf{x}) \cdot \dot{\boldsymbol{u}}'(\mathbf{x}, t)\right\} d\Omega \\ = \int_\Gamma \left[\boldsymbol{t'}_{(\hat{\mathbf{N}})} * \boldsymbol{u}\right](\mathbf{x}, t)\, d\Gamma + \int_\Omega \rho &\left\{\left[\tilde{\boldsymbol{f}}' * \boldsymbol{u}\right](\mathbf{x}, t)\right. \\ &\left.+ \boldsymbol{v_0'}(\mathbf{x}) \cdot \boldsymbol{u}(\mathbf{x}, t) \, + \, \boldsymbol{u_0'}(\mathbf{x}) \cdot \dot{\boldsymbol{u}}(\mathbf{x}, t)\right\} d\Omega\,, \end{aligned}$$

where $\boldsymbol{t}_{(\hat{\mathbf{N}})} = \boldsymbol{\tau}\hat{\mathbf{N}}\,, \boldsymbol{t'}_{(\hat{\mathbf{N}})} = \boldsymbol{\tau}'\hat{\mathbf{N}}$ are tractions of states $\mathcal{S}$, $\mathcal{S}'$ on the boundary.

Theorem 1 establishes a conservation of virtual work obtained multiplying tensions of state $\mathcal{S}$ with displacements of state $\mathcal{S}'$ and its analogous with interchanged states. *Time domain boundary element method* is built starting directly from 4.44, discretizing both space and time. The drawback of this approach is that discrete convolutions are involved and the approach is usually stable only for very short times; consequently, this approach is more suitable to investigate transients.

An alternative approach is to transform 4.44 by means of Laplace or Fourier transformation, reducing convolutions to simple multiplications. In both cases this is referred as *frequency domain boundary element method*; this last option will be considered.

4.3.2   Frequency domain boundary element method

Consider the general form of the Fourier transform

$$\bar{\bar{\mathscr{F}}}(\mathbf{x}, \omega) = \int_{-\infty}^{\infty} \mathscr{F}(\mathbf{x}, t) e^{-i\omega t} dt \ ,$$

equations 4.41 - 4.43 recasts[5]

$$-\omega^2 \, \bar{u}_j = \bar{b}_j + (c_p^2 - c_s^2)\bar{u}_{i,ij} + c_s^2 \bar{u}_{j,ii} \qquad (4.45)$$

$$\begin{aligned}
\bar{t}_{(\hat{\mathbf{N}})i}(\mathbf{x}, \omega) &= \bar{p}_i(\mathbf{x}, \omega); \quad \mathbf{x} \in \Gamma_t \\
\bar{u}_i(\mathbf{x}, \omega) &= \bar{q}_i(\mathbf{x}, \omega); \quad \mathbf{x} \in \Gamma_u \ .
\end{aligned} \qquad (4.46)$$

$$(4.47)$$

Helmholtz decomposition of sec. 4.1 holds in frequency domain, thus two-dimensional approximations can be considered. SH-waves and P-SV cases involves two separate BEM.

In case of SH-Waves, in order to transform the anti-plane strain differential equation 4.13 into its integral counterpart it is sufficient to exploit the Green's second identity. SH waves are not of primary interest in this work, but integral equations and fundamental solutions are introduced in appendix B for the sake of completeness.

The P-SV(2D plane strain) and the full 3D case share the same Integral formulation. Recalling properties of convolution with respect to Fourier transforms and imposing the condition of quiescent past for states $\mathcal{S},\mathcal{S}'$, the Graffi equation 4.44 in

---

[5]bars indicates fourier transformed quantities.

frequency domain is obtained.

$$\int_{\Gamma} \left[\bar{\boldsymbol{t}}_{(\hat{\mathbf{N}})} \cdot \bar{\boldsymbol{u}}' \right] (\mathbf{x}, t) \, d\Gamma + \int_{\Omega} \left[\bar{\boldsymbol{f}} \cdot \bar{\boldsymbol{u}}' \right] (\mathbf{x}, t) \Omega \tag{4.48}$$

$$= \int_{\Gamma} \left[\bar{\boldsymbol{t}}'_{(\hat{\mathbf{N}})} \cdot \bar{\boldsymbol{u}} \right] (\mathbf{x}, t) \, d\Gamma + \int_{\Omega} \left[\bar{\boldsymbol{f}}' \cdot \bar{\boldsymbol{u}} \right] (\mathbf{x}, t) d\Omega \,,$$

with

$$\mathcal{E}_0 \left(\tilde{\boldsymbol{f}} \,, \rho, C_p, C_s; \Omega \times t^+ \right) \tag{4.49}$$

$$\mathcal{E}_0 \left(\tilde{\boldsymbol{f}}', \rho, C_p, C_s; \Omega \times t^+ \right) \,, \tag{4.50}$$

where $\bar{\boldsymbol{f}} = \rho \bar{\tilde{\boldsymbol{f}}}$, $\bar{\boldsymbol{f}}' = \rho \bar{\tilde{\boldsymbol{f}}}'$.

This equation relates two elastic states. $\mathcal{S}'$ is then assumed to be the state produced by a localized unit force $\bar{\boldsymbol{f}}' = \delta(\mathbf{x} - \mathbf{s})\hat{\mathbf{e}}$ applied at the point $\mathbf{s}$. The solution of eq. 4.45 satisfying this request is called Green's function (or fundamental function) of the system. Each orientation of the load can be expressed by a linear composition of the Green's functions calculated with the direction of the load $\hat{\mathbf{e}}$ parallel to the main axes. Green's functions can therefore be rearranged in a tensor form. The fundamental tensor notation both for displacements and tensions is

$$\boldsymbol{U}_{ji}(\mathbf{x}, \mathbf{s}) \,, \qquad\qquad \boldsymbol{T}_{ji}(\mathbf{x}, \mathbf{s}) \,, \tag{4.51}$$

which indicates the ith displacements/tensions component at location $\mathbf{x}$ produced by the source located in $\mathbf{s}$, with loading force directed as $\hat{\mathbf{e}}_{\mathbf{j}}$. Green's functions are available in literature both for 2D and 3D cases, unfortunately they were reported incorrectly in different articles, therefore to avoid confusion they were re-derived. A correct version is available in Dominguez (1984) or alternatively in appendix C.

By inserting Fundamental solutions in 4.48, neglecting internal forces for state $\mathcal{S}$ and noting that

$$\int_{\Omega} \left[\bar{\boldsymbol{f}}' \cdot \bar{\boldsymbol{u}} \right] (\mathbf{x}, \omega) d\Omega \;=\; \int_{\Omega} \delta(\mathbf{x} - \mathbf{s}) \hat{\mathbf{e}}_{\mathbf{j}} \cdot \bar{\boldsymbol{u}}(\mathbf{x}, \omega) d\Omega \;=\; \bar{\boldsymbol{u}}(\mathbf{s}, \omega) \cdot \hat{\mathbf{e}}_{\mathbf{j}} \,, \tag{4.52}$$

the final integral form is obtained

$$\int_{\Gamma} \boldsymbol{U}(\mathbf{x}, \mathbf{s}, \omega) \bar{\boldsymbol{t}}_{(\hat{\mathbf{N}})}(\mathbf{x}, \omega) \, d\Gamma = \int_{\Gamma} \boldsymbol{T}(\mathbf{x}, \mathbf{s}, \omega) \bar{\boldsymbol{u}}(\mathbf{x}, \omega) \, d\Gamma + \boldsymbol{\varrho}(\mathbf{s}) \bar{\boldsymbol{u}}(\mathbf{s}, \omega) \,. \tag{4.53}$$

Equation 4.53 relates displacements of an internal point $\mathbf{s}$ of Ω with values of fields at boundaries; for this case $\boldsymbol{\varrho}(\mathbf{s}) = \mathbb{I}$.

The point can be conceptually directed towards the boundary; eventually it can reach Γ leading to an expression which depends only on quantity evaluated at the boundary. It is noteworthy that fundamental solutions 4.51, in appendix C depend on the distance $r = \|\mathbf{x} - \mathbf{s}\|$ and the latter goes to zero if $\mathbf{s}$ belongs to the boundary. Integrals in eq. 4.53 then become singular and have to be evaluated in Cauchy's principal value sense. Recalling eq. 4.52 it can be shown (Dominguez, 1993) that for smooth boundary

$$\boldsymbol{\varrho}(\mathbf{s}) = \left\{ \begin{array}{ll} \mathbb{I} & \mathbf{s} \in \Omega \\ \mathbf{0} & \mathbf{s} \notin \Omega \\ [\boldsymbol{c}] & \mathbf{s} \in \Gamma \end{array} \right. ,$$

where $[\boldsymbol{c}]$ is a 2×2 matrix of coefficients that have to be calculated exploiting zero stress rigid body translation considerations.

Approximated Solution

So far only the suitable integral equation was derived. In order to obtain numerical solutions it is necessary to approximate integrals of eq. 4.53. The boundary is approximated as small elements, each one defined by one or more points (nodes) and spatial variation of fields on each element is obtained by polynomial interpolation of the field nodal values. Higher degrees of the interpolating functions corresponds to a higher number of nodes per element.

Since integration path is intended counter-clockwise, both elements and nodes are numerated accordingly. Integrals in equation 4.53 are converted to sums on all of the elements.

$$\sum_{k=1}^{n_e} \int_{\Delta_e} \boldsymbol{T}(\mathbf{x}, \mathbf{s}, \omega) \bar{\boldsymbol{u}}(\mathbf{x}) \, de \, + \, \boldsymbol{\varrho}(\mathbf{s}) \bar{\boldsymbol{u}}(\mathbf{s}) = \sum_{k=1}^{n_e} \int_{\Delta_e} \boldsymbol{U}(\mathbf{x}, \mathbf{s}, \omega) \bar{\boldsymbol{t}}_{(\hat{\mathbf{N}})}(\mathbf{x}) \, de \, , \qquad (4.54)$$

where n_e is the total number of elements and Δ_e is the element surface[6]. The complexity of the BEM depends now on the particular choice of collocation and interpolation.

Element Technology

Elements can be classified according the kind of interpolation law exploited.

---

[6]Here we refer to surface element because so far the formulation is valid both for 2D and 3D regions.

Element Classification		
Element Kind	Fields Interpolating functions	Number of Nodes
Constant	No interpolation	1
Linear	linear	2
Parabolic	quadratic	3

Elements involving two or more nodes can be defined as continuous or discontinuous depending on whether or not there are nodes placed at their extremes. The method of discontinuous elements is widely exploited in cracks evaluation (Portela, 1992), indeed, since this approach allows collocation of nodes inside the element, it avoids numerical singularities at crack tips or at boundary edges, assuring the continuity of interpolated fields.

The geometry of the element can be defined by nodal coordinate values interpolation as well; in this way parabolic shaped elements (3 nodes) or splines (5 nodes) can be exploited to better approximate curved portions of Γ.

General interpolations for boundary geometry and fields on each element takes the
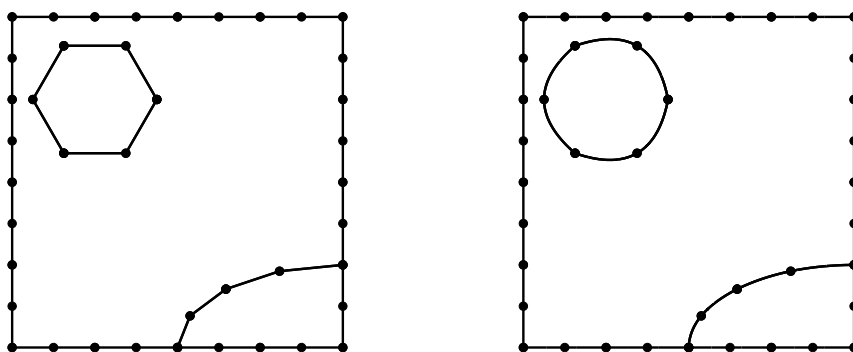
(a) Linear Elements   (b) Quadratic Elements.

Figure 4.7: Example of Domain Discretizations

form

$$\mathbf{x} = \sum_{n=1}^{n_n} P_n^g(\eta)\mathbf{x}_n \ , \qquad \boldsymbol{F}(\mathbf{x}) = \sum_{n=1}^{n_n} P_n^f(\eta)\boldsymbol{F}(\mathbf{x}_n) \ , \qquad (4.55)$$

where η ranges between two values $\eta \in [\eta_{\min}, \eta_{\max}]$, n_n is the number of nodes on the element; P_n^g, P_n^f are two sets of interpolating functions and $\boldsymbol{F}$ indicates a general vector field. Let d_g and d_f be respectively the degree of the interpolating functions for the geometry P_n^g and for the fields P_n^f; the element is said to be:

$$
\begin{array}{lll}
Subparametric & \text{if} & d_f > d_g \\
Isoparametric & \text{if} & d_f = d_g \\
Iperparametric & \text{if} & d_f < d_g
\end{array}
$$

(a) $P_1(\eta)$ (b) $P_2(\eta)$ (c) $P_3(\eta)$
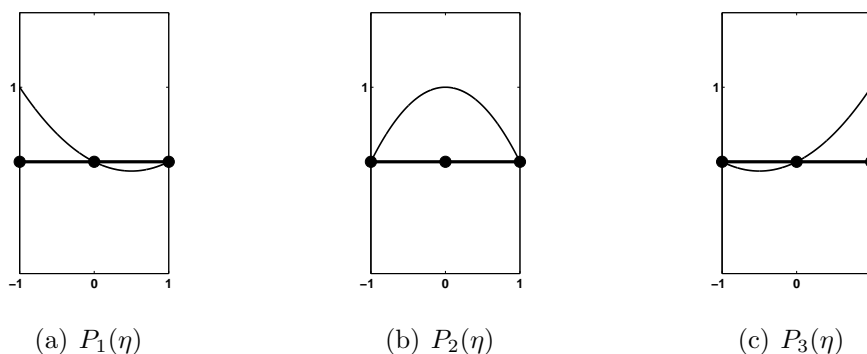
Figure 4.8: Weighting functions for QCE

(a) $P_1(\eta)$ (b) $P_2(\eta)$ (c) $P_3(\eta)$
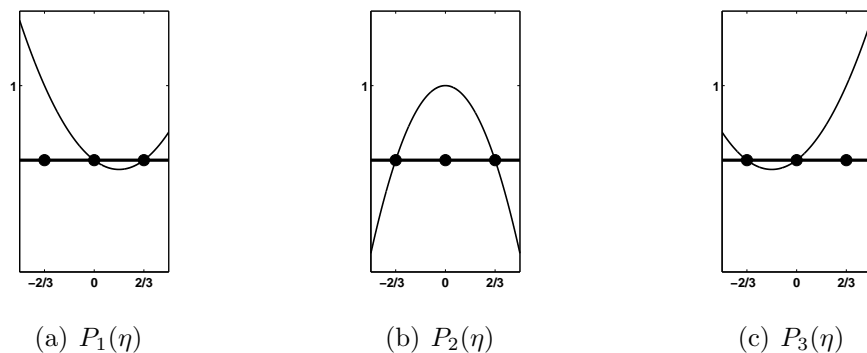
Figure 4.9: Weighting functions for QDE

Here mainly isoparametric quadratic continuous elements (QCE), (Manolis & Beskos, 1983) will be exploited. Isoparamatric quadratic discontinuous elements (QDE), (Portela, 1992) are introduced only as a valid solution in case of a non-flat soil

surface. Interpolated quantities in both case have the same form, eq. 4.55 is then written

$$\mathbf{x}_k(\eta) \;=\; \sum_{n=1}^{3} P_n(\eta)\mathbf{x_{kn}} \tag{4.56}$$

$$\bar{\boldsymbol{u}}_k(\eta) \;=\; \sum_{n=1}^{3} P_n(\eta)\boldsymbol{u_{kn}} \tag{4.57}$$

$$\bar{\boldsymbol{t}}_k(\eta) \;=\; \sum_{n=1}^{3} P_n(\eta)\boldsymbol{t_{kn}} \tag{4.58}$$

where $-1 \leq \eta \leq 1$, $\boldsymbol{u_{kn}} = \bar{\boldsymbol{u}}(\mathbf{x}_n)$ and $\boldsymbol{t_{kn}} = \bar{\boldsymbol{t}}(\mathbf{x}_n)$ on the $\boldsymbol{k}^{\text{th}}$ element.
Figures 4.3.2 - 4.3.2, depict interpolating functions (see table 4.1) vs local elements coordinate η.

Int. Funct.	QCE	QDE
$P_1(\eta)$	$-\dfrac{\eta}{2} + \dfrac{\eta^2}{2}$	$-\dfrac{3}{4}\eta + \dfrac{9}{8}\eta^2$
$P_2(\eta)$	$1 - \eta^2$	$1 - \dfrac{9}{4}\eta^2$
$P_3(\eta)$	$\dfrac{\eta}{2} + \dfrac{\eta^2}{2}$	$\dfrac{3}{4}\eta + \dfrac{9}{8}\eta^2$

Table 4.1: Element weighting functions

The Linear system of equations

By introducing 4.56-4.58 into 4.54, nodal values of fields factors out. Due to the change of reference, from the principal axes $\mathscr{R} = \{\boldsymbol{e}_1, \boldsymbol{e}_2\}$ to the element's local system of coordinate defined by $\mathscr{R}_e = \{\eta : \eta \in [-1, 1]\}$, it is necessary to introduce

the Jacobian of the transformation $J(\eta)$.

$$\sum_{k=1}^{n_e}\sum_{n=1}^{3}\left(\int_{-1}^{1}\boldsymbol{T}(\mathbf{x}_k(\eta),\mathbf{s},\omega)P_n(\eta)J(\eta)\,d\eta\right)\boldsymbol{u_{kn}} + \varrho(\mathbf{s})\boldsymbol{u_s} = \qquad (4.59)$$

$$\sum_{k=1}^{n_e}\sum_{n=1}^{3}\left(\int_{-1}^{1}\boldsymbol{U}(\mathbf{x}_k(\eta),\mathbf{s},\omega)P_n(\eta)J(\eta)\,d\eta\right)\boldsymbol{t_{kn}} ,$$

where $\boldsymbol{u_s} = \bar{\boldsymbol{u}}(\mathbf{s})$ was defined.

Formula 4.59 is now specialized for 2D domains and represents two coupled equations. If now the source $\mathbf{s}$ is cycled to coincide each time with one node at the boundary, a system of equations is obtained. In order to better describe this procedure lets drop dependencies from space and frequency and define the *Influence coefficients* (4.60).

$$[\mathcal{U}_{kn}^s]_{ji} = \int_{-1}^{1}U_{ji}(\mathbf{x}_k(\eta),\mathbf{s},\omega)P_n(\eta)J(\eta)d\eta \qquad (4.60)$$

$$[\mathcal{T}_{kn}^s]_{ji} = \int_{-1}^{1}T_{ji}(\mathbf{x}_k(\eta),\mathbf{s},\omega)P_n(\eta)J(\eta)d\eta ,$$

where upper indexes are integer numbers. In particular $k \in [1, n_e]$ is the element number, $n \in \{1, 2, 3\}$ is the node on the element and $s \in [1, n_n]$ is the node where the source is located.
Emphasizing components, equation 4.59 takes the form

$$\sum_{k=1}^{n_e}\sum_{n=1}^{3}[\mathcal{T}_{kn}^s]_{ji}\,u_{kn_i} + \varrho_{ij}\delta_{ij}\delta(\mathbf{x}-\mathbf{s})u_{s_j} = \sum_{k=1}^{n_e}\sum_{n=1}^{3}[\mathcal{U}_{kn}^s]_{ji}\,t_{kn_i} , \qquad (4.61)$$

explicitly, for each source location we have a couple of equations 4.62

$$\sum_{k=1}^{n_e}\sum_{n=1}^{3}\begin{bmatrix}[\mathcal{T}_{kn}^s]_{11} & [\mathcal{T}_{kn}^s]_{12}\\ [\mathcal{T}_{kn}^s]_{21} & [\mathcal{T}_{kn}^s]_{22}\end{bmatrix}\begin{bmatrix}u_{kn_1}\\ u_{kn_2}\end{bmatrix} + \frac{1}{2}\begin{bmatrix}u_{s_1}\\ u_{s_2}\end{bmatrix}\delta(\mathbf{x}-\mathbf{s})$$

$$= \sum_{k=1}^{n_e}\sum_{n=1}^{3}\begin{bmatrix}[\mathcal{U}_{kn}^s]_{11} & [\mathcal{U}_{kn}^s]_{12}\\ [\mathcal{U}_{kn}^s]_{21} & [\mathcal{U}_{kn}^s]_{22}\end{bmatrix}\begin{bmatrix}t_{kn_1}\\ t_{kn_2}\end{bmatrix} , \qquad (4.62)$$

which depends only on source and element nodes positions. The set of equation can be rearranged in an elegant matrix form

$$[\boldsymbol{H}]\{\mathbf{u}\} = [\boldsymbol{G}]\{\mathbf{t}\} \qquad (4.63)$$

where the matrix structure is sketched only for $[\boldsymbol{H}]$, both for the QCE (4.64) case and for QDE (4.65), being the same for $[\boldsymbol{G}]$ provided we change the $\mathcal{T}$ symbol to $\mathcal{U}$.

$$[\boldsymbol{H}] = \begin{pmatrix} \begin{matrix} \left[\mathcal{T}_{11}^1\right]\left[\mathcal{T}_{12}^1\right]\left[\mathcal{T}_{13}^1+\mathcal{T}_{21}^1\right]\left[\mathcal{T}_{22}^1\right] \\ \left[\mathcal{T}_{11}^2\right]\left[\mathcal{T}_{12}^2\right]\left[\mathcal{T}_{13}^2+\mathcal{T}_{21}^2\right]\left[\mathcal{T}_{22}^2\right] \quad \cdots \\ \left[\mathcal{T}_{11}^3\right]\left[\mathcal{T}_{12}^3\right]\left[\mathcal{T}_{13}^3+\mathcal{T}_{21}^3\right]\left[\mathcal{T}_{22}^3\right] \\ \left[\mathcal{T}_{11}^4\right]\left[\mathcal{T}_{12}^4\right]\left[\mathcal{T}_{13}^4+\mathcal{T}_{21}^4\right]\left[\mathcal{T}_{22}^4\right] \\ \quad\quad \vdots \quad\quad\quad\quad \ddots \\ \quad\quad\quad\quad \left[\mathcal{T}_{(n_e-1)3}^{n_n}+\mathcal{T}_{n_e1}^{n_n}\right]\left[\mathcal{T}_{n_e2}^{n_n}\right]\left[\mathcal{T}_{n_e3}^{n_n}\right] \end{matrix} \end{pmatrix} , \qquad (4.64)$$

$$[\boldsymbol{H}] = \begin{pmatrix} \begin{matrix} \left[\mathcal{T}_{11}^1\right]\left[\mathcal{T}_{12}^1\right]\left[\mathcal{T}_{13}^1\right]\left[\mathcal{T}_{21}^1\right]\left[\mathcal{T}_{22}^1\right] \\ \left[\mathcal{T}_{11}^2\right]\left[\mathcal{T}_{12}^2\right]\left[\mathcal{T}_{13}^2\right]\left[\mathcal{T}_{21}^2\right]\left[\mathcal{T}_{22}^2\right] \quad \cdots \\ \left[\mathcal{T}_{11}^3\right]\left[\mathcal{T}_{12}^3\right]\left[\mathcal{T}_{13}^3\right]\left[\mathcal{T}_{21}^3\right]\left[\mathcal{T}_{22}^3\right] \\ \left[\mathcal{T}_{11}^4\right]\left[\mathcal{T}_{12}^4\right]\left[\mathcal{T}_{13}^4\right]\left[\mathcal{T}_{21}^4\right]\left[\mathcal{T}_{22}^4\right] \\ \quad\quad \vdots \quad\quad\quad\quad \ddots \\ \quad\quad\quad\quad \left[\mathcal{T}_{(n_e-1)3}^{n_n}\right]\left[\mathcal{T}_{n_e1}^{n_n}\right]\left[\mathcal{T}_{n_e2}^{n_n}\right]\left[\mathcal{T}_{n_e3}^{n_n}\right] \end{matrix} \end{pmatrix} , \qquad (4.65)$$

and

$$\{\mathbf{u}\} = \begin{pmatrix} \boldsymbol{u}(n_1) \\ \boldsymbol{u}(n_2) \\ \boldsymbol{u}(n_3) \\ \vdots \\ \boldsymbol{u}(n_n-1) \\ \boldsymbol{u}(n_n) \end{pmatrix} , \quad \{\mathbf{t}\} = \begin{pmatrix} \boldsymbol{t}(n_1) \\ \boldsymbol{t}(n_2) \\ \boldsymbol{t}(n_3) \\ \vdots \\ \boldsymbol{t}(n_n-1) \\ \boldsymbol{t}(n_n) \end{pmatrix} , \qquad (4.66)$$

are displacements and tensions at the nodes.

All matrices in 4.63 are $[2\,n_n \times 2\,n_n]$ dense. The machinery of BEM for one domain is completed when boundary conditions are imposed. Lets assume that displacements (but not tensions) are known on Γ_u and tensions (but not displacements) are known on Γ_t, with $\Gamma = \Gamma_u \cup \Gamma_t$, so there are n_n known nodal values to exploit. Then moving on the right all products involving known nodal quantities and leaving unknown nodal values on the left, eq. 4.63 recasts in form of linear system of equations

$$[\mathbf{A}]\,\{\mathbf{X}\} = \{\mathbf{B}\} \ , \qquad (4.67)$$

which solution gives the unknown nodal values of the fields.

NOTE: Equation 4.62 and 4.66 actually are expressed by two different notations. QCE adjacent elements always share a node, therefore there is not one to one correspondence. Let E_k and E_{k+1} be two consecutive

Node numbering correspondences		
$\boldsymbol{u}(node_{\#})$	QCE $\boldsymbol{u_{kn}}$	QDE $\boldsymbol{u_{kn}}$
$\boldsymbol{u}(n_1)$	$\boldsymbol{u_{11}}$	$\boldsymbol{u_{11}}$
$\boldsymbol{u}(n_2)$	$\boldsymbol{u_{12}}$	$\boldsymbol{u_{12}}$
$\boldsymbol{u}(n_3)$	$\boldsymbol{u_{13}}, \ \boldsymbol{u_{21}}$	$\boldsymbol{u_{13}}$
$\boldsymbol{u}(n_4)$	$\boldsymbol{u_{22}}$	$\boldsymbol{u_{21}}$
$\boldsymbol{u}(n_5)$	$\boldsymbol{u_{23}}, \ \boldsymbol{u_{31}}$	$\boldsymbol{u_{22}}$
$\boldsymbol{u}(n_6)$	$\boldsymbol{u_{32}}$	$\boldsymbol{u_{23}}$
$\vdots$	$\vdots$	$\vdots$
$\boldsymbol{u}(n_{(n-2)})$	$\boldsymbol{u_{(n_e-1)2}}, \ \boldsymbol{u_{n_e1}}$	$\boldsymbol{u_{n_e1}}$
$\boldsymbol{u}(n_{(n-1)})$	$\boldsymbol{u_{n_e2}}$	$\boldsymbol{u_{n_e2}}$
$\boldsymbol{u}(n_n)$	$\boldsymbol{u_{n_e3}}$	$\boldsymbol{u_{n_e3}}$

Table 4.2: Correspondence between node numbering and equation 4.62

elements, then the contribution of the shared node will be evaluated twice, the first time being *node number 3 on E_k* and the second time being *node number 1 on E_{k+1}*. QCE elements instead have no shared nodes and posses a one to one correspondence. The relationship between these two notations are sketched in table 4.2.

Matching boundary conditions

In previous sections the BEM method for a single domain was developed. In order now to investigate piecewise solids, boundary conditions have to be imposed to match regions with different elastic properties. Continuity of displacements and normal stresses at the shared boundary is required, then for each couple of domains Ω_j, Ω_{j+1} with interface Γ_j the following *matching conditions* will be imposed at each shared node.

$$
\begin{aligned}
\left[\boldsymbol{u}(n_i)\right]_{\Gamma_j} &= 0 \\
\left[\boldsymbol{t}(n_i)\right]_{\Gamma_j} &= 0 \,,
\end{aligned}
\tag{4.68}
$$

$$
\forall \, n_i \in \Gamma_j \,,
$$

where $[\mathbf{a}]_\Gamma$ is the jump operator (sec. 4.2.1). An explicit procedure for general problems can be found in the book by Katsikadelis (2002) [61]; alternatively for layered

media oriented problems, see Beskos, 1986[13].

Finally, source intensity, source orientation and zero surface stress were indicated as boundary conditions to solve the BEM integral equation. Weight drop, sledge hammer or a gun shot can be modeled in Fourier's space as a nodal stress vector of intensity $f_0(\omega)$ and perpendicular to the soil surface. More complicate cases such as, for example, an explosion, the portion of the surface corresponding to the source can be modeled as a semicircle and radial nodal stresses must be imposed. For massive sources such as, for example, an electro-mechanical shaker the corresponding compatibility and equilibrium conditions are:

$$\boldsymbol{u}_s = \left\{ \begin{array}{c} 0 \\ \Delta_y \end{array} \right\} \tag{4.69}$$

$$\boldsymbol{F} = -m\omega^2\Delta_y + \boldsymbol{t}_s \tag{4.70}$$

where $\boldsymbol{t}_s$ is the stress at the interface between the shaker and the ground, $\boldsymbol{F}$ is the force produced by the shaker and m is the shaker's mass. These extra equations couple stress and strain at source's location and the linear system for the first layer

$$[\mathbf{H}]\,\bar{\mathbf{u}} \;\; = \;\; [\mathbf{G}]\,\bar{\mathbf{t}}\,,$$

changes to

$$\begin{bmatrix} \mathbf{H_{ss}} & \mathbf{H_{s1}} & \mathbf{H_{s2}} \\ \mathbf{H_{1s}} & \mathbf{H_{11}} & \mathbf{H_{12}} \\ \mathbf{H_{2s}} & \mathbf{H_{21}} & \mathbf{H_{22}} \end{bmatrix} \left\{ \begin{array}{c} \boldsymbol{\Delta} \\ \mathbf{u_1} \\ \mathbf{u_2} \end{array} \right\} = \begin{bmatrix} \mathbf{G_{ss}} & \mathbf{G_{s1}} & \mathbf{G_{s2}} \\ \mathbf{G_{1s}} & \mathbf{G_{11}} & \mathbf{G_{12}} \\ \mathbf{G_{2s}} & \mathbf{G_{21}} & \mathbf{G_{22}} \end{bmatrix} \left\{ \begin{array}{c} \mathbf{t_s}(\boldsymbol{\Delta}) = \boldsymbol{F} + m\omega^2\boldsymbol{\Delta} \\ \mathbf{t_1} \\ \mathbf{t_2} \end{array} \right\},$$

finally,

$$\begin{bmatrix} [\mathbf{H_{ss}} + m\omega^2\mathbf{G_{ss}}] & \mathbf{H_{s1}} & \mathbf{H_{s2}} \\ [\mathbf{H_{1s}} + m\omega^2\mathbf{G_{1s}}] & \mathbf{H_{11}} & \mathbf{H_{12}} \\ [\mathbf{H_{2s}} + m\omega^2\mathbf{G_{2s}}] & \mathbf{H_{21}} & \mathbf{H_{22}} \end{bmatrix} \left\{ \begin{array}{c} \boldsymbol{\Delta} \\ \mathbf{u_1} \\ \mathbf{u_2} \end{array} \right\} = \begin{bmatrix} \mathbf{G_{ss}} & \mathbf{G_{s1}} & \mathbf{G_{s2}} \\ \mathbf{G_{1s}} & \mathbf{G_{11}} & \mathbf{G_{12}} \\ \mathbf{G_{2s}} & \mathbf{G_{21}} & \mathbf{G_{22}} \end{bmatrix} \left\{ \begin{array}{c} F \\ \mathbf{t_1} \\ \mathbf{t_2} \end{array} \right\},$$

here H_{ab} (G_{ab}) is the interaction matrix of a node (cycling source) on the portion a of the boundary, with the receiving node on portion b. Subscript s indicate that the node is one in the source's boundary portion (vibrating machine location), 1 indicates the free surface and 2 indicates interface with the half-space.

4.3.3 The Final Framework

Commercial algorithms capable of performing Elastodynamic calculations already exist; unfortunately however, their main drawback is that there are no source codes available and therefore it is impossible to make modifications to suit the approach followed in this dissertation. To test the ideas introduced so far a code was initially
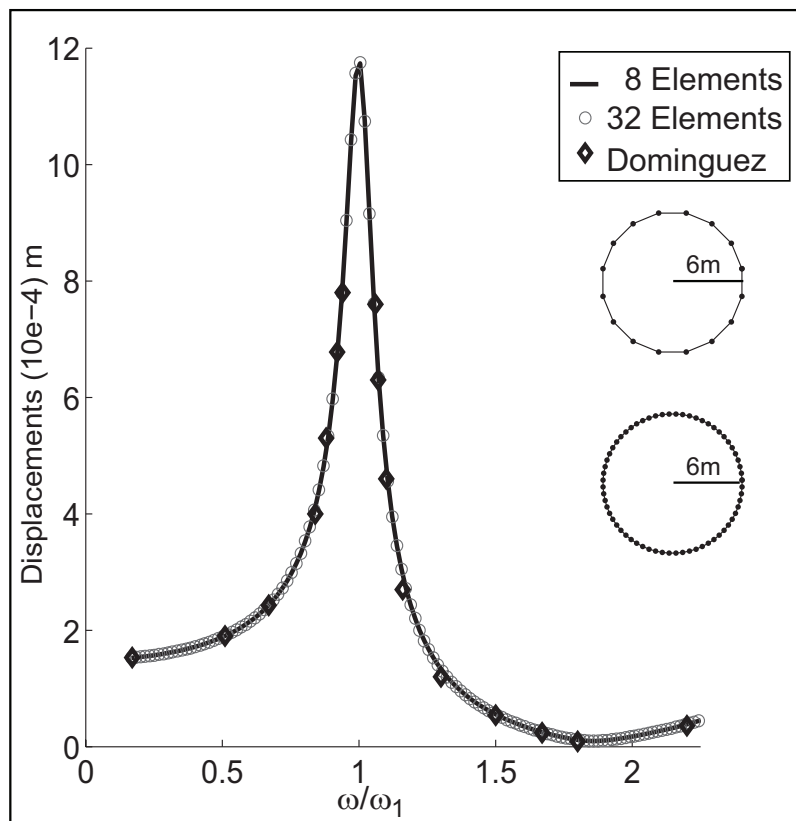
Figure 4.10: Displacements on Infinite cylinder surface under normal stress obtained with 8 and 32 element discretization

written in Matlab. Unfortunately due to the "interpretive" nature of the Matlab language this first routine turned out to be unexpectedly slow. To speed up the computations the code was optimized to run in the parallel environment of Matlab, and calculation of influence coefficients was implemented in a C-language MEX file, this solution was able to reduce the computation time by two order of magnitude. Further developments in full C-language are currently under consideration.

Once implemented, the code was tested on a simple problem (example N. 4, Dominguez, 1993) for which an analytical solution is available. Testing consisted of evaluating radial displacements on an infinitely long cylinder surface assuming a $p = 100N/m^2$ normal Stress. Elastic characteristics of the cylinder were assumed:

$$
\begin{array}{lccl}
\text{Density} & \rho & = & 100kg/m^3 \\
\text{Shear modulus} & \mu & = & 10^6 N/m^2 \\
\text{Poisson's Ratio} & \nu & = & 0.25 \\
\text{Damping Ratio} & \beta_r & = & 0.05
\end{array}
$$

Displacements were calculated for different values of frequency $10 < \omega < 150$. Analytical solution (Kitahara, 1984) prescribes a resonance effect for $\omega_1 = 59.733$, $\omega_2 = 85.6$, $\ldots s^{-1}$. As can be seen in figure 4.10 the implemented code reproduced the results.

Chapter 5

Numerical Inversion.

5.1 Inverse Methods Framework.

Physical theories allow a quantitative interpretation of the real world and permit the interpretation of results obtained by experiments. A model is an ideal approximation of a real system which still retains the main features of the original observed system. Actually modelization is the tool by means of which the physical theory is applied to predict the outcome of some measurements. Further comparison of model results and experimental evidence allows us to determine whether to accept or discard the theory. In this sense the process of starting from an initial model setup and exploiting physical laws to make predictions is called either the "modelization problem", the "simulation problem" or the "forward problem".

The approach is schematically described by

Model Parameters $\rightarrow$ **Forward problem** $\rightarrow$ **Theoretical solution**

Ideally if the set of all model parameters $\boldsymbol{M}$ is defined, the forward problem can be symbolically described by an operator equation:

$$\mathbf{m} \rightarrow \mathbf{d} = A(\mathbf{m}), \quad \text{with} \quad \mathbf{m} \in \boldsymbol{M}. \tag{5.1}$$

The *inverse problem* on the other hand consist in exploiting the real observed data to infer on plausible model parameters. Schematically:

Plausible Model Parameters $\rightarrow$ **Inverse Model** $\rightarrow$ **Real Data**

Obviously this second approach demand the advanced presence of the forward model. Actually every inverse problem is built based on the corresponding forward model. It is noteworthy that in general inverse problems are much harder to solve. The difficulty arises because they are usually ill-posed. The term "ill-posed" indicates one or more of the following conditions:

- Noisy observed data.

- Insufficient data.

- Inconsistent data

- Inexact forward modeling

The cumulative effect of all these factors can leads to different issues regarding the existence, uniqueness and stability of a solution.

Existence:
Obviously, a solution must exist for the inverse problem to be worthy of investigation, and

$$\boldsymbol{M} \neq \varnothing \,, \tag{5.2}$$

is required.

Uniqueness:
Let's suppose that the same set of data $\mathbf{d}$ can be obtained from two different models, namely

$$\mathbf{m_0} \rightarrow \mathbf{d} = A(\mathbf{m_0}) \tag{5.3}$$
$$\mathbf{m_1} \rightarrow \mathbf{d} = A(\mathbf{m_1}) \,, \tag{5.4}$$

In this situation the data available are not sufficient to define a unique solution.

Stability:
This concept pertains to the continuity of the solution with respect to the data. Let's suppose $\mathbf{m_0}$ and $\mathbf{m_1}$ are respectively solutions of the two inverse problems

$$\mathbf{m_0} \rightarrow \mathbf{d_0} = A(\mathbf{m_0}) \tag{5.5}$$
$$\mathbf{m_1} \rightarrow \mathbf{d_1} = A(\mathbf{m_1}) \,, \tag{5.6}$$

Then, if there is no continuity with respect to the data, it could occur that when starting with two arbitrarily close sets of data, solution $\mathbf{m_0}$, $\mathbf{m_1}$ are completely

different. This is obviously an undesiderable situation especially because observed data are usually affected by some measurement error. The strategy to cope with these difficulties is to exploit the Tikhonov regularization theory (Tikhonov, 1977). This approach consists of searching the solution $\mathbf{m}$ in a subset $C \subset \boldsymbol{M}$ where the problem is well posed according to the following definition:

> **Definition 4** *The problem 5.1 is conditionally well-posed if the following conditions are met:*
>
> - *It is know a priori that the solution of 5.1 exists and belongs to a specific set $C \subset \boldsymbol{M}$.*
>
> - *The operator A is a one-to-one mapping of C onto AC and the operator A^{-1} is continuous on AC.*

Restricting the set $\boldsymbol{M}$ to C translates practically into adding some a priori information to the system. In particular in the least squared approach, first described by Gauss around 1794, the most probable set of parameters $\mathbf{m}$ is obtained by iterative minimization of the objective function E_M[1]

$$E_M = |A(\mathbf{m}) - \mathbf{d}|^2 \ . \tag{5.7}$$

It is standard to introduce some a priori information by adding a regularizer, i.e. a function $\mathcal{R}$ which modifies the original objective function. This leads to a new inverse problem to be minimized

$$E = |A(\mathbf{m}) - \mathbf{d}|^2 + \alpha \mathcal{R} \,, \tag{5.8}$$

where α is a weighting constant.

With this approach the original ill-posed problem is approximated by a family of well-posed problems depending on the value of α. The strategy consists of iteratively minimizing E until convergence occurs and then reducing the value of the weight. The procedure is then repeated until the desired overall decrease is reached.

Relevant to the inversion of surface data, the chosen approach tries to minimize the mismatch between the model generated surface displacement at receiver locations and the actual ones. This approach can be seen as a complete waveform inversion, accounting both for wave phase and amplitude. For simplicity the case of a layer over an half-space has been considered. The problem is highly ill-posed, creating

---

[1]Objective function is sometime called "Data fidelity term" as well as "Misfit function".

discretization of the interface requires a number of nodes much greater of the sensor's number. In order to regularize the objective function and obtain at the same time a smooth interface, a regularizer of the form

$$\mathcal{R} = \int_\Gamma ds \tag{5.9}$$

has been introduced. This is actually the integral of the arclength parameter. The competing effects of misfit and regularizer leads to the shortest interface satisfying the data.

In sec. 4.3 the frequency domain boundary element method was introduced as an effective way to model surface displacement. Here BEM was exploited as a forward model. What is obtained from the theoretical calculations are the surface displacements, expressed in frequency domain, at sensor's locations. In the following sections synthetic and some real data will be analyzed. Obviously the synthetic data, obtained from exploiting the forward model are in the correct form already. Real data on the other hand, needs a pre-elaboration.
Usually receiver response is expressed in terms of velocity or acceleration, so basically pre-elaboration consists of *offset removal* to remove the eventual DC component and *Fourier transform*; to express data in term of frequency. Finally to obtain displacements, integration by $\omega-$ arithmetic must be performed. The output of these elaborations is then suitable to be compared with theoretical displacements.

5.2   Synthetic Data Inversion.

5.2.1   Self consistency of the inversion algorithm

In order to test the consistency and robustness of the inversion algorithm, a trial model with a given geometry was implemented and the forward algorithm was exploited in order to obtain the synthetic displacements at the free surface.
The inversion algorithm was then expected to reconstruct the correct interface starting from an initial guess. The objective interface (fig. 5.2.1) was chosen with a 50 degree average slope in order to simulate a strong non-flat situation. A small hill was introduced to test the capacity to individuate details. The dimensions of the model are at engineering-geotechnical scale and receivers' locations were chosen analogous to arrays for classic surface wave investigations. The distance of the source to the closest receiver was 3 m (9.84 ft.) and distance between receivers was 4 m(13.12 ft.). Elastic parameters, source intensity and frequency were chosen as follows:

$f_0(\omega)[N]$	ω	$V_s[m/s]$	$V_p[m/s]$	$\rho[Kg/m^3]$
1000	1	400	500	1600
		4000	4500	2400

As a first test, synthetic data were obtain exploiting the forward model and then inverted. Fig. 5.2.1 shows that despite the drawbacks of using a numerical sensitivity matrix, the algorithm can individuate rough characteristics quite easily (10 to 30 iterations), however it requires more effort to individuate details. The stopping criterions were fixed respectively for the normalized misfit to be reduced to 10^{-2} and 10^{-3}, however the algorithm was let to cycle beyond these thresholds. Figure 5.2.1 shows an intermediate result (iteration 15), and results corresponding respectively to the misfit crossing the first and second thresholds (iteration 33 and 42). Finally iteration 100 is shown; no improvement was found passed this number of iterations in any of the test performed.

Since the forward algorithm produces displacements in frequency domain, the disturbance was introduced directly on the data calculated in this representation and designed to affect both the real and imaginary part. Effects of errors were investigated at different levels, in particular amplitude and phase were perturbed separately. (Fig. 5.2.1). It should be noted, as stated in section 5.1, that if real experimental data were recorded as velocities or accelerations, then they must be expressed in frequency domain. If they were originally affected by measurement errors, this affects the corresponding Fourier transform as well.

The way in which time domain errors are distributed on the Fourier transformed data strongly depends on the initial error distribution. The worst case scenario is when the distribution is uniform so the percentage of noise remains the same after transformation.

With Gaussian noise, the percentage of noise that passes to the Fourier transformed data is expected to be smaller. For this reason, error levels of 5% in Fourier transformed data can be considered a strong deviation. Inspecting figure 5.2.1 it is apparent how the final result is much more sensitive to noise which affects the phase relation between different receivers.

5.2.2 Two components VS. one components

In order to invert P-SV waves the algorithm exploits both the vertical and horizontal displacement to infer the shape of layer interface. In a second test with synthetic data, the possibility of exploiting only the vertical component of the displacements was investigated. There is a direct motivation to explore this possibility; in practical
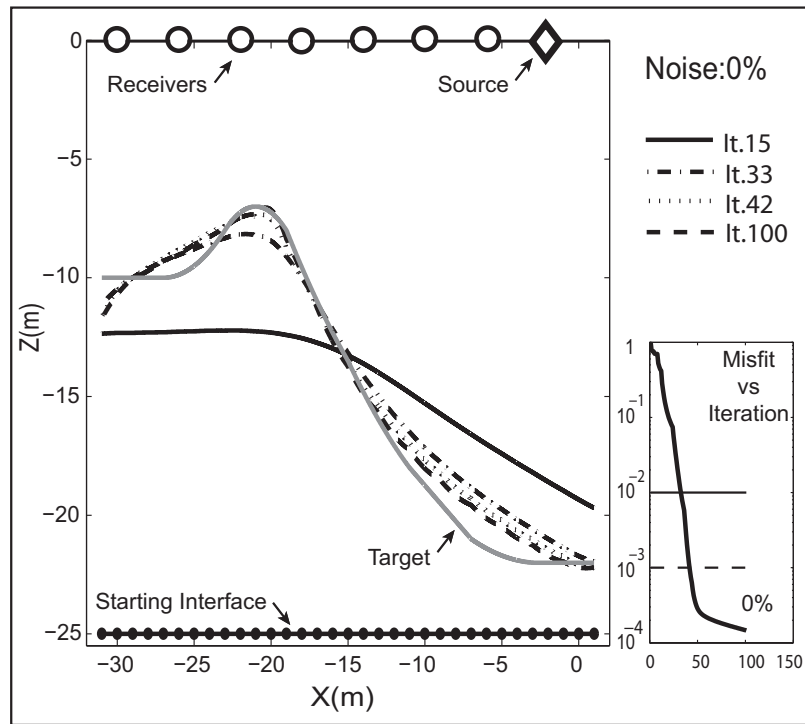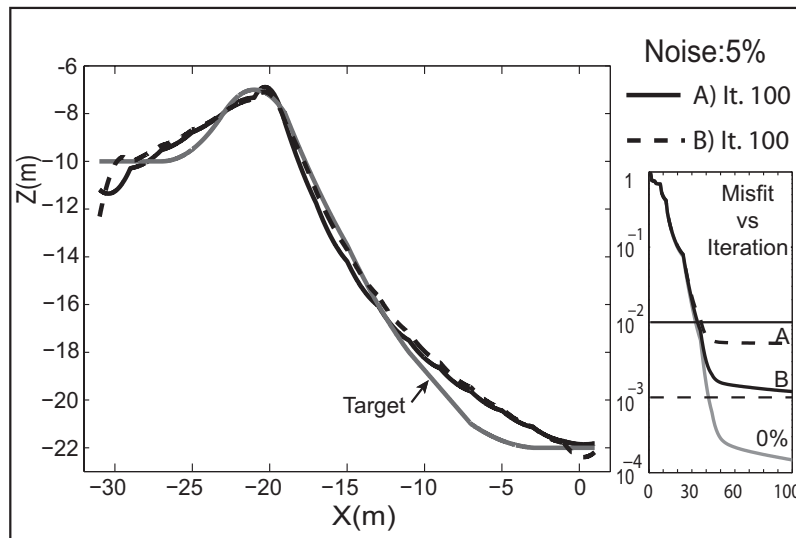
Figure 5.2: *Sensitivity respect to Gaussian noise; A) Error on phases, B) Error on Amplitudes*

surface wave testing, measuring equipment that can record displacements in more than one direction is much more expensive than its 1D counterpart (not only are 3D geophones necessary but also the seismograph must have double the number of recording channels). From a computational point of view, restricting the scope to one displacement component results in discarding half of the information available, worsening the already ill-posed problem.

Figure 5.2.1 shows the results of inversion using only the vertical component of displacements. As expected, the mathematical problem is more poorly conditioned and this results in an increased number of iterations.

The influence of noise is more severe, as expected, and small details are harder to individuate. Even if the inversion gives satisfactory results with one component only, care is needed during inversion because of an augmented tendency of the algorithm to lapse into local minima of the objective function.
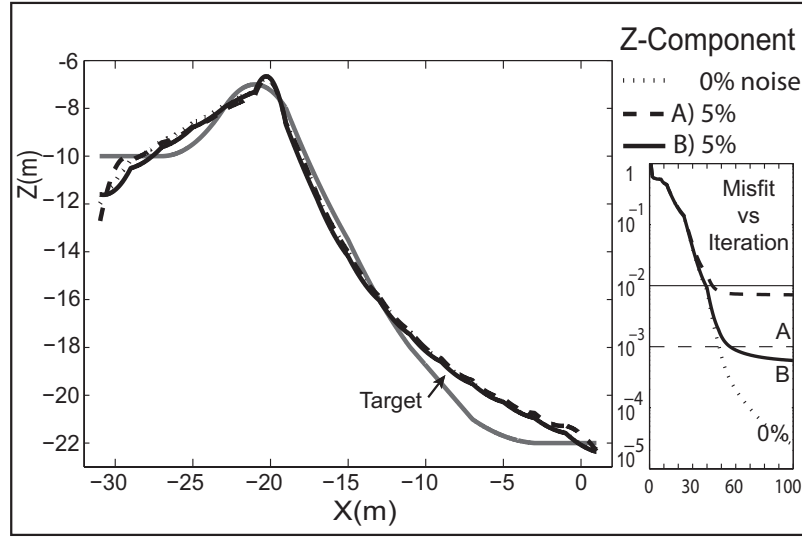
Figure 5.3: *One-component inversion A) Error on phases, B) Error on Amplitudes*

5.2.3   Non-flat surface

A common drawback of all surface waves testing is that the impossibility to handle non-flat interfaces is accompanied by the impossibility to perform surface investigations in the presence of non-flat surface. In the present development, since the only condition related to the surface introduced by modeling was the *free surface condition*; there is no restriction regarding the geometry. The application of the developed algorithm to a non-flat surface model is depicted in fig. 5.2.3. In the present simulation the more challenging case of 10% noise was investigated as well. Further the horizontal extent of the model was increased by four meters at each side allowing for an increased number of nodes.

5.2.4   Reduced Acoustic Impedance

As final test on synthetic data model for the geometry in fig. 5.2.1 was tested in a lower acoustic impedance jump case. Corresponding elastic parameters were chosen as follows:
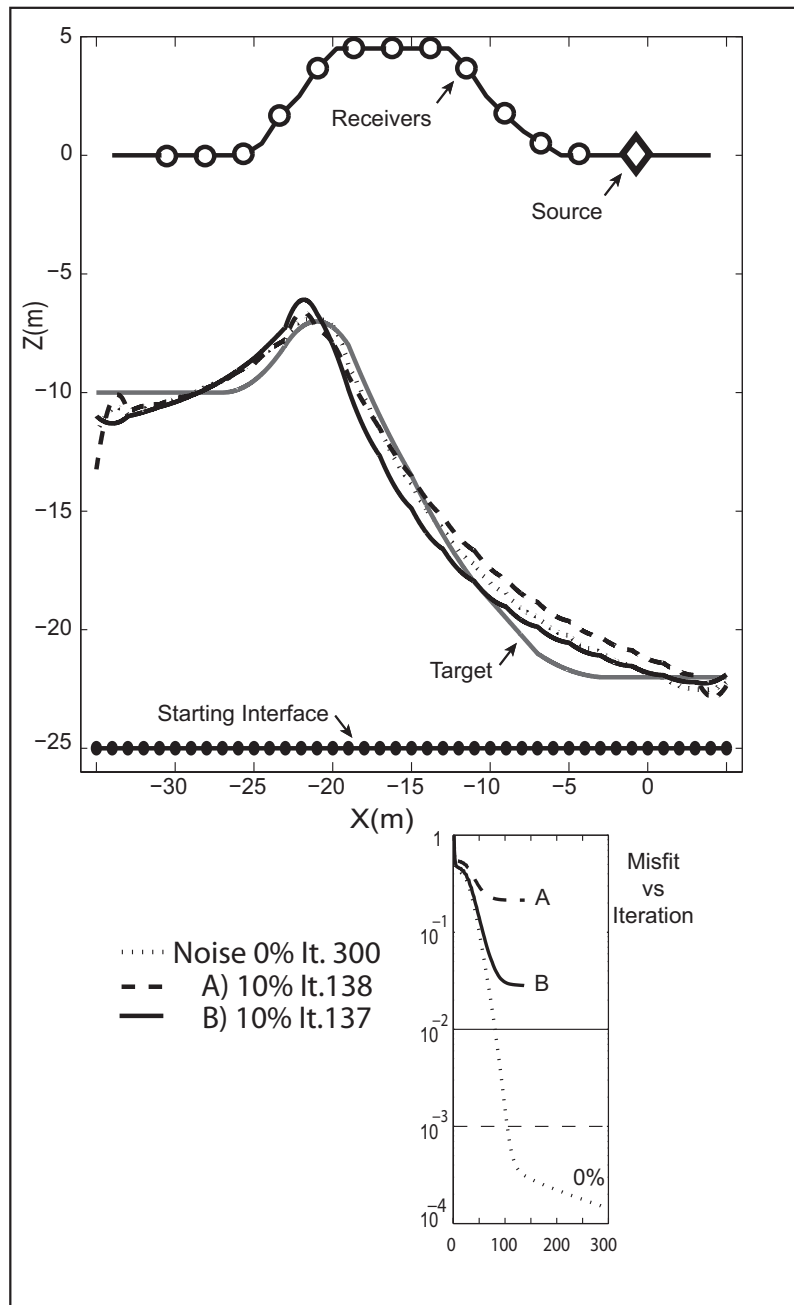
Figure 5.4: *Non-Flat surface model ; A) Error on phases, B) Error on amplitudes*

$f_0(\omega)[N]$	ω	$V_s[m/s]$	$V_p[m/s]$	$\rho[Kg/m^3]$
1000	1	400	500	1600
		800	900	2400
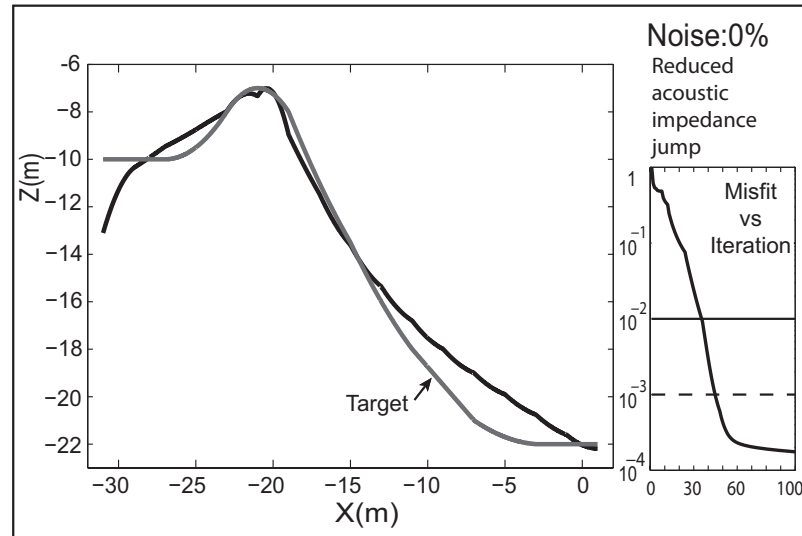
Figure 5.5: *Geometry of reference*

5.3   Real Data inversion

5.3.1   First study on real data

In last section synthetic data were inverted with different noise levels to assure algorithm stability. Since the final goal of processing is to extract information from data, a real dataset was investigated. It should be noted that due to the fact that the approach presented is completely new, it is very difficult to retrieve suitable datasets.

The main difficulty is that in classical surface wave testing the source is not recorded because there is no interest in the signal amplitude, while in this approach source amplitude is an important parameter.

The second point of difficulty is that all available surface waves' datasets are collected with the assumption of a parallel-layered soil and non-parallel cases are usually investigated with other methods. Therefore it is almost impossible to find surface wave data collected on a non-parallel layered soil and with a good knowledge of irregular buried structure. Only chance to match completely the requirements of the present method whould be to perform an ad-hoc field test.
Despite these difficulties some testing can still be performed.

Available information:
The exploited dataset, courtesy of Prof. Glenn J. Rix[2], was collected in a region of Alabama (USA). An *APS 400* electromechanical shaker accessorized with a reacting mass was operated as a harmonic source to provide signals ranging from about 3 to 100 Hz and vertical components of surface waves were monitored by a linear array of 15 receivers located at distances ranging from 2.4 to 32 m (8 to 105 ft) from the source.

Thanks to the testing performed by Prof. Rix, a shear wave velocity profile, obtained by the principles of surface wave propagation in a layered medium is available in table 5.1 and plotted in fig. 5.6.
The figure shows that some kind of major discontinuity in the shear wave is present. Indeed the local soil is actually known to be compatible with a layer+half-space model. Bedrock is known to lie between 61 to 70 meters deep, and after some investigation it turned out that bedrock is actually constituted of sandstone.

It is interesting to perform a comparison between the available data and characteristics of the inversion algorithm.

1. **Source:**
   The inversion algorithm assumes the source amplitude is known for the frequencies investigated.
   Real Data: the source amplitude is not known. Nonetheless an estimation of the force generated is still possible from data sheets of the source device and the formula

$$F_{Tot} = F_g + \frac{1}{2}(m_d + m_r)\omega^2\Delta_u , \qquad (5.10)$$

   where F_g is the maximum force magnitude generable by the shaker, m_d is the device mass m_r is the reacting mass and Δ_u is displacement induced at source location.

---

[2]Georgia Institute of Technology

Layer thickness	Shear Velocity
1	326
1	288
2	257
2	384
2	412
1	320
3	270
4	516
5	401
5	333
5	265
10	548
10	913
10	1196
10	1385

Table 5.1: Model obtained with surface wave beamforming method

2. **Recorded Data:**
   The inversion algorithm exploits two in-plane components, fortunately it was shown in sec. 5.2.2 that also performing inversion with only one component can lead to good results.
   Real Data: only the vertical component is available.

3. **Medias Characteristics:**
   At this stage of development the inversion algorithm assumes V_S, V_P and ρ to be known both for the layer and half space.
   Information available: the V_S profile is known, as well as depth and material of bedrock.

There is a serious lack of information.

Data Elaboration

As it is apparent, this lack of knowledge about the key parameters of the modelization seems to make any sort of application useless. Fortunately the main goal of this test is to reconstruct the *interface shape* between upper layer and bedrock which is known to be almost flat in the real soil. Approximating the real case with just the
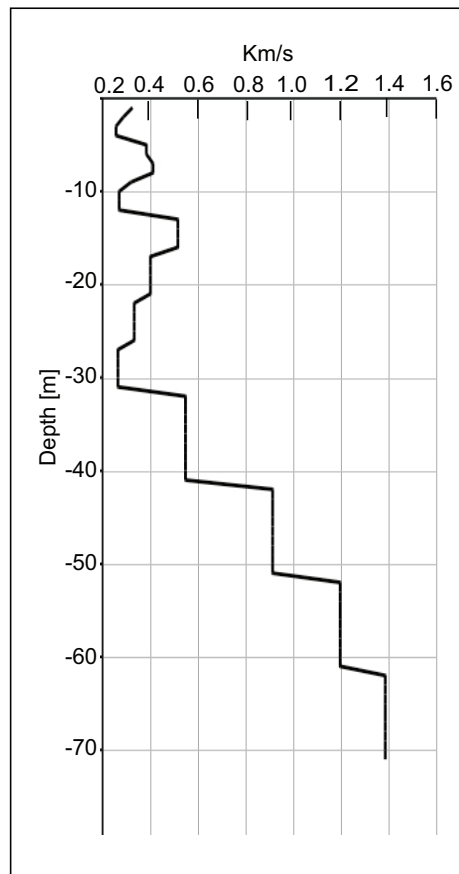
Figure 5.6: Local shear wave velocity profile obtained by classic surface wave methods

simplest model leads to the "equivalent" soil model where the interface may not be physical. Noneltheless, an error in V_S, V_P or ρ parameters is actually expected to affect only the depth of the interface and not its shape.

For this reason, the test will be considered successful if the inverted shape still remains flat.

In order to proceed, soil parameters must be chosen. Actually the parameters' influence was first investigated by means of the following procedure: shear wave velocity value of the layer and half space were chosen to be average velocityes according

to eq. 5.11

$$\bar{V}_s = \frac{\sum_{i=1}^{n_l} d_i}{\sum_{i=1}^{n_l} \frac{d_i}{V_{si}}} \; ; \tag{5.11}$$

once V_S was chosen, values of V_P and density ρ were selected according to the probable soil composition. Based on terrain characteristics in table 5.2, eight different

Nature of terrain	V_P (m/s)	V_S (m/s)	ρ (g/cm^3)
Top soil	300 - 700	100 - 300	1.7 - 2.4
Dry sand	400 - 1200	100 - 500	1.5 - 1.7
Wet sand	1500 - 2000	400 - 600	1.9 - 2.1
Saturated clays	1100 - 2500	200 - 800	12.0 - 2.4
Coal	2200 - 2700	1000 - 1400	1.3 - 1.8
Saturated sandy clay formations	1500 - 2200	500 - 750	2.1 - 2.4
Porous and saturated Sandstone	2000 - 3500	800 - 1800	2.1 - 2.4

Table 5.2: Model obtained with surface wave beamforming method

sets of parameters were selected and are detailed in table 5.3. The following criterion were adopted: for the first group, namely setups 1 to 4; the V_{S30} and an estimation of V_S in the half-space were calculated by means of eq. 5.11 and values of table 5.1. Then, keeping fixed values for V_S, density ρ and shear modulus μ have been calulate in order to obtain combinations with the lowest shear modulus (and lowest density) and combinations with highest shear modulus (and highest density) in reasonable accordance with the values on table 5.2, namely top-soil, dry sand and saturated clays for which $V_{S_{30}}$ is consistent.
As final step for each $\rho - \mu$ combination,λ has been tuned in order to obtain its maximum and minimum values. Combinations then represent the cases in table 5.3 and summarized as follows:

Setup 1: fixed V_s profile $\rightarrow$ Minimum ρ, μ and λ

Setup 2: fixed V_s profile $\rightarrow$ Maximum ρ, μ and minimum λ

Setup 3: fixed V_s profile $\rightarrow$ Minimum ρ, μ and maximum λ

Setup 4: fixed V_s profile $\rightarrow$ Maximum ρ, μ and maximum λ

Setup	Domain	$V_S(m/s)$	$V_P(m/s)$	$\rho(Kg/m^3)$
1	L.	355	615	1500
	H.S.	1014	2002	2100
2	L.	355	615	2400
	H.S.	1017	2002	2400
3	L.	355	1200	1500
	H.S.	1014	3500	2100
4	L.	355	1200	2400
	H.S.	1017	3500	2400
5	L.	604	1044	1500
	H.S.	1504	2604	2100
6	L.	604	1046	2400
	H.S.	1504	2605	2400
7	L.	604	1200	1500
	H.S.	1504	3500	2100
8	L.	604	1200	2400
	H.S.	1504	3500	2400

Table 5.3: Tested Setups

The same holds true for setups from 5 to 8, the only difference being that V_{s60} was taken as a reference. It should be noted that the exploited inverse algorithm implements a minimim interface length regularizer. The main effect of this choice is that when the guessed starting model presents an interface which is far from the minimum objective energy configuration, the data fidelity term causes the interface to move, but the regularizer keep it flat. As a consequence, the task accomplished by the algorithm during initial iterations is to find the parallel layer configuration closest to the actual soil. On one hand forcing the interface to be flat could be an interesting alternative method to perform classical inversions, this allows a prediction of the most probable depth of the flat interface. This last characteristic of the algorithm has been exploited to perform a parametric study. The misfit term has been calculated by placing a flat surface at many different locations. Figures 5.7(a) and 5.3.1 depict the calculated misfit term as a function of the depth. This show that at least for parallel layered models the misfit presents a unique minimum.

The available data consted of 71 files, corresponding to 71 different values of frequency. Since the sensors adopted were accelerometers, the elaboration required both a Fourier transformation and a double integration, performed in frequency domain by the $\omega -$ arithmetic. This method of integration requires the discarding of small frequencies, so further elaborations involved only frequencies larger than 1 Hz. After parameter investigation, the following two sets have been selected for inversion

Inversion parameters 1:

	V_P	V_S	ρ	λ	μ
Layer	664	355	1500	$2.83e^8$	$1.89e^8$
Half-space	2001	1369	2400	$6.126e^8$	$4.5e^9$

Inversion parameters 2:

	V_P	V_S	ρ	λ	μ
Layer	959	605	1500	$2.83e^8$	$5.48e^8$
Half-space	2180	1500	2400	$6.126e^8$	$5.4e^9$

and the inverted interface are respectively depicted in figure 5.3.1 and 5.3.1
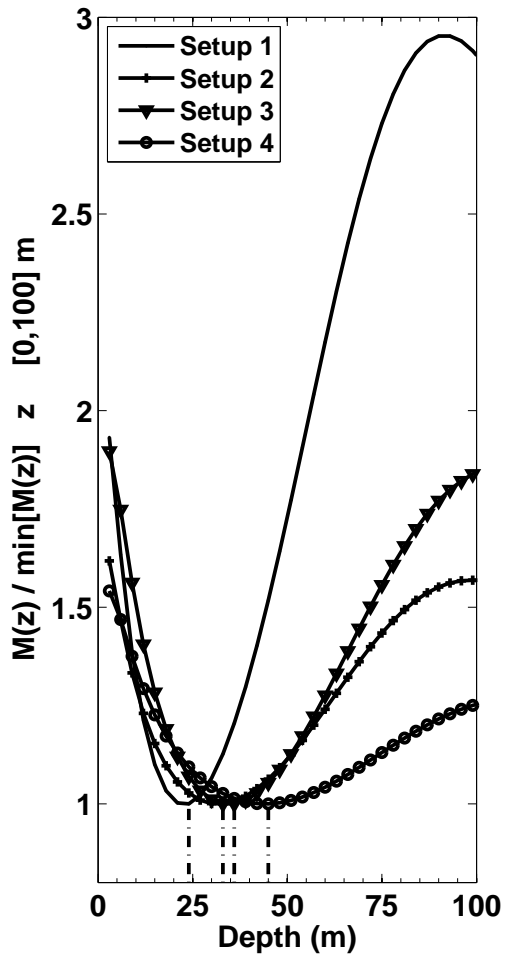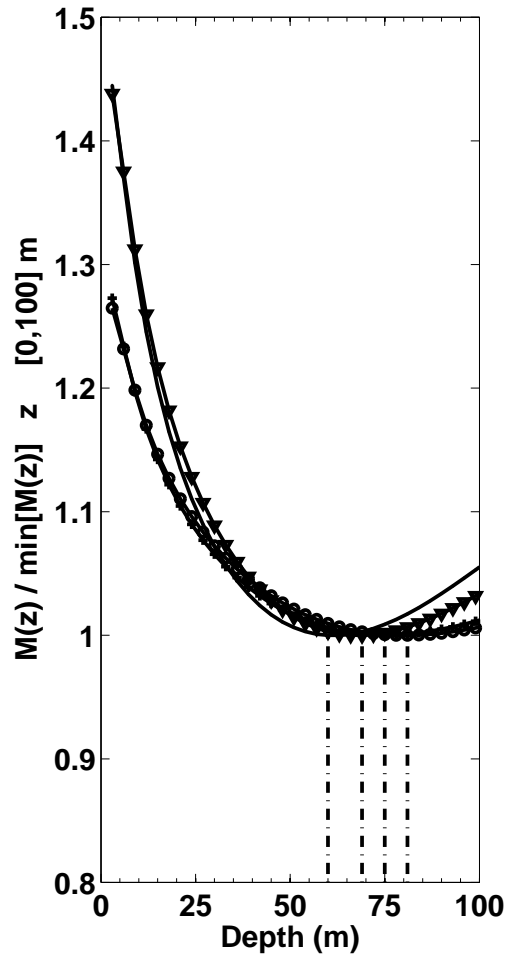
(a) Setups 1 to 4   (b) Setups 5 to 8

Figure 5.7:
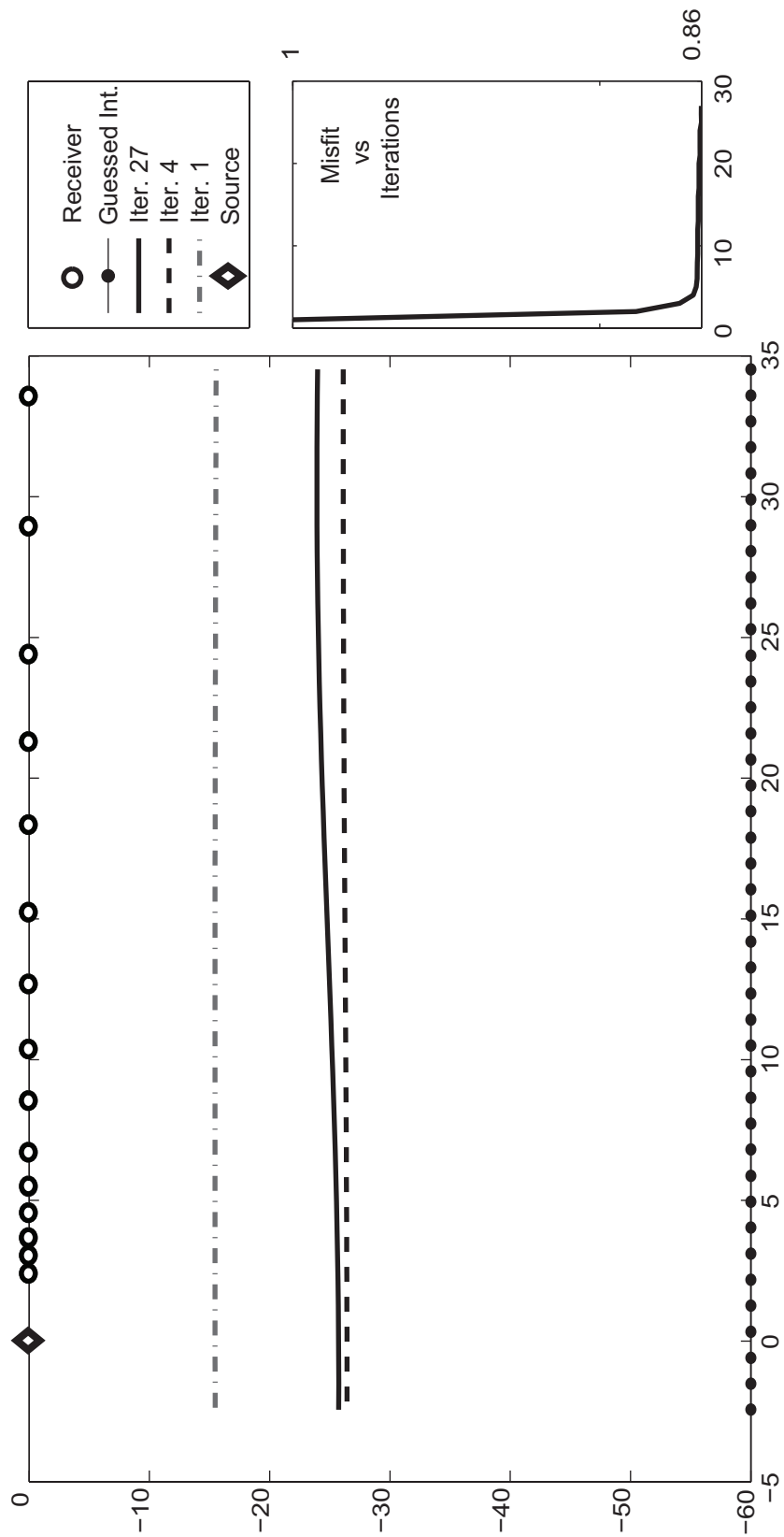
Figure 5.8: Setup 1 Inversion
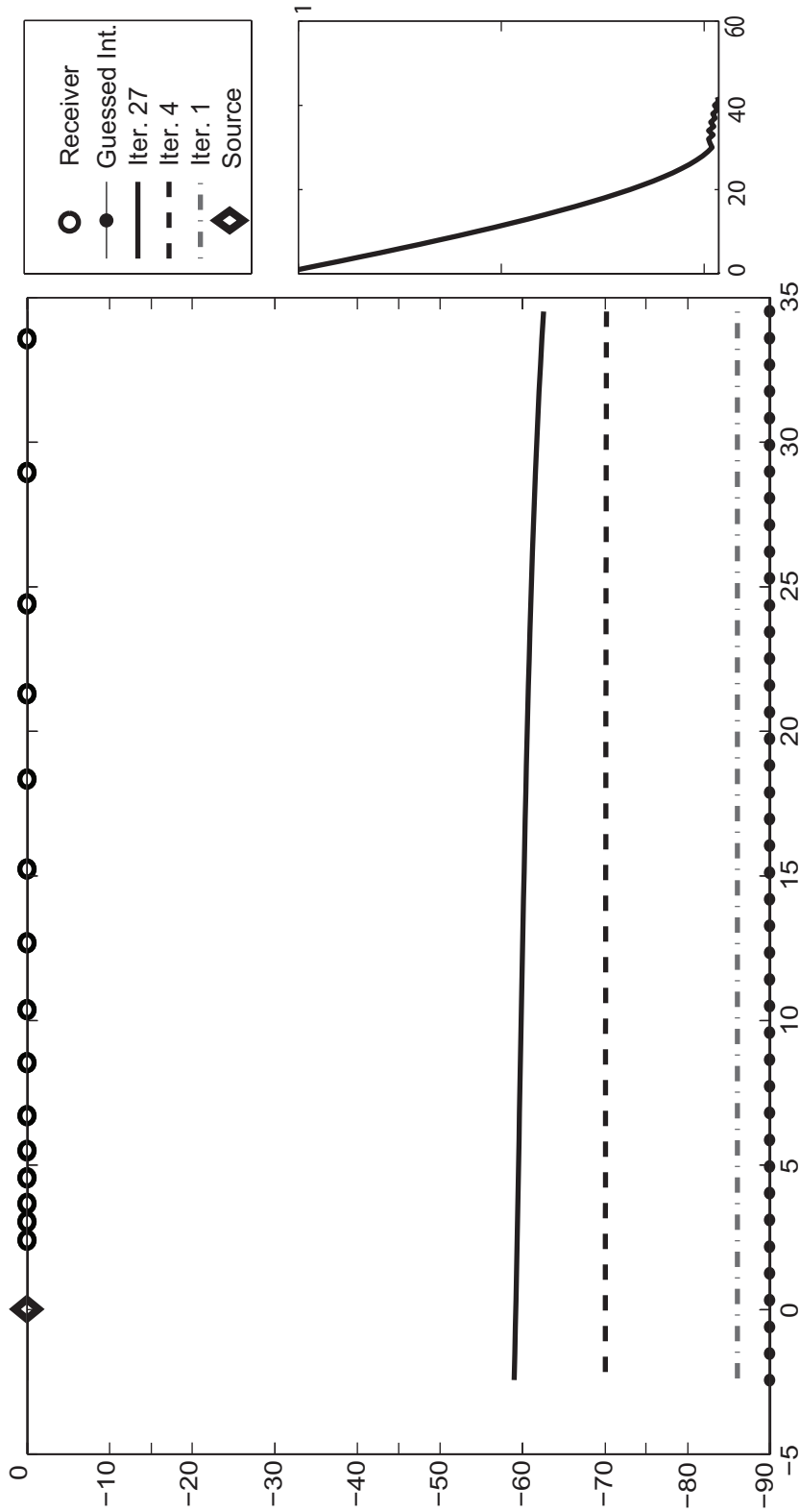
Figure 5.9: Setup 2 Inversion

Chapter 6

Analytical Shape Derivative.

In chapter 5.1 a complete waveform inversion feasibility study was investigated. The numerical calculation of a shape sensitivity matrix, which related change of calculated displacements at sensor locations with a perturbation of the subsoil structure was demonstrated to be effective despite its low numerical accuracy. However for discretization with a large number of nodes the computational time grows as the square of the number of nodes. Moreover as the number of nodes exceeds the number of available data measurements, the problem becomes ill-posed and the numerical inversion inefficient. To overcome such limitations and improve the speed and reliability of optimization, an alternative approach is necessary.

Unfortunately, shape optimization in the field of elastodynamics is a pretty recent development and there is little literature on inverse model approaches related to this topic. Some recent work attempted to introduce concepts of imaging (Guzina 2004, 2006). Attempts have been made calculating the first derivative of Graffi's boundary integral equation or extending the topological derivative concept introduced by Novotny *et al.* (2003) to elastodynamic (Carretero, 2008; Bertsch, 2010).

In this chapter a novel analytic formulation for node displacements is introduced. The formulation is valid for general surface topologies infinite non-parallel layers. The presented approach exploits the geometric Calculus of Variations for curves and surfaces.

6.1   Tools of the Calculus of Variations

The Calculus of Variations is a field of mathematics that deals with the maximization or minimization of functionals .

Functionals are mappings from a set of functions to real numbers. A functional is sometime referred to as an *energy* $\mathcal{E}$ and is usually posed in integral form. The integrand, referred to as the *Lagrangian* is usually expressed by a suitable combination of a function f and its derivative.

$$E(f) = \int_0^1 L(f, f', x)dx \,, \tag{6.1}$$

where $f' = \frac{df}{dx}$.

The extreme effectiveness of the Calculus of Variations has been exploited in many fields of mathematics and physics. The framework operates within the infinite dimensional space of functions. Functional minimization consists of moving through this space by following the trajectory which minimizes the energy.

As a first step, a function must be generalized to the infinite dimensional space. Conceptually f can be sampled for many values of the parameter x and a vector of length n can be defined as

$$\boldsymbol{V} = (f(x_0), \ f(x_1), \ \dots \ f(x_{n-1}), \ f(x_n)) \,, \tag{6.2}$$

this simple operation leads to an $n -$ dimensional representation of the function. In this space a norm could be defined as

$$|f|^2 = \sum_{i=0}^{n} f^2(x_i) \,, \tag{6.3}$$

unfortunately this definition is not intrinsic to the function. In fact if a half-spaced sampling is considered, the new norm is equal to the old one plus a contribution from the new points

$$|f|^2 = \sum_{i=0}^{n} f^2(x_i) + \sum_{\text{New points}} f^2(x_i) \,. \tag{6.4}$$

Thus the norm is found to depend on the number of samples. A well defined norm is then expressed by

$$|f|^2 = \frac{1}{n} \sum_{i=0}^{n} f^2(x_i) \,. \tag{6.5}$$

As $n \to \infty$, the space step Δx goes to zero and the new definition of norm is written as

$$\lim_{n \to \infty} \Delta x \sum_{i=0}^{n} f^2(i\,\Delta x) \to \int_0^1 f^2(x)dx \doteq \|f\|_{L_2(0,1)} \,, \tag{6.6}$$

where the integral is in the Riemann sense and $L_2(0,1)$ is the space of squared integrable functions with parameter[1] on $[0, 1]$. The procedure outlined transforms the finite vector space of samples of the function f into a related infinite dimensional vector space.

It is worthwhile to investigate which concepts of finite dimensional concepts carry over to infinite dimensional vector spaces. First of all, the norm has a different meaning, taking the three-dimensional space as an example, two vectors $\boldsymbol{V} = (V_1, V_2, V_3)$ and $\boldsymbol{W} = (W_1, W_2, W_3)$ are equal if and only if

$$
\begin{aligned}
V_1 &= W_1 \\
V_2 &= W_2 \\
V_3 &= W_3 .
\end{aligned}
$$

Indeed

$$\boldsymbol{V} - \boldsymbol{W} = 0, \tag{6.7}$$

is sufficient to state that V, W are the same.

The concepts of norm, distance and internal product are defined by

$$
\begin{aligned}
\|\boldsymbol{V}\|^2 &= V_1^2 + V_2^2 + V_3^2 \\
\|\boldsymbol{V} - \boldsymbol{W}\| &= (V_1 - W_1)^2 + (V_2 - W_2)^2 + (V_3 - W_3)^2 \\
\boldsymbol{V} \cdot \boldsymbol{W} &= V_1 W_1 + V_2 W_2 + V_2 W_2 .
\end{aligned}
\tag{6.8}
$$

It is straightforward to see that operations in 6.8 involve each coordinate and holds for any finite number of dimensions.

The infinite dimensional counterpart is instead slightly different. Two vectors in $L_2(0,1)$ are the same if and only if

$$\|f - g\|_{L_2(0,1)} = 0. \tag{6.9}$$

Since Riemann integration is involved in 6.6 this means that f and g are allowed to be different at some points, since isolated pointwise differences in the functions do not contribute the L_2 norm of their difference. It is evident that to extend the concept of equality, it is necessary to relax 6.7 to 6.9 form, which is not valid for all "coordinates" of the vector involved; in a sense, it is not point-wise true. The meaning of distance instead follows with the same meaning. The form of the infinite

---

[1]Here any other domain for parameter can easily be reduced to the assumed one

version resembles the form of the finite version where integration is used instead of summation

$$\|f - g\| = \int_0^1 (f(x_1) - g(x_1))^2 \, dx \, .$$

The main concepts of infinite dimensional calculus such as the norm and inner product are then respectively defined as

$$\int_0^1 f^2(x) dx \quad \doteq \quad \langle f, f \rangle \tag{6.10}$$

$$\int_0^1 f(x) \, g(x) dx \quad \doteq \quad \langle f, g \rangle \, . \tag{6.11}$$

$$\tag{6.12}$$

The main advantage of generalizing a finite dimensional function to an infinite dimensional space is that an elegant formulation of the optimization problems exists.

In one-dimensional problems the necessary condition for a point to be stationary is the null derivative. In higher, finite dimensions this coincides with the null gradient requirement.

In infinite dimensions a necessary condition exists as well and corresponds to request that the variation of the functional $E(f)$, with respect to any infinitesimal perturbation of f is zero. Since the functional is expressed by f, a perturbation consists of slightly changing the function. As it happens in every space, perturbing one element of the space leads to another element of the same space; this can be pictured as moving along a trajectory connecting different points of the space, every point being a function. By superposition, perturbation of a point by ϵ corresponds to move from point f to the point $f + \epsilon g$, and this can be interpreted as a movement along an ϵ-dependent trajectory

$$f \to f + \epsilon g \, . \tag{6.13}$$

Assuming that $\mathcal{E}$ can be regarded as function of ϵ then the *variation* is defined as the directional derivative of $\mathcal{E}$ along ϵ direction

$$\frac{\partial \mathcal{E}}{\partial \epsilon} = \lim_{\epsilon \to 0} \frac{\mathcal{E}(f + \epsilon g) - \mathcal{E}(f)}{\epsilon} \, . \tag{6.14}$$

If the directional derivative is zero independently of the perturbation direction g, the desired necessary condition has been found, in particular

$$\left. \frac{\partial \mathcal{E}(f + \epsilon g)}{\partial \epsilon} \right|_{\epsilon=0} = \frac{\partial}{\partial \epsilon} \int_0^1 L(f + \epsilon g, f' + \epsilon g', x) dx \, . \tag{6.15}$$

Introducing $h = f + \epsilon g$,

$$\frac{\partial \mathcal{E}(h)}{\partial \epsilon}\Big|_{\epsilon=0} = \int_0^1 \frac{dL}{dh}g + \frac{dL}{dh'}g' \, dx \,, \tag{6.16}$$

separating integrals and integrating the second by parts

$$\frac{\partial \mathcal{E}(h)}{\partial \epsilon}\Big|_{\epsilon=0} = \int_0^1 \frac{dL}{dh}g \, dx - \int_0^1 \frac{d}{dx}\left(\frac{dL}{dh'}\right)g \, dx + \frac{dL}{dh'}g\Big|_0^1 \,. \tag{6.17}$$

If the case of fixed known end-points is considered such that the boundary term vanishes, the remaining pieces can be collected to form

$$\frac{\partial \mathcal{E}(h)}{\partial \epsilon}\Big|_{\epsilon=0} = \int_0^1 \left(\frac{dL}{dh} - \frac{d}{dx}\left(\frac{dL}{dh'}\right)\right)g \, dx \,. \tag{6.18}$$

The only way for eq. 6.18 to be zero independently of the value of g is for the term in parenthesis to equal zero. Finally

$$\frac{dL}{df} - \frac{d}{dx}\left(\frac{dL}{df'}\right) = 0 \,. \tag{6.19}$$

The result obtained is that this Euler-Lagrange Equation 6.19 represents a necessary condition to obtain a local maximum or minimum. To proceed further the formal definition of gradient must be considered

Definition 5 *Gradient*
The Gradient *of a scalar function $f(x, y, z, \dots)$ denoted as ∇f, where ∇ denotes the vector differential operator, is defined as the vector that satisfies the relation*

$$\langle \nabla \mathcal{E}, \boldsymbol{V} \rangle = \frac{\partial \mathcal{E}}{\partial \boldsymbol{V}} \tag{6.20}$$

It is worth noting that the definition of internal product 6.11, eq. 6.18 actually possesses the structure

$$\int_0^1 \left(\frac{dL}{df} - \frac{d}{dx}\frac{dL}{df'}\right)g \, dx \equiv \langle \nabla \mathcal{E}, g \rangle \,, \tag{6.21}$$

it can be proven that the Euler-Lagrange equation is the infinite dimensional counterpart of the finite dimensional gradient.

A classic example of the effectiveness of the Euler-Lagrange eq. isfound in curve length minimization.

Example 1 *Starting from the energy 6.22, which is the arclength of the curve $\boldsymbol{C} = (x, f(x))$*

$$\mathcal{E} = \int_0^1 \sqrt{1 + (f')^2}\, ds\,, \tag{6.22}$$

then the corresponding Euler-Lagrange equation is

$$-\frac{\partial L_{f'}}{\partial x} = 0$$

$$\frac{f''}{\left(1 + f'^2\right)^{3/2}} = 0\,,$$

which simplifies to $f'' = 0$; exactly the equation of a straight line.

Following what has been stated so far, the procedure to infinitely sample the function f and consider the obtained vector $\boldsymbol{V}$ as belonging to the $L_2(0,1)$ space, leads to a scheme where Calculus of Variations applies and Euler-Lagrange equations can be interpreted as the gradient in this infinite dimensional space.

The machinery for functional minimization can be exploited, after some modifications for optimization of geometric shapes. The classic procedure is to build a suitable curve/shape-dependent Energy functional, to calculate the Euler-Lagrange equation and then to introduce an artificial time dependence to allow the curve to evolve. In particular if

$$\boldsymbol{C} = \begin{pmatrix} x \\ y \end{pmatrix}\,, \tag{6.23}$$

then

$$\boldsymbol{C}(t + \Delta t) = \begin{pmatrix} x(t) \\ y(t) \end{pmatrix} - \Delta t\, \nabla\mathcal{E}\,; \tag{6.24}$$

the following example shows the procedure for the energy 6.22 of ex. 1.

Example 2 *In ex. 1 the form of Euler-Lagrange equation was obtained. If time dependence is introduced, the evolution equation, also called* minimization flow, *assumes the form*

$$f_t = -\nabla\mathcal{E} = \frac{f''}{\left(1 + f'^2\right)^{3/2}}\,, \tag{6.25}$$

and

$$f(t + \Delta t) = f(t) - \Delta t\, \nabla \mathcal{E} = f(t) + \Delta t\, \frac{f''}{\left(1 + f'^2\right)^{3/2}}\,. \qquad (6.26)$$

6.2   Basics of curves

In the former section the basics of variational calculus were introduced.

The motivation is to apply the machinery of Calculus of Variations to geometric objects. Here the topic is focused on curves, but most of these arguments still hold for surfaces. Unfortunately there exists a big difference between a function and a curve. In fact the domain of a function doesn't change and the integral of an energy function on a fixed domain Ω (2D case for simplicity), is

$$\mathcal{E}(f) = \iint_\Omega L(f,\, f_x,\, f_y,\, x,\, y)\, dx\, dy\,. \qquad (6.27)$$

In the machinery of infinite dimensional calculus all of the candidate functions are defined on the same domain, this assumption permits elimination of boundary terms from integration by parts, leading to Euler-Lagrange equations and subsequently to the gradient descent.

The main difficulty with curves is that there is usually a parametrization involved. For a curve length L parametrized by the arclength, for example on the interval $[0,\, 1]$, every value of the parameter identifies a point on the curve. If the curve evolves, the parametrization and consequently the length changes. Let's introduce some basic concepts of curves:

Definition 6 *The curve (planar) is the image of a continuous mapping*

$$y : [0, 1] \to \mathbb{R}^2\,, \qquad (6.28)$$

where $[0, 1]$ is called "parameter space".

Definition 7 *A "Parametrized curve" is a continuous mapping*

$$\boldsymbol{C}(p) = \begin{pmatrix} x(p) \\ y(p) \end{pmatrix}\,, \qquad (6.29)$$

from a unit interval to $\mathbb{R}^2$.

The curve is the geometric object and does not depend on the parametrization. The parametrized curve is the mapping, and there are many ways to parametrize the curve.

6.2.1   Geometric properties of curves.

> **Definition 8** *Every quantity that can be calculated and that does not depend on a curve's parameterization is defined as* "Geometric".

As a first step, derivatives must be ensured independent on the parametrization; to fulfill this requirement, some constraints on the curve itself have to be made. For functions, differentiability is a well defined concept. For curves, arbitrarily choosing a differentiable representation is not sufficient because the goal is to obtain derivatives of the object itself and not just of the representation. In this scope, regular curves must be considered.

> **Definition 9** *A curve is called* Regular *when given a parametric representation* $\boldsymbol{C}(p)$*, its derivative* $\partial\boldsymbol{C}(p)/\partial p$ *never vanishes for any* p *in the domain of the parameter* $[a,b]$*.*

It is then not sufficient to have a differentiable mapping, the derivative must never vanish; in fact points where the derivative is zero correspond to cusps of the curve; the condition of *regularity* is set up to avoid this kind of situation, where even if the related parametrization formula is differentiable, the curve is not.

- ***Speed of a parametrized curve***

$$\mid \boldsymbol{C}_p \mid = \sqrt{x_p^2 + y_p^2}, \tag{6.30}$$

  where the subscript indicates derivative, is the norm of the derivative with respect to the parameter.

- ***Velocity of a parametrized curve***

$$\boldsymbol{C}_p = \begin{pmatrix} x_p \\ y_p \end{pmatrix}. \tag{6.31}$$

- ***Unit tangent vector***

$$\boldsymbol{T} = \frac{\boldsymbol{C}_p}{\mid \boldsymbol{C}_p \mid}. \tag{6.32}$$

The unit tangent vector is a *Geometric Property*, the only non-geometric part being its sign, which indicates whether the curve is parameterized to be traced backward or forward depending on p.

It is worth noting that at the cusps there is no way to define a unique value for the unit tangent. This leads to the consideration of the unit tangent as the geometric counterpart for curves of the first derivative for functions. In this sense, condition $\partial \boldsymbol{C}(p)/\partial p \neq 0$ turns to be a regularity condition for curves.

- **Unit normal vector**

$$\boldsymbol{N} = J\boldsymbol{T} = J\frac{\boldsymbol{C}_p}{|\boldsymbol{C}_p|} = \begin{pmatrix} 0 & 1 \\ -1 & 0 \end{pmatrix}\frac{\boldsymbol{C}_p}{|\boldsymbol{C}_p|}. \tag{6.33}$$

The Unit normal is still a geometric property of the curve.

Definition 10 Reparametrization
Reparametrization of a curve $\phi : [0,1] \to [0,1]$ is a "diffeomorphism" such that $\phi(0) = 0$, $\phi(1) = 1$

The interval is mapped on the same interval, and the derivative is strictly greater than zero[2], $\phi_p > 0$ for all $p \in (0,1)$.

Diffeomorphism
Is called a differentiable function with a differentiable inverse. Given a parametrization $\boldsymbol{C}(p)$ of a curve and a diffeomorfism $\phi(p)$, then $\boldsymbol{C}(\phi(p))$ is a reparametrization of $\boldsymbol{C}(p)$.

- **The Arclength parameter**
  Is a parametrization that ranges from zero to the length of the curve and has the following interpretation: assuming the curve starts from 0, and is traced to s, then the length of the curve between the two points is s. This obviously is another geometric property and the arclength is independent of any other parametrization.

- **Curvature**
  This is the inverse of the radius of the "osculating circle"; the osculating circle being the circle that locally best approximates the curve at point p.

---

[2]Technically the only necessary feature is $\phi_p \neq 0$. Cause of the $\phi_p > 0$ property, this is called a "Positive Reparametrization" and the $>$ preserve the direction of the point identified by p along the curve. A "Negative Reparametrization" ($\phi_p < 0$)traces the curve backward.

A clearer interpretation for k can readily be obtained investigating its mathematical expression

$$k = \frac{1}{r} = \frac{\boldsymbol{C}_{pp} \cdot J\, \boldsymbol{C}_p}{\mid \boldsymbol{C}_p \mid^3} \,, \tag{6.34}$$

where J represents a $\pi/2$ rotation.

The term, $\boldsymbol{C}_{pp}$ is the acceleration of the trajectory $\boldsymbol{C}(p) = (x(p),\, y(p))^T$; being a vector it has two components and can be decomposed along the tangent and the normal to the curve

$$\boldsymbol{C}_{pp} = (\boldsymbol{C}_{pp} \cdot \boldsymbol{T})\, \boldsymbol{T} \,+\, (\boldsymbol{C}_{pp} \cdot \boldsymbol{N})\, \boldsymbol{N} \,. \tag{6.35}$$

The tangent term changes in speed along the curve, it depends only on the parametrization and is not geometric. Indeed, translating points of an infinitesimal distance along the tangent does not change the curve; on the other hand, the normal part term which really carries a geometric meaning is the term responsible for a change of the curve. Note that if the second derivative with respect to arclength is considered, then the expression [3]

$$
\begin{aligned}
\boldsymbol{C}_{ss} &= \frac{\frac{\boldsymbol{C}_{pp}}{|\boldsymbol{C}_p|} - \frac{\boldsymbol{C}_p}{|\boldsymbol{C}_p|^2}\frac{\boldsymbol{C}_p \boldsymbol{C}_{pp}}{|\boldsymbol{C}_p|}}{\mid \boldsymbol{C}_p \mid} = \frac{\boldsymbol{C}_{pp} - (\boldsymbol{C}_{pp} \cdot \boldsymbol{T})\, \boldsymbol{T}}{\mid \boldsymbol{C}_p \mid^2} \\
&= \frac{(\boldsymbol{C}_{pp} \cdot \boldsymbol{N})}{\mid \boldsymbol{C}_p \mid^2}\boldsymbol{N} \\
&= \frac{(\boldsymbol{C}_{pp} \cdot J\, \boldsymbol{C}_p)}{\mid \boldsymbol{C}_p \mid^3}\boldsymbol{N} \\
&= k\, \boldsymbol{N} \,,
\end{aligned}
$$

is called the *geometric second derivative*, and shows that curvature is the geometric version of a second derivative for functions.

6.2.2   Calculus of Variations for curves.

To introduce features of Calculus of Variation for curves, let's first consider a very simple energy 6.36, which measures how unsmooth the curve is, the parameter is assumed to run from zero to one .

Example 3 *The scheme for function based minimization, namely*

Energy $\rightarrow$ Lagrangian $\rightarrow$ gradient descent

---

[3]The use of the planar rotation J makes this relation valid in 2D environments only.

does not work because of the intermediate passage of parametrization, nevertheless heedlessly applying this old fashion calculus leads to

$$\mathcal{E} = \frac{1}{2} \int_0^1 | \boldsymbol{C}_p |^2 \, dp = \int_0^1 \boldsymbol{C}_p \cdot \boldsymbol{C}_p dp \qquad (6.36)$$

$$
\begin{aligned}
x_t &= -\frac{1}{2}\left(L_x - \frac{d}{dp}L_{x_p}\right) = \frac{d}{dp}(x_p) = x_{pp} \\
y_t &= -\frac{1}{2}\left(L_y - \frac{d}{dp}L_{y_p}\right) = \frac{d}{dp}(y_p) = y_{pp} \, ,
\end{aligned}
$$

finally

$$
\begin{aligned}
\begin{pmatrix} x_t \\ y_t \end{pmatrix} &= \begin{pmatrix} x_{pp} \\ y_{pp} \end{pmatrix} \\
\boldsymbol{C}_t &= \boldsymbol{C}_{pp} \, .
\end{aligned}
\qquad (6.37)
$$

Note that this last expression [4] is parametrization-dependent, which means that evolutions started with different parametrizations (differing in speed) give completely different results. It is clear that parametrization is an arbitrary choice and is supposed to be a tool to describe the geometric object without affecting it. The problem lies in the fact that from the beginning the Energy (eq. 6.36) was not geometric.

In order to obtain a variational scheme capable to bypass the parametrization problem, it is necessary to change the approach: let's consider the energy depending upon the curve; recalling the definition of $L_2(0,1)$ product, eq 6.11, and relation

$$E_v = \langle \nabla \mathcal{E}, \mathbf{v} \rangle \, , \qquad (6.38)$$

here function f and perturbation g are replaced by curve representations.

If energy depends on a curve, calculating the variation of the energy with respect to a variation of that curve means calculating the directional derivative of the energy with respect to the direction connecting the original and the perturbed curve. Exploiting the $L_2(0,1)$ product definition

$$\frac{dE}{dt} = \frac{d\mathcal{E}}{d\boldsymbol{C}_t} \cdot \boldsymbol{C}_t \, . \qquad (6.39)$$

---

[4]Eq. 6.37 is commonly known as *heat equation* cause of the similarity with the equation for heat propagation in physics. It is exploited in image processing to smooth images.

translates into

$$\frac{dE}{dt} \;=\; \langle \nabla \mathcal{E}, \, \boldsymbol{C}_t \rangle = \int_0^1 \boldsymbol{C}_t \cdot \nabla \mathcal{E} \, dp \,. \tag{6.40}$$

The meaning of eq. 6.40 is quite subtle. Imagine that the curve is a function of time, then a time-dependent energy can be written. The derivative of energy with respect to time must be calculated and manipulated until the term $\boldsymbol{C}_t$ is isolated and finally, the expression multiplying $\boldsymbol{C}_t$ corresponds to the directional derivative $\nabla \mathcal{E}$. The final step is once again the equation

$$\boldsymbol{C}_t \;=\; -\nabla \mathcal{E}$$
$$\boldsymbol{C}(t + \Delta t) \;=\; C(t) - \Delta t \, \nabla \mathcal{E} \,.$$

This new approach can then be summarized as:

$$\textbf{Energy}(t) \to \frac{\partial \mathcal{E}}{\partial t} = \langle \nabla \mathcal{E}, \, C_t \rangle \to \textbf{gradient descent}$$

Example 4 *In example 3 the classic variational calculation result was obtained. Here the evolution flow is obtained for the same energy following the approach for curves.*

$$\frac{dE}{dt} \;=\; \frac{1}{2}\frac{d}{dt}\int_0^1 \boldsymbol{C}_p(t) \cdot \boldsymbol{C}_p(t) \, dp \tag{6.41}$$

$$=\; \int_0^1 \boldsymbol{C}_{tp} \cdot \boldsymbol{C}_p \, dp \tag{6.42}$$

$$=\; -\int_0^1 \boldsymbol{C}_t \cdot \boldsymbol{C}_{pp} \, dp \tag{6.43}$$

$$=\; \langle \boldsymbol{C}_t, \, -\boldsymbol{C}_{pp} \rangle_{L^2} \,. \tag{6.44}$$

In eq. 6.41 t, p are independent and time derivatives were moved inside

In eq. 6.42 t, p were switched

In eq. 6.43 integration by parts was performed assuming a fixed boundary

finally the gradient descent is deliberately set as

$$\boldsymbol{C}_t \;=\; \boldsymbol{C}_{pp} \,, \tag{6.45}$$

which corresponds to the previous result (eq. 6.37).

The last example shows how the second approach reproduces the classic result; obviously since one of the key ingredients is the energy, it must be built to be geometric.

It should be noted that the second ingredient, the $L_2(0,1)$ inner product, is defined by an integration on the curve. Unlike the first approach, where integration was on a fixed domain, here the integral is on the evolving curve which is not fixed. Consequently many of basic theorems that can be found in a classic Calculus of Variation book are no longer valid. The inner product has to be expressed in a geometric way, which is accomplished by exploiting the arclength as a parameter, and the *geometric inner product* assumes the form

$$\langle f, \, g \rangle = \int_0^L f(s)g(s)ds \, . \tag{6.46}$$

Summary of the Gradient descent computation method for geometric energies:

- Propose curve-dependent energy that is geometric.

$$\mathcal{E}(\boldsymbol{C}) = \int_{\boldsymbol{C}} L \, ds \, . \tag{6.47}$$

- Compute the time derivative $\frac{dE}{dt}$ rewriting the energy with a dummy arbitrary parameter which is time independent.

- Manipulate $\frac{dE}{dt}$ until something with the form

$$\frac{dE}{dt} = \int_C \boldsymbol{C}_t \cdot (\boldsymbol{G}) \, ds \tag{6.48}$$

   is obtained.

- Set the gradient descent flow as $\boldsymbol{C}_t = -\boldsymbol{G}$

6.3   Adjoint Active Curves Inversion

In the former section concepts of flow minimization were introduced. The field of application is mainly related to computer vision technology; in particular the minimization technique outlined is the basic concept of what is referred to as *active contours.*

This technique has been introduced in the last fifteen years, and today is one of the most effective techniques for image segmentation. A nice feature of this machinery is that it can be specialized following two main approaches:

- **Boundary-based active contours**
  The Energy is written in terms of a curve and then minimized. It can be proven that starting from an energy of the form

$$\mathcal{E} = \int_{\boldsymbol{C}} \phi \, ds \,, \tag{6.49}$$

  and once the energy derivative with respect to time has been calculated

$$\frac{d}{dt}\mathcal{E} = \int_{\boldsymbol{C}(t)} \left(K\phi \boldsymbol{N} - (\nabla\phi \cdot \boldsymbol{N}) \, \boldsymbol{N} \right) \boldsymbol{C}_t ds \,, \tag{6.50}$$

  the resulting gradient takes the form

$$\nabla\mathcal{E} = K\phi \boldsymbol{N} - (\nabla\phi \cdot \boldsymbol{N}) \, \boldsymbol{N} \,. \tag{6.51}$$

- **Region-based active contours**
  The Energy is written in terms of domain quantities. The domain integral is then transformed into a boundary integral and minimized. The initial energy

$$\mathcal{E} = \iint_{\text{inside } \boldsymbol{C}} F(\boldsymbol{C}(t)) \, dA \,, \tag{6.52}$$

  leads to the gradient

$$\nabla\mathcal{E} = F(\boldsymbol{C}(t)) \, \boldsymbol{N} \,. \tag{6.53}$$

Equations 6.51 6.53 were exploited in conjunction with the *Adjoint Method* to obtain a minimizing inversion algorithm.

6.3.1   Problem definition

Consider a distribution of n_f sources located at coordinates $\boldsymbol{x}_f$ on the soil surface (Γ_0). Given a distribution of n_s sensors on the soil surface, located at coordinates $\boldsymbol{x}_k$, displacements produced are recorded and indicated with $\widetilde{\mathbf{u}}(\omega, \boldsymbol{x}_k)$, where $k \in \{1, 2, ..., n_s\}$.

The subsoil structure is assumed to be piecewise layered with generally non-flat boundaries. Let Ω_i be the general layer between Γ_{i-1} and Γ_i interfaces. The whole

Symbol	Meaning
Γ	Union of all boundaries
Γ_0	Soil surface
Γ_i	Boundary between layers
Ω_i	Layer Internal area
Ω	$\cup \Omega_i$
k	Number of receivers
$(\cup \boldsymbol{x}_f)$	Sources locations
$(\cup \boldsymbol{x}_k)$	Receivers locations
$\mathbf{u}(\omega, \boldsymbol{x})$	Particle Displacements
$\widetilde{\mathbf{u}}(\omega, \boldsymbol{x}_k)$	Particle displacements (Data)
$\mathcal{L}\mathbf{v} = 0$	Navier's wave equation $T_{ij,j} + \rho\omega^2 v_i = 0$

Table 6.1: Notations for Analytic Shape Derivative

set of layers is indicated as $\Omega = \cup_{i=1}^{\infty} \Omega_i$ and the whole set of boundaries is indicated as $\Gamma = \cup_{i=0}^{\infty} \Gamma_i$.

The materials constituting the layers are assumed to be linear, isotropic, elastic, homogeneous and particles motion is assumed to obey to Navier's equation of motion. Function **u** describing particle displacements is assumed to exist and belonging to C^2 class. For the sake of clarity, the notations are summarized in table 6.1.
FIGURE

6.3.2 Energy Definition

Setting up the variational minimization approach requires building an objective function. It is a natural choice to require the vector distance between the model calculated values of displacements and the given data to be a minimum value; this results in a misfit term $\mathcal{E}_M$ which expresses mathematically the request in a least squared sense. Next, the final energy form can be obtained by a suitable choice of regularizer. A feature which must be included is the physics law of wave motion. In chapter 5 this feature was implicitly included by the numerical Jacobian J. Indeed, its calculation was performed by perturbing the interface, running the forward model and then applying finite difference approximation. Wave motion law was then directly inherited by the inverse algorithm.

Conditions on $\mathbf{u}$	Scope
$\mathcal{L}\mathbf{u} = T_{ij,j}^{(\mathbf{u})} + \rho\omega^2 u_i = 0$	In Ω
$\mathbf{T}^{(\mathbf{u})} \cdot \hat{\boldsymbol{N}} = 0$	On $\Gamma_0/ \left(\cup \boldsymbol{x}_f \right)$
$\mathbf{T}^{(\mathbf{u})} \cdot \hat{\boldsymbol{N}} = \mathbf{F}$	On $\left(\cup \boldsymbol{x}_f \right)$
$[\mathbf{u}]_{\Gamma_i} = 0$	At Γ_i
$\left[\mathbf{T}^{(\mathbf{u})} \cdot \hat{\boldsymbol{N}} \right]_{\Gamma i} = 0$	At Γ_i
Conditions on $\mathbf{w}$	Scope
$\mathcal{L}\mathbf{w} = T_{ij,j}^{(\mathbf{w})} + \rho\omega^2 w_i = 0$	In Ω
$\boldsymbol{u}_t \cdot \boldsymbol{T}^{(\boldsymbol{w},1)} \boldsymbol{N}^0 + c.c = - \left\{ 2\left(\mathbf{u}_{[r]} - \widetilde{\mathbf{u}}_{k[r]}\right)\mathbf{u}_{[r]t} + 2\left(\mathbf{u}_{[i]} - \widetilde{\mathbf{u}}_{k[i]}\right)\mathbf{u}_{[i]t} \right\}$ so $\boldsymbol{T}^{(\boldsymbol{w})}\boldsymbol{N}^0 = -\left(\mathbf{u}_{[r]} - \widetilde{\mathbf{u}}_{k[r]}\right) + i\left(\mathbf{u}_{[i]} - \widetilde{\mathbf{u}}_{k[i]}\right)$	On $\Gamma_0/\boldsymbol{x}_k$
$\mathbf{T}^{(\mathbf{w})} \cdot \hat{\boldsymbol{N}} = 0$	On $\Gamma_0/ \left(\cup \boldsymbol{x}_f, \cup \boldsymbol{x}_k \right)$
$\mathbf{w} = \mathbf{0}$	On $\left(\cup \boldsymbol{x}_f \right)$
$[\mathbf{w}]_{\Gamma_j} = 0$	At Γ_j
$\left[\mathbf{T}^{(\mathbf{w})} \cdot \hat{\boldsymbol{N}} \right]_{\Gamma_j} = 0$	At Γ_j

Table 6.2: Wave-Fields conditions for analytic shape derivative.

In this new approach Navier's equation is introduced as the regularizer. Let's suppose that the wave equation is introduced for each point in Ω by the Lagrange multiplicator method. This can be regarded as a sum on the infinite number of particles. Now, this sum turns into an integral because continuum mechanics was assumed and the Lagrangian multiplicators are substituted by the vector function $\boldsymbol{w}$. What is remaining is the integral term $\mathcal{R}(\boldsymbol{u}, \boldsymbol{w})$ which now depends both on $\boldsymbol{u}$ and $\boldsymbol{w}$ fields.

$$
\begin{aligned}
\mathcal{E} &= \mathcal{E}_M + \mathcal{R}(\boldsymbol{u}, \boldsymbol{w}) && (6.54) \\
&= \sum_{k=1}^{n} \frac{1}{2} \|(\boldsymbol{u}(\omega, \boldsymbol{x}_k) - \widetilde{\boldsymbol{u}}(\omega, \boldsymbol{x}_k))\|^2 + \int_{\Omega} \boldsymbol{w} \cdot (\mathcal{L}\boldsymbol{u}) \, d\Omega + c.\,c. \\
&= \int_{\Gamma} g \, d\Gamma + \sum_{j} \int_{\Omega_j} \boldsymbol{w}^j \cdot \left(\mathcal{L}^j \boldsymbol{u}^j\right) d\Omega + c.\,c. \,, && (6.55)
\end{aligned}
$$

with

$$
g = \frac{1}{2} \left(\mathbf{u}(\omega, \boldsymbol{x}) - \widetilde{\mathbf{u}}_k\right)\left(\mathbf{u}(\omega, \boldsymbol{x}) - \widetilde{\mathbf{u}}_k\right)^* \delta\left(\boldsymbol{x} - \boldsymbol{x}_k\right). \tag{6.56}
$$

6.3.3 Strategy outline

Considering Energy 6.54 the artificial time dependence must be introduced to allow interfaces to evolve. The evolution of geometry then reflects in the displacement field $\boldsymbol{u}$ and the adjoint field $\boldsymbol{w}$ which now both depend on the artificial time. Eq. 6.54 must be derived with respect to time and manipulated into the form

$$
\frac{d}{dt}\mathcal{E} = \int_{\boldsymbol{\Gamma}} (\nabla \mathcal{E}) \boldsymbol{\Gamma}_t d\boldsymbol{\Gamma} \tag{6.57}
$$

as stated in sec. 6.2.2.

Note that 6.54 is composed of a boundary term and a domain term on which respectively 6.51 and 6.53 will be applied. To follow the approach outlined in sec. 6.2.2, requires extra care, in fact this environment hides an extra time dependence. Comparing 6.51 with $\mathcal{E}_M$

$$
\begin{aligned}
\mathcal{E} &= \int_C \phi(\boldsymbol{C}(t)) \, ds \\
\mathcal{E}_M &= \int_{\boldsymbol{\Gamma}(t, \boldsymbol{u}(t))} g \, ds \,,
\end{aligned}
$$

it is apparent that the integrand possesses a time dependence inherited from the evolving curve and a time dependence inherited from the displacement field, this

gives rise to an extra term and 6.51 becomes

$$\frac{d}{dt}\mathcal{E}_M = \int_{\boldsymbol{\Gamma}(t)} \left(Kg\boldsymbol{N} - (\nabla g \cdot \boldsymbol{N})\,\boldsymbol{N}\right) \boldsymbol{\Gamma}_t ds - \int_{\boldsymbol{\Gamma}(t)} g_t ds\,, \tag{6.58}$$

the same fact occurs for the region term $\mathcal{R}$, which takes the form

$$\frac{d}{dt}\mathcal{R} = \int_{\boldsymbol{\Gamma}(t)} \left(\boldsymbol{w} \cdot (\mathcal{L}\boldsymbol{u})\right) \boldsymbol{N} \cdot \boldsymbol{\Gamma}_t ds + \int_{\Omega} \left(\boldsymbol{w} \cdot (\mathcal{L}\boldsymbol{u})\right)_t d\Omega\,, \tag{6.59}$$

The extra terms in eq. 6.58 and 6.59 are times derivatives of involved quantities. They are not geometric; fortunately the adjoint field $\boldsymbol{w}$ represent an extra degree of freedom. By imposing suitable conditions (see table 6.2) on $\boldsymbol{w}$, any residual time dependent (non-geometric) term disappears and the final gradient flow is obtained.

6.3.4   Integration by parts of $\mathcal{R}$

Before manipulating the whole energy function, it is useful to simplify the regularizer term[5].

Explicit introduction of $\boldsymbol{T}$ tensor components leads to

$$\begin{aligned}
\mathcal{R}(\mathbf{u},\,\mathbf{w}) &= \int_{\Omega} \mathbf{w} \cdot (\mathcal{L}\mathbf{u})\, d\Omega \\
&= \int_{\Omega} \left[\left(T_{11,1}^{(\mathbf{u})} + T_{12,2}^{(\mathbf{u})} + \gamma u_1\right) w_1 + \left(T_{21,1}^{(\mathbf{u})} + T_{22,2}^{(\mathbf{u})} + \gamma u_2\right) w_2\right] d\Omega \\
&= -\sum_{j=1}^{\infty} \int_{\boldsymbol{\Gamma}_{j-1}} \left[\left(T_{11}^{(\mathbf{u},j)} N_x^{j-1} + T_{12}^{(\mathbf{u},j)} N_y^{j-1}\right) w_1^j + \left(T_{21}^{(\mathbf{u},j)} N_x^{j-1} + T_{22}^{(\mathbf{u},j)} N_y^{j-1}\right) w_2^j\right] d\boldsymbol{\Gamma}^{j-1} \\
&\quad + \sum_{j=1}^{\infty} \int_{\boldsymbol{\Gamma}_j} \left[\left(T_{11}^{(\mathbf{u},j)} N_x^j + T_{12}^{(\mathbf{u},j)} N_y^j\right) w_1^j + \left(T_{21}^{(\mathbf{u},j)} N_x^j + T_{22}^{(\mathbf{u},j)} N_y^j\right) w_2^j\right] d\boldsymbol{\Gamma}^j \\
&\quad - \sum_{j=1}^{\infty} \int_{\Omega_j} \left[T_{11}^{(\mathbf{u},j)} w_{1,1}^j + T_{12}^{(\mathbf{u},j)} w_{1,2}^j + T_{21}^{(\mathbf{u},j)} w_{2,1}^j + T_{22}^{(\mathbf{u},j)} w_{2,2}^j - \gamma^j \boldsymbol{w}^j \cdot \boldsymbol{u}^j\right] d\Omega_j \\
&\quad + c.\,c.\,.
\end{aligned}$$

---

[5]For sake of simplicity, dependencies of $\mathbf{u}$ will be dropped.

By reordering surfaces and regrouping, the following expression is obtained,

$$
\begin{aligned}
\mathcal{R}(\mathbf{u},\,\mathbf{w}) \;=\; & -\int_{\boldsymbol{\Gamma}_0} \boldsymbol{w}^0 \cdot \boldsymbol{T}^{(\mathbf{u},0)} \boldsymbol{N}^0 d\boldsymbol{\Gamma}^0 \\
& +\sum_{j=1}^{\infty} \int_{\boldsymbol{\Gamma}_j} \left\{ \boldsymbol{w}^j \cdot \boldsymbol{T}^{(\mathbf{u},j)} \boldsymbol{N}^j - \boldsymbol{w}^{j+1} \cdot \boldsymbol{T}^{(\mathbf{u},j+1)} \boldsymbol{N}^j \right\} d\boldsymbol{\Gamma}^j \\
& -\sum_{j=1}^{\infty} \int_{\Omega_j} \left[T_{11}^{(\mathbf{u},j)} w_{1,1}^j + T_{12}^{(\mathbf{u},j)} w_{1,2}^j + \right. \\
& \qquad\qquad \left. T_{21}^{(\mathbf{u},j)} w_{2,1}^j + T_{22}^{(\mathbf{u},j)} w_{2,2}^j - \gamma^j \boldsymbol{w}^j \cdot \boldsymbol{u}^j \right] d\Omega_j \\
& +c.\,c.\;,
\end{aligned}
$$

which simplifies to eq. 6.60 once conditions in table 6.2 are inserted.

$$
\begin{aligned}
\mathcal{R}(\mathbf{u},\,\mathbf{w}) \;=\; & -\sum_{j=1}^{\infty} \int_{\Omega_j} \left[T_{11}^{(\mathbf{u},j)} w_{1,1}^j + T_{12}^{(\mathbf{u},j)} w_{1,2}^j + \right. \qquad\qquad (6.60)\\
& \qquad\qquad \left. T_{21}^{(\mathbf{u},j)} w_{2,1}^j + T_{22}^{(\mathbf{u},j)} w_{2,2}^j - \gamma^j \boldsymbol{w}^j \cdot \boldsymbol{u}^j \right] d\Omega_j \\
& +c.\,c.\;.
\end{aligned}
$$

Let's define function $\mathcal{F}^j(\boldsymbol{u}^j, \boldsymbol{w}^j)$ to be the term in squared parenthesis, the contribution of the regularizer to the total energy converts the equation to

$$
\mathcal{R}(\mathbf{u},\,\mathbf{w}) = -\sum_{j=1}^{\infty} \int_{\Omega_j} \mathcal{F}^j(\boldsymbol{u}^j, \boldsymbol{w}^j)\, d\Omega_j + c.\,c.\;. \qquad\qquad (6.61)
$$

.

6.3.5   Time dependence of g function.

The data fidelity term is a complex function and its derivation with respect to time requires a special procedure. Its time dependence is inherited from the $\boldsymbol{u}$ field which is in general a complex quantity. To derive this quantity with respect to time by the chain rule means deriving a complex function respect to a complex function. This kind of derivation is equivalent to requiring that the derivative exists and it is unique at every point in the complex plane. It can be recalled that, contrary to what happens for real domain $\mathbb{R}$; $\mathbb{C}$ possesses no ordering. If a point z_p is considered,

the complex derivative evaluated at z_p must exist and be unique, approaching the point from any direction. Unfortunately terms like $z\, z^*$ do not belong to the set of functions satisfying this feature, so the simple chain rule cannot be applied.

The key observation is that there is no interest in $\frac{\partial g}{\partial \boldsymbol{u}}$, so its calculation is not necessary; on the other hand g_t can still be calculated by separating the real and imaginary parts of $\boldsymbol{u}$ and performing time derivation by chain rule on the two parts separately. The final form of g_t is obtained in a few passages,

$$\frac{dg}{dt} = 2\left(\mathbf{u}_{[r]} - \widetilde{\mathbf{u}}_{k[r]}\right)\mathbf{u}_{[r]t} + 2\left(\mathbf{u}_{[i]} - \widetilde{\mathbf{u}}_{k[i]}\right)\mathbf{u}_{[i]t}\,, \qquad (6.62)$$

where $[r]$, $[i]$ subscripts indicate real and imaginary parts respectively.

6.3.6   Energy time derivative

Exploiting 6.61 and 6.62 the derivative of energy with respect to time takes the form

$$
\begin{aligned}
\frac{d\mathcal{E}}{dt} \;=\; & \int_{\boldsymbol{\Gamma}_0} \left\{ 2\left(\mathbf{u}_{[r]} - \widetilde{\mathbf{u}}_{k[r]}\right)\mathbf{u}_{[r]t} + 2\left(\mathbf{u}_{[i]} - \widetilde{\mathbf{u}}_{k[i]}\right)\mathbf{u}_{[i]t} \right\}\, d\boldsymbol{\Gamma} \\
& - \sum_{j=1}^{\infty} \int_{\partial\Omega_j} \mathcal{F}^j(\boldsymbol{u}^j, \boldsymbol{w}^j)\left(\boldsymbol{N}\cdot\boldsymbol{\Gamma}_t\right) d\Gamma + c.\,c. \\
& - \sum_{j=1}^{\infty} \int_{\Omega_j} \Big[T_{11}^{(\mathbf{u}_t,j)} w_{1,1}^j + T_{12}^{(\mathbf{u}_t,j)} w_{1,2}^j + \\
& \qquad\qquad T_{21}^{(\mathbf{u}_t,j)} w_{2,1}^j + T_{22}^{(\mathbf{u}_t,j)} w_{2,2}^j - \gamma^j \boldsymbol{w}^j \cdot \boldsymbol{u}_t^j \Big]\, d\Omega_j + c.\,c. \\
& - \sum_{j=1}^{\infty} \int_{\Omega_j} \Big[T_{11}^{(\mathbf{u},j)} w_{t1,1}^j + T_{12}^{(\mathbf{u},j)} w_{t1,2}^j + T_{21}^{(\mathbf{u},j)} w_{t2,1}^j + \\
& \qquad\qquad T_{22}^{(\mathbf{u},j)} w_{t2,2}^j - \gamma^j \boldsymbol{w}_t^j \cdot \boldsymbol{u}^j \Big]\, d\Omega_j + c.\,c.\,,
\end{aligned}
$$

note that this takes a much simpler form once integration by parts is performed a second time(D.1; D.2)

$$
\begin{aligned}
\frac{d\mathcal{E}}{dt} \;=\; & \int_{\mathbf{\Gamma}_0} \left\{ 2\left(\mathbf{u}_{[r]} - \widetilde{\mathbf{u}}_{k[r]}\right)\mathbf{u}_{[r]t} + 2\left(\mathbf{u}_{[i]} - \widetilde{\mathbf{u}}_{k[i]}\right)\mathbf{u}_{[i]t} \right\}\, d\mathbf{\Gamma} \\
& - \sum_{j=1}^{\infty} \int_{\partial\Omega_j} \mathcal{F}^j(\boldsymbol{u}^j, \boldsymbol{w}^j)\,(\boldsymbol{N}\cdot\mathbf{\Gamma}_t)\, d\mathbf{\Gamma} + c.\,c. \\
& - \sum_{j=1}^{\infty} \left[\int_{\partial\Omega_j} \boldsymbol{u}_t^j \cdot \boldsymbol{T}^{(\boldsymbol{w},j)}\boldsymbol{N}\,d\mathbf{\Gamma} - \int_{\Omega_j} \boldsymbol{u}_t^j\cdot\mathcal{L}\boldsymbol{w}^j\,d\Omega \right] \\
& - \sum_{j=1}^{\infty} \left[\int_{\partial\Omega_j} \boldsymbol{w}_t^j \boldsymbol{T}^{(\mathbf{u},j)}\boldsymbol{N}\,d\mathbf{\Gamma} - \int_{\Omega_j} \boldsymbol{w}_t^j\cdot\boldsymbol{L}\boldsymbol{u}^j\,d\Omega_j \right].
\end{aligned}
$$

Summations on layer boundaries can be grouped with respect to the interface where they are calculated. The relation D.3 is then introduced to obtain eq. 6.63.

$$
\begin{aligned}
\frac{d\mathcal{E}}{dt} \;=\; & \int_{\mathbf{\Gamma}_0} \left\{ 2\left(\mathbf{u}_{[r]} - \widetilde{\mathbf{u}}_{k[r]}\right)\mathbf{u}_{[r]t} + 2\left(\mathbf{u}_{[i]} - \widetilde{\mathbf{u}}_{k[i]}\right)\mathbf{u}_{[i]t} \right\}\, d\mathbf{\Gamma} && (6.63) \\
& + \int_{\mathbf{\Gamma}_0} \boldsymbol{u}_t^1 \cdot \boldsymbol{T}^{(\boldsymbol{w},1)}\boldsymbol{N}^0 d\mathbf{\Gamma}^0 + \int_{\mathbf{\Gamma}_0} \boldsymbol{w}_t^1 \cdot \boldsymbol{T}^{(\boldsymbol{u},1)}\boldsymbol{N}^0 d\mathbf{\Gamma}^0 + c.\,c. \\
& - \sum_{j=1}^{\infty} \int_{\mathbf{\Gamma}_j} \left[\mathcal{F}^j(\boldsymbol{u}^j, \boldsymbol{w}^j) - \mathcal{F}^{j+1}(\boldsymbol{u}^{j+1}, \boldsymbol{w}^{j+1}) \right]\left(\boldsymbol{N}^j\cdot\mathbf{\Gamma}_t^j\right) d\mathbf{\Gamma}^j + c.\,c. \\
& - \sum_{j=1}^{\infty} \int_{\mathbf{\Gamma}_j} \left[\boldsymbol{u}_t^j \cdot \boldsymbol{T}^{(\boldsymbol{w},j)}\boldsymbol{N}^j - \cdots \right. && (6.64) \\
& \qquad\qquad \left. \left(\boldsymbol{u}_t^j + \left(\boldsymbol{D}\left(\boldsymbol{u}^j\right) - \boldsymbol{D}\left(\boldsymbol{u}^{j+1}\right)\right)\mathbf{\Gamma}_t\right)\cdot\boldsymbol{T}^{(\boldsymbol{w},j+1)}\boldsymbol{N}^j \right] d\mathbf{\Gamma}^j + c.\,c. \\
& - \sum_{j=1}^{\infty} \int_{\mathbf{\Gamma}_j} \left[\boldsymbol{w}_t^j \cdot \boldsymbol{T}^{(\mathbf{u},j)}\boldsymbol{N}^j - \cdots \right. && (6.65) \\
& \qquad\qquad \left. \left(\boldsymbol{w}_t^j + \left(\boldsymbol{D}\left(\boldsymbol{w}^j\right) - \boldsymbol{D}\left(\boldsymbol{w}^{j+1}\right)\right)\mathbf{\Gamma}_t\right)\cdot\boldsymbol{T}^{(\mathbf{u},j+1)}\boldsymbol{N}^j \right] d\mathbf{\Gamma}^j + c.\,c. \\
& + \sum_{j=1}^{\infty} \int_{\Omega_j} \boldsymbol{u}_t^j \cdot \boldsymbol{L}\boldsymbol{w}^j\,d\Omega + \sum_{j=1}^{\infty} \int_{\Omega_j} \boldsymbol{w}_t^j \cdot \boldsymbol{L}\boldsymbol{u}^j\,d\Omega_j + c.\,c. \,.
\end{aligned}
$$

Simplification of residual time dependent terms is obtained by imposing the restrictions summarized in table 6.2 on vector function $\boldsymbol{w}$. After a few passages,

$$
\begin{aligned}
\frac{d\mathcal{E}}{dt} &= -\sum_{j=1}^{\infty} \int_{\boldsymbol{\Gamma}_j} \left[\mathcal{F}^j(\boldsymbol{u}^j, \boldsymbol{w}^j) - \mathcal{F}^{j+1}(\boldsymbol{u}^{j+1}, \boldsymbol{w}^{j+1}) \right] \left(\boldsymbol{N}^j \cdot \boldsymbol{\Gamma}_t^j \right) d\boldsymbol{\Gamma}^j \\
&\quad -\sum_{j=1}^{\infty} \int_{\boldsymbol{\Gamma}_j} \left[\boldsymbol{\Gamma}_t \cdot \left(\boldsymbol{D}\left(\boldsymbol{u}^j\right) - \boldsymbol{D}\left(\boldsymbol{u}^{j+1}\right) \right)^T \right] \boldsymbol{T}^{(\boldsymbol{w}, j+1)} \boldsymbol{N}^j d\boldsymbol{\Gamma}^j \\
&\quad -\sum_{j=1}^{\infty} \int_{\boldsymbol{\Gamma}_j} \left[\boldsymbol{\Gamma}_t \cdot \left(\boldsymbol{D}\left(\boldsymbol{w}^j\right) - \boldsymbol{D}\left(\boldsymbol{w}^{j+1}\right) \right)^T \right] \boldsymbol{T}^{(\mathbf{u}, j+1)} \boldsymbol{N}^j d\boldsymbol{\Gamma}^j \\
&\quad +c.\,c.\,.
\end{aligned}
$$

which now can be written by projecting along the normal and tangential directions, obtaining the final form 6.66. By exploiting eq. D.3 and noticing that interface boundary conditions imply $(\boldsymbol{D}\left(\boldsymbol{u}\right)\boldsymbol{T} = 0)$ and $(\boldsymbol{D}\left(\boldsymbol{w}\right)\boldsymbol{T} = 0)$

$$
\begin{aligned}
\frac{d\mathcal{E}}{dt} &= -\sum_{j=1}^{\infty} \int_{\boldsymbol{\Gamma}_j} \left[\mathcal{F}^j(\boldsymbol{u}^j, \boldsymbol{w}^j) - \mathcal{F}^{j+1}(\boldsymbol{u}^{j+1}, \boldsymbol{w}^{j+1}) \right] \left(\boldsymbol{N}^j \cdot \boldsymbol{\Gamma}_t^j \right) d\boldsymbol{\Gamma}^j \\
&\quad -\sum_{j=1}^{\infty} \int_{\boldsymbol{\Gamma}_j} \left(\left[\left(\boldsymbol{D}\left(\boldsymbol{u}^j\right) - \boldsymbol{D}\left(\boldsymbol{u}^{j+1}\right) \right)^T \boldsymbol{T}^{(\boldsymbol{w}, j+1)} \boldsymbol{N}^j \right] \cdot \boldsymbol{N}^j \right) \left(\boldsymbol{N}^j \cdot \boldsymbol{\Gamma}_t \right) d\boldsymbol{\Gamma}^j \\
&\quad -\sum_{j=1}^{\infty} \int_{\boldsymbol{\Gamma}_j} \left(\left[\left(\boldsymbol{D}\left(\boldsymbol{u}^j\right) - \boldsymbol{D}\left(\boldsymbol{u}^{j+1}\right) \right)^T \boldsymbol{T}^{(\boldsymbol{w}, j+1)} \boldsymbol{N}^j \right] \cdot \mathbf{T}^j \right) \left(\mathbf{T}^j \cdot \boldsymbol{\Gamma}_t \right) d\boldsymbol{\Gamma}^j \\
&\quad -\sum_{j=1}^{\infty} \int_{\boldsymbol{\Gamma}_j} \left(\left[\left(\boldsymbol{D}\left(\boldsymbol{w}^j\right) - \boldsymbol{D}\left(\boldsymbol{w}^{j+1}\right) \right)^T \boldsymbol{T}^{(\mathbf{u}, j+1)} \boldsymbol{N}^j \right] \cdot \boldsymbol{N}^j \right) \left(\boldsymbol{N}^j \cdot \boldsymbol{\Gamma}_t \right) d\boldsymbol{\Gamma}^j \\
&\quad -\sum_{j=1}^{\infty} \int_{\boldsymbol{\Gamma}_j} \left(\left[\left(\boldsymbol{D}\left(\boldsymbol{w}^j\right) - \boldsymbol{D}\left(\boldsymbol{w}^{j+1}\right) \right)^T \boldsymbol{T}^{(\mathbf{u}, j+1)} \boldsymbol{N}^j \right] \cdot \mathbf{T}^j \right) \left(\mathbf{T}^j \cdot \boldsymbol{\Gamma}_t \right) d\boldsymbol{\Gamma}^j \,.
\end{aligned}
$$

Finally

$$
\mathcal{E}_t = \sum_{j=1}^{\infty} \int_{\boldsymbol{\Gamma}_j} F \left(\boldsymbol{N}^j \cdot \boldsymbol{\Gamma}_t \right) d\boldsymbol{\Gamma}^j \,, \tag{6.66}
$$

where

$$
\begin{aligned}
F \;=\; \Big\{ \;&\Big[T_{11}^{(\mathbf{u},j+1)} w_{1,1}^{j+1} + T_{12}^{(\mathbf{u},j+1)} w_{1,2}^{j+1} + T_{21}^{(\mathbf{u},j+1)} w_{2,1}^{j+1} \\
&+ T_{22}^{(\mathbf{u},j+1)} w_{2,2}^{j+1} - \gamma^{j+1} \boldsymbol{w}^{j+1} \cdot \boldsymbol{u}^{j+1} \Big] \\
&- \Big[T_{11}^{(\mathbf{u},j)} w_{1,1}^{j} + T_{12}^{(\mathbf{u},j)} w_{1,2}^{j} + T_{21}^{(\mathbf{u},j)} w_{2,1}^{j} + T_{22}^{(\mathbf{u},j)} w_{2,2}^{j} - \gamma^{j} \boldsymbol{w}^{j} \cdot \boldsymbol{u}^{j} \Big] \\
&- \Big(\Big[\big(\boldsymbol{D}\left(\boldsymbol{u}^{j}\right) - \boldsymbol{D}\left(\boldsymbol{u}^{j+1}\right) \big)^{T} \boldsymbol{T}^{(w,j+1)} \boldsymbol{N}^{j} \Big] \cdot \boldsymbol{N}^{j} \Big) \\
&- \Big(\Big[\big(\boldsymbol{D}\left(\boldsymbol{w}^{j}\right) - \boldsymbol{D}\left(\boldsymbol{w}^{j+1}\right) \big)^{T} \boldsymbol{T}^{(\mathbf{u},j+1)} \boldsymbol{N}^{j} \Big] \cdot \boldsymbol{N}^{j} \Big) \Big\} \,.
\end{aligned}
\tag{6.67}
$$

6.3.7 Curve Update:

Equation 6.66 is now in a suitable form and it leads to the update formula

$$
\boldsymbol{\Gamma}_{t} \;=\; -F \cdot \boldsymbol{N} \,,
\tag{6.68}
$$

which rules the evolution of all the points on the curve.
Actually, since interfaces in the forward model are sets of elements and actual points on each element are obtained by interpolating nodal coordinates[6] according to eq. 4.56-4.58, it is necessary to customize 6.66. In this scope, a parameters vector $V(t)$ is defined as the vector containing all nodal coordinates:

$$
\boldsymbol{V}(t) = \left(x_1(t),\, y_1(t)\, x_2(t),\, y_2(t)\, \ldots\, x_n(t),\, y_n(t) \right)^{T} \,,
\tag{6.69}
$$

as a consequence the updated formula can be written as

$$
\dot{\boldsymbol{V}}(t) = -\nabla \mathcal{E} \boldsymbol{V}(t) \,,
\tag{6.70}
$$

where

$$
\nabla \mathcal{E} =
\begin{pmatrix}
\frac{\partial \mathcal{E}}{\partial x_1} \\
\frac{\partial \mathcal{E}}{\partial y1} \\
\vdots \\
\vdots \\
\frac{\partial \mathcal{E}}{\partial x_n} \\
\frac{\partial \mathcal{E}}{\partial y_n}
\end{pmatrix}
.
\tag{6.71}
$$

---

[6]Note that assumption of continuity for $\boldsymbol{u}$ field forbids use of QDE on interface elements. This, in fact would introduce discontinuity to element extremes

Each term in 6.71 is finally calculated by

$$\frac{\partial \mathcal{E}}{\partial \alpha_i} = \sum_1^{n_e} \int_{-1}^1 \left[F \left(\mathbf{\Gamma}_{\alpha_i} \cdot \mathbf{N} \right) \| \mathbf{\Gamma}_\eta \| \right]_{(\eta)} d\eta$$

$$= \sum_1^{n_e} \int_{-1}^1 \left[F \left(\mathbf{\Gamma}_{\alpha_i} \cdot \mathbf{J}\, \mathbf{\Gamma}_\eta \right) \right]_{(\eta)} d\eta \,,$$

where n_e is the number of elements and α_i is one of the parameters in $V(t)$.
It is straightforward that only elements depending upon the node with respect to which derivative is performed will contribute to displacing the respective node. Finally, time step Δt is chosen and displaced nodes at each iteration are obtained evolving nodes at earlier time.

$$x_i(t + \Delta t) = x_i(t) - \frac{\partial \mathcal{E}}{\partial x_i} \Delta t \tag{6.72}$$

$$y_i(t + \Delta t) = y_i(t) - \frac{\partial \mathcal{E}}{\partial y_i} \Delta t \,. \tag{6.73}$$

6.3.8   Adding the Curvature regularizer.

The formulation presented in the former section introduced a regularizer which forces the system to obey to a certain physical law such as Navier's Equation of motion.

Even if satisfactory, the desired behavior of the algorithm is to start with a set of guessed simple interfaces, namely parallel planes, and obtain a non-layered model which fits the data. It is then necessary to introduce a second regularizer for which its purpose is to evolve interfaces shrinking the length, and resulting in a smoothing effect. Computation of this term starts from the geometric energy formula

$$\mathcal{E}_l = \int_\Gamma ds \,, \tag{6.74}$$

where ds is the arclength measure, and follows the same steps used to obtain 6.72, 6.73. Collecting all of the parts together

$$\boldsymbol{\alpha}_i(t + \Delta t) = \boldsymbol{\alpha}_i(t) - \frac{\partial E_k}{\partial \boldsymbol{\alpha}_i} \Delta t \,,$$

with

$$
\frac{\partial E_k}{\partial \alpha_i} \;=\; \sum_{1}^{n_e} \Bigg\{ \int_{-1}^{1} \left[F \left(\mathbf{\Gamma}_{\alpha_i} \cdot \mathbf{N} \right) \, \|\mathbf{\Gamma}_{\eta}\| \right]_{(\eta)} \, d\eta
$$

$$
+ \beta \left(\int_{-1}^{1} \left[K \left(\mathbf{\Gamma}_{\alpha_i} \cdot \mathbf{N} \right) \, \|\mathbf{\Gamma}_{\eta}\| \right]_{(\eta)} \, d\eta + \left(\mathbf{\Gamma}_{\alpha_i} \cdot \mathbf{T} \right)\big|_{-1}^{1} \right) \Bigg\} , \qquad (6.75)
$$

and β is simply an arbitrary weight.

Chapter 7

Conclusions.

In this research effort, an overview of SWM was given. It is understood that layered models classically exploited to investigate surface waves are seriously inadequate for cases in which the real soil structure presents an non-flat surface, steep lithological interfaces or voids, expecially because they usually correspond to acoustic impedance discontinuities.

Introduction of such features seriously compromises the reflection/diffraction pattern which gave rise to Love and Rayleigh waves. As a result, layer modelization is inadequate and unfortunately, the classic SWM elaboration process gives no indication of the real soil structure. To overcome such limitations, a novel approach has been proposed coupling the mathematically advanced boundary element method and inversion theory to investigate the possibility of a full wavefield inversion.

This method has been tested against synthetic data and partially on real data and it has been proven robust.

Moreover synthetic simulation shows that in "in plane" problems can in general be investigated exploiting just the vertical component of the wave-motion.

Finally a coupling between active curves, introduced only fifteen years ago in the field of computer vision and imaging, and the adjoint field method was exploited to build the theoretical basis of a new class of shape optimization solver for subsoil structure determination. This proposed method can be fully generalized to soils of any degree of complexity, to three-dimensional domains, and to non-flat surface environments.

Viscoelasticity can be taken into account as well.

Appendix A

Detaills of Lagrangian Model.

A.0.9 Proof of the Action principle

Starting with formulation for Lagrangian (4.24) we expand the variation and integrate on space and time domain. Wrote explicitly Lagrangian reads

$$
\begin{aligned}
L \;=\; & 1/2 \int_{0}^{\eta_{(x)}} \rho_1 \Big(\frac{\partial v_{1_{II}}}{\partial t}\Big)^2 - \mu_1 \Big[\Big(\frac{\partial v_{1_{II}}}{\partial x}\Big)^2 + \Big(\frac{\partial v_{1_{II}}}{\partial z}\Big)^2\Big] \, dz \\
+ \; & 1/2 \int_{\eta_{(x)}}^{\infty} \rho_2 \Big(\frac{\partial v_{2_{II}}}{\partial t}\Big)^2 - \mu_2 \Big[\Big(\frac{\partial v_{2_{II}}}{\partial x}\Big)^2 + \Big(\frac{\partial v_{2_{II}}}{\partial z}\Big)^2\Big] \, dz \\
- \; & \mu_2 \Big(\frac{\partial v_{2_{II}}}{\partial z} - \frac{\partial v_{2_{II}}}{\partial x}\frac{\partial \eta_{(x)}}{\partial x}\Big)(v_{2_{II}} - v_{1_{II}}) \mid_{z=\eta_{(x)}} \\
+ \; & \int_{0}^{\infty} \mu \frac{\partial v_I}{\partial x} \big(v_{II} - 1/2 v_I - v_i\big) \mid_{x=-L} dz \\
- \; & \int_{0}^{\infty} \mu \frac{\partial v_{III}}{\partial x} \big(v_{II} + 1/2 v_{III}\big) \mid_{x=L} dz
\end{aligned}
$$

Romans subscript (I, II, III) indicates the region, numeric subscript (1, 2) indicates respectively the upper and lower media.

117

$$\delta \int_{t_1}^{t_2} \int_{\Omega} L \; d\Omega \; dt =$$

$$+ \int_{t_1}^{t_2} \int_{x_1}^{x_2} \int_0^{\eta_{(x)}} \rho_1 \frac{\partial v_{1_{II}}}{\partial t} \frac{\partial}{\partial t} \delta v_{1_{II}} - \mu_1 (\frac{\partial v_{1_{II}}}{\partial x} \frac{\partial}{\partial x} \delta v_{1_{II}} + \frac{\partial v_{1_{II}}}{\partial z} \frac{\partial}{\partial z} \delta v_{1_{II}}) \; dz \; dx \; dt$$

$$+ \int_{t_1}^{t_2} \int_{x_1}^{x_2} \int_{\eta_{(x)}}^{\infty} \rho_2 \frac{\partial v_{2_{II}}}{\partial t} \frac{\partial}{\partial t} \delta v_{2_{II}} - \mu_2 (\frac{\partial v_{2_{II}}}{\partial x} \frac{\partial}{\partial x} \delta v_{2_{II}} + \frac{\partial v_{2_{II}}}{\partial z} \frac{\partial}{\partial z} \delta v_{2_{II}}) \; dz \; dx \; dt$$

$$- \int_{t_1}^{t_2} \int_{x_1}^{x_2} \mu_2 (\frac{\partial}{\partial z} \delta v_{2_{II}} - \frac{\partial}{\partial x} \delta v_{2_{II}} \frac{\partial \eta_{(x)}}{\partial x}) (v_{2_{II}} - v_{1_{II}}) \; |_{z = \eta_{(x)}} \; dx \; dt$$

$$- \int_{t_1}^{t_2} \int_{x_1}^{x_2} \mu_2 (\frac{\partial v_{2_{II}}}{\partial z} - \frac{\partial v_{2_{II}}}{\partial x} \frac{\partial \eta_{(x)}}{\partial x}) (\delta v_{2_{II}} - \delta v_{1_{II}}) \; |_{z = \eta_{(x)}} \; dx \; dt$$

$$+ \int_{t_1}^{t_2} \int_0^{\infty} \mu \frac{\partial v_I}{\partial x} (\delta v_{II} - 1/2 \delta v_I - \delta v_i) \; |_{x = -L} \; dz$$

$$+ \int_{t_1}^{t_2} \int_0^{\infty} \mu \frac{\partial \delta v_I}{\partial x} (v_{II} - 1/2 v_I - v_i) \; |_{x = -L} \; dz$$

$$+ \int_{t_1}^{t_2} \int_0^{\infty} \mu \frac{\partial v_{III}}{\partial x} (\delta v_{II} - 1/2 \delta v_{III}) \; |_{x = L} \; dz$$

$$- \int_{t_1}^{t_2} \int_0^{\infty} \mu \frac{\partial \delta v_{III}}{\partial x} (v_{II} + 1/2 v_{III}) \; |_{x = L} \; dz$$

In order to expose relevant features we must perform integration by parts, then lets switch to a compact notation for integrations, We will write integration variables as subscripts, so for example let be

$$\int_{t_1}^{t_2} \int_{x_1}^{x_2} \int_0^{\infty} \; dz \; dt \to \langle \; \rangle_{x,z,t} \qquad (A.1)$$

$$\begin{aligned}
v_I &= v_i + v_r = I_n \; e^{ik_n(x+L)} + R_n \; e^{-ik_n(x+L)} \\
\delta v_I &= \delta R_n \; e^{-ik_n(x+L)} \\
\frac{\partial \; \delta v_I}{\partial x} &= -ik_n \delta R_n \; e^{-ik_n(x+L)} = -ik_n \delta v_I \\
v_{III} &= T_n \; e^{ik_n(x-L)} \\
\delta v_{III} &= \delta T_n \; e^{ik_n(x-L)} \\
\frac{\partial \; \delta v_{III}}{\partial x} &= ik_n \delta T_n \; e^{ik_n(x-L)} = ik_n \delta v_{III}
\end{aligned} \qquad (A.2)$$

Expanding surface integrals, after some simplifications, reordering and exploiting the properties of the wave ansatz (4.33 - 4.34 - A.2), δA reads.

$$\delta A = \left\langle(-\rho\frac{\partial^2 v_{II}}{\partial t^2} + \mu\frac{\partial^2 v_{II}}{\partial x^2} + \mu\frac{\partial^2 v_{II}}{\partial z^2})\delta v_{II}\right\rangle_{x,z,t} \tag{A.3}$$

$$+\left[\left\langle\rho\frac{\partial v_{II}}{\partial t}\delta v_{II}\right\rangle_{x,z}\right]_{t_1}^{t_2} \tag{A.4}$$

$$-\left\langle\mu_1(\frac{\partial v_{1_{II}}}{\partial z})\delta v_{1_{II}}\mid_{z=0}\right\rangle_{x,t} \tag{A.5}$$

$$+\left\langle\mu_2(\frac{\partial v_{2_{II}}}{\partial z})\delta v_{2_{II}}\mid_{z\to\infty}\right\rangle_{x,t} \tag{A.6}$$

$$+\left\langle\left[\mu_2(\frac{\partial v_{2_{II}}}{\partial x}n_x + \frac{\partial v_{2_{II}}}{\partial z}n_z) - \mu_1(\frac{\partial v_{1_{II}}}{\partial x}n_x + \frac{\partial v_{1_{II}}}{\partial z}n_z)\right]\delta v_{1_{II}}\mid_{z=\eta_{(x)}}\right\rangle_{x,t} \tag{A.7}$$

$$-\left\langle\mu_2(\frac{\partial\delta v_{2_{II}}}{\partial x}n_x + \frac{\partial\delta v_{2_{II}}}{\partial z}n_z)(v_{2_{II}} - v_{2_{II}})\mid_{z=\eta_{(x)}}\right\rangle_{x,t} \tag{A.8}$$

$$+\left\langle\left[\mu\frac{\partial v_I}{\partial x} - \mu(\frac{\partial v_{II}}{\partial x})\right]\delta v_{II}\mid_{x=x_1}\right\rangle_{z,t} \tag{A.9}$$

$$+\left\langle\left[\mu(\frac{\partial v_{II}}{\partial x}) - \mu(\frac{\partial v_{III}}{\partial x})\right]\delta v_{II}\mid_{x=x_2}\right\rangle_{z,t} \tag{A.10}$$

$$-i\mu k_{n(-L)}\left\langle\delta v_I(v_I - v_{II})\mid_{x=x_1}\right\rangle_{z,t} \tag{A.11}$$

$$-i\mu k_{n(L)}\left\langle\delta v_{III}(v_{III} - v_{II})\mid_{x=x_2}\right\rangle_{z,t} \tag{A.12}$$

In this form many features can be easily recognized. Due to the fact that δv_I, $\delta v_{1_{II}}$, $\delta v_{2_{II}}$, δv_{III} are arbitrary, the only way for δA to be zero is other quantities in integrands goes to zero. This leads to the following interpretations:

- (A.3) Wave Equation.

- (A.4) Conservation law.

- (A.5) Zero stress condition at free surface.

- (A.6) Zero amplitude condition at $z \to \infty$.

- (A.7) Continuity of stress at interface.

- (A.8) Continuity of displacements at interface.

- (A.9) Continuity of stress between I-II region separation.

- (A.10) Continuity of stress between II-III region separation.

- (A.11) Continuity of wavefunctions between I-II region separation.

- (A.12) Continuity of wavefunctions between II-III region separation.

A.0.10   Lagrangian minimization

By introducing ansatz 4.35 in 4.24 we obtain a second order differential equations system. Constants here are presented in synthetic form even if they are valid for every x-point of the discretization.

$$E_{1_{ij}} = -(1/2)e^{i(k_i-k_j)x}(\beta_{1i,j}\mu_1 + \beta_{2i,j}\mu_2)$$

$$E_{2_{ij}} = 1/2e^{i(k_i-k_j)x}(\mu_1(\beta_{1i,j_x} - \beta_{1i_x,j} - \frac{\partial\beta_{1i,j}}{\partial x} + 2\beta_{1i,j}\ \Psi)$$

$$+\mu_2(\beta_{2i,j_x} - \beta_{2i_x,j} - \frac{\partial\beta_{2i,j}}{\partial x} + 2\beta_{2i,j}\ \Psi))$$

$$E_{3_{ij}} = 1/2e^{i(k_i-k_j)x}(-\omega^2(\beta_{1i,j}\rho_1 + \beta_{2i,j}\rho_2)$$

$$+\mu_1(\beta_{1i_x,j_x} + \beta_{1i_z,j_z} - \frac{\partial\beta_{1i_x,j}}{\partial x} + (\beta_{1i_x,j} + \frac{\partial\beta_{1i,j}}{\partial x} - \beta_{1i,j_x})\ \Psi + \beta_{1i,j}\Phi)$$

$$+\mu_2(\beta_{2i_x,j_x} + \beta_{2i_z,j_z} - \frac{\partial\beta_{2i_x,j}}{\partial x} + (\beta_{2i_x,j} + \frac{\partial\beta_{2i,j}}{\partial x} - \beta_{2i,j_x})\ \Psi + \beta_{2i,j}\Phi))$$

With:

$$\Psi = -i(k_i + \frac{\partial k_i}{\partial x}x)$$

$$\Phi = k_i^2 - i\frac{\partial k_i}{\partial x} - i\frac{\partial^2 k_i}{\partial x^2}x + 2k_i\frac{\partial k_i}{\partial x}x + \left(\frac{\partial k_i}{\partial x}\right)^2 x^2$$

$$\beta_{\Omega n,m} = \int_0^{\eta(x)} f_{\Omega_m} f_{\Omega_n} dz$$

$$\beta_{\Omega n,m_x} = \int_0^{\eta(x)} f_{\Omega_n} \frac{\partial f_{\Omega_m}}{\partial x} dz$$

$$\beta_{\Omega n_x,m} = \int_0^{\eta(x)} f_{\Omega_m} \frac{\partial f_{\Omega_n}}{\partial x} dz$$

$$\beta_{\Omega n_x,m_x} = \int_0^{\eta(x)} \frac{\partial f_{\Omega_m}}{\partial x} \frac{\partial f_{\Omega_n}}{\partial x} dz$$

$$\beta_{\Omega n_z,m_z} = \int_0^{\eta(x)} \frac{\partial f_{\Omega_m}}{\partial z} \frac{\partial f_{\Omega_n}}{\partial z} dz$$

Appendix B

Integral reppresentation for SH Waves.

Fourier transform of eq. 4.13, leads to the Helmholtz's equation, here reported with the corresponding and fundamental solution

$$c_2^2 \bar{u}_{3,\alpha\alpha} + \bar{b}_3 = -\omega^2 \bar{u}_3$$

$$\bar{u}_{33}^* = \frac{i\bar{b}_3(\omega)}{4\rho c_2^2} H_0^{(1)}\left(\frac{\omega r}{c_2}\right)$$

Where $H_0^{(1)}$ is the Hankel function of the first kind and order zero.

Integral formulation for antiplane case (eq. 4.13) in frequency domain is obtained exloiting Green's second identity.

$$\epsilon(\xi)\bar{u}_3(\xi) = \int_s \left[\bar{u}_3(\mathbf{x})\frac{\partial}{\partial \hat{n}}\left(\bar{u}_{33}^*/\bar{b}_3(\omega)\right) - \frac{\partial \bar{u}_3(\mathbf{x})}{\partial \hat{n}}\left(\bar{u}_{33}^*/\bar{b}_3(\omega)\right)\right] ds(\mathbf{x})$$

where $\epsilon(\xi) = 1/2$ for smooth boundaryes.

Appendix C

Green functions for P-SV/3D elastodynamic.

Fundamental solution of elastodynamics in frequency domain and unbounded space are listed below. Both cases, displacements and tractions can be collectively written as

$$\boldsymbol{U}_{ji}(\mathbf{x}, \mathbf{s}) = \frac{1}{\alpha \, \pi \, \rho \, C_s^2} \left(\psi \, \delta_{ij} - \chi \, r_{,i} \, r_{,j} \right) \tag{C.1}$$

$$\boldsymbol{T}_{ji}(\mathbf{x}, \mathbf{s}) = \frac{1}{\alpha \, \pi} \left[\left(\frac{d\psi}{dr} - \frac{1}{r}\chi \right) \left(\frac{\partial r}{\partial N} \delta_{ij} + r_{,i} \, N_j \right) \right. \tag{C.2}$$

$$- \frac{2}{r}\chi \left(r_{,j} \, N_i - 2 r_{,i} \, r_{,j} \frac{\partial r}{\partial N} \right) - 2\frac{d\chi}{dr} r_{,i} \, r_{,j} \frac{\partial r}{\partial N}$$

$$\left. + \left(\frac{C_p^2}{C_s^2} - 2 \right) \left(\frac{d\psi}{dr} - \frac{d\chi}{dr} - \frac{\alpha}{2r} \right) r_{,j} \, N_i \right] \tag{C.3}$$

- **2D: P-SV(plane strain)**

$$\alpha = 2$$

$$\psi = K_0 \left(k_s \, r \right) + \frac{1}{k_s \, r} \left[K_1 \left(k_s \, r \right) - \frac{C_s}{C_p} K_1 \left(k_p \, r \right) \right]$$

$$\chi = K_2 \left(k_s \, r \right) - \frac{C_s^2}{C_p^2} K_2 \left(k_p \, r \right)$$

$$- \frac{C_s^2}{C_p^2} \left(\frac{3}{k_p^2 \, r^2} + \frac{3}{k_p \, r} + 1 \right) \frac{exp \left(-k_p \, r \right)}{r}$$

125

where K_0, K_1, K_2 are Bessel's functions respectively of zeroth, first, second order and $k_s = i\omega/C_s$, $k_p = i\omega/C_p$

- **3D:**

$$\alpha = 4$$

$$\psi = \left(\frac{1}{k_s^2 \, r^2} + \frac{1}{k_s \, r} + 1 \right) \frac{exp\,(-k_s \, r)}{r}$$
$$- \frac{C_s^2}{C_p^2} \left(\frac{1}{k_p^2 \, r^2} + \frac{1}{k_p \, r} \right) \frac{exp\,(-k_p \, r)}{r}$$

$$\chi = \left(\frac{3}{k_s^2 \, r^2} + \frac{3}{k_s \, r} + 1 \right) \frac{exp\,(-k_s \, r)}{r}$$
$$- \frac{C_s^2}{C_p^2} \left(\frac{3}{k_p^2 \, r^2} + \frac{3}{k_p \, r} + 1 \right) \frac{exp\,(-k_p \, r)}{r}$$

Appendix D

Details of Analytical Shape Derivative.

Details of integration by parts

$$\int_{\Omega_j} \left[T_{11}^{(\mathbf{u}_t,j)} w_{1,1}^j + T_{12}^{(\mathbf{u}_t,j)} w_{1,2}^j + T_{21}^{(\mathbf{u}_t,j)} w_{2,1}^j + T_{22}^{(\mathbf{u}_t,j)} w_{2,2}^j - \gamma^j \boldsymbol{w}^j \cdot \boldsymbol{u}_t^j \right] d\Omega_j$$

$$= \int_{\partial\Omega_j} \left(\lambda^j \left(u_{t1}^j N_x + u_{t2}^j N_y \right) + 2\mu^j u_{t1}^j N_x \right) w_{1,1}^j + \mu^j \left(u_{t1}^j N_y + u_{t2}^j N_x \right) \left(w_{1,2}^j + w_{2,1}^j \right)$$

$$+ \left(\lambda^j \left(u_{t1}^j N_x + u_{t2}^j N_y \right) + 2\mu^j u_{t2}^j N_y \right) w_{2,2}^j$$

$$- \int_{\Omega_j} \left\{ \lambda^j \left(u_{t1}^j w_{1,11}^j + u_{t2}^j w_{1,12}^j \right) + 2\mu^j u_{t1}^j w_{1,11}^j + u_{t1}^j \mu^j \left(w_{1,22}^j + w_{2,12}^j \right) \right.$$

$$+ u_{t2}^j \mu^j \left(w_{1,21}^j + w_{2,11}^j \right) + \lambda^j \left(u_{t1}^j w_{2,21}^j + u_{t2}^j w_{2,22}^j \right) + 2\mu^j u_{t2}^j w_{2,22}^j + \gamma^j \boldsymbol{w}^j \cdot \boldsymbol{u}_t^j \right\} d\Omega$$

$$= \int_{\partial\Omega_j} \left\{ u_{t1}^j \left[\left(\lambda^j \left(w_{1,1}^j + w_{2,2}^j \right) + 2\mu^j w_{1,1}^j \right) N_x + \mu^j \left(w_{1,2}^j + w_{2,1}^j \right) N_y \right] \right.$$

$$+ u_{t2}^j \left[\mu^j \left(w_{1,2}^j + w_{2,1}^j \right) N_x + \left(\lambda^j \left(w_{1,1}^j + w_{2,2}^j \right) + 2\mu^j w_{2,2}^j \right) N_y \right] \right\} d\Gamma$$

$$- \int_{\Omega_j} \left\{ u_{t1}^j \left[\frac{\partial}{\partial x} \left(\lambda^j \left(w_{1,1}^j + w_{2,2}^j \right) + 2\mu^j w_{1,1}^j \right) + \frac{\partial}{\partial y} \mu^j \left(w_{1,2}^j + w_{2,1}^j \right) \right] \right.$$

$$+ u_{t2}^j \left[\frac{\partial}{\partial y} \left(\lambda^j \left(w_{1,1}^j + \lambda^j w_{2,2}^j \right) + 2\mu^j w_{2,2}^j \right) + \frac{\partial}{\partial x} \mu^j \left(w_{1,2}^j + w_{2,1}^j \right) \right]$$

$$+ \gamma^j \boldsymbol{w}^j \cdot \boldsymbol{u}_t^j \right\} d\Omega$$

$$= \int_{\partial\Omega_j} \boldsymbol{u}_t^j \cdot \boldsymbol{T}^{(\boldsymbol{w},j)} \boldsymbol{N} d\Gamma - \int_{\Omega_j} \boldsymbol{u}_t^j \cdot \mathcal{L} \boldsymbol{w}^j d\Omega \tag{D.1}$$

$$\int_{\Omega_j} \left[T_{11}^{(\mathbf{u},j)} w_{t1,1}^j + T_{12}^{(\mathbf{u},j)} w_{t1,2}^j + T_{21}^{(\mathbf{u},j)} w_{t2,1}^j + T_{22}^{(\mathbf{u},j)} w_{t2,2}^j - \gamma^j \boldsymbol{w}_t^j \cdot \boldsymbol{u}^j \right] d\Omega_j$$

$$= \int_{\partial\Omega_j} \left[T_{11}^{(\mathbf{u},j)} w_{t1}^j N_x + T_{12}^{(\mathbf{u},j)} w_{t1}^j N_y + T_{21}^{(\mathbf{u},j)} w_{t2}^j N_x + T_{22}^{(\mathbf{u},j)} w_{t2}^j N_y \right] d\Gamma$$

$$- \int_{\Omega_j} \left[T_{11,1}^{(\mathbf{u},j)} w_{t1}^j + T_{12,2}^{(\mathbf{u},j)} w_{t1}^j + T_{21,1}^{(\mathbf{u},j)} w_{t2}^j + T_{22,2}^{(\mathbf{u},j)} w_{t2}^j - \gamma^j \boldsymbol{w}_t^j \cdot \boldsymbol{u}^j \right] d\Omega_j$$

$$= \int_{\partial\Omega_j} \boldsymbol{w}_t^j \boldsymbol{T}^{(\mathbf{u},j)} \boldsymbol{N} d\Gamma - \int_{\Omega_j} \boldsymbol{w}_t^j \cdot \boldsymbol{L} \boldsymbol{u}^j d\Omega_j \tag{D.2}$$

Time derivative of displacements

$$\frac{d}{dt} \boldsymbol{v}^{(j)}(\Gamma(t), t) = \boldsymbol{v}_t^j + \boldsymbol{D}\left(\boldsymbol{v}^j\right) \Gamma_t,$$

$$\boldsymbol{v}_t^{j+1} = \boldsymbol{v}_t^j + \left(\boldsymbol{D}\left(\boldsymbol{v}^j\right) - \boldsymbol{D}\left(\boldsymbol{v}^{j+1}\right)\right) \Gamma_t$$

where $\boldsymbol{v}$ represents both $\boldsymbol{u}$, $\boldsymbol{w}$.

Matrix Manipulations

$$\left(\left(\boldsymbol{D}\left(\boldsymbol{w}^j\right) - \boldsymbol{D}\left(\boldsymbol{w}^{j+1}\right)\right)^T \boldsymbol{T}^{(\boldsymbol{u}^{j+1})} \boldsymbol{N}^j \right) \cdot \boldsymbol{T}^j = \tag{D.3}$$

$$\left(\boldsymbol{N}^j\right)^T \left(\boldsymbol{T}^{(\boldsymbol{u}^{j+1})}\right)^T \left(\boldsymbol{D}\left(\boldsymbol{w}^j\right) - \boldsymbol{D}\left(\boldsymbol{w}^{j+1}\right)\right) \boldsymbol{T}^j$$

$$\left(\left(\boldsymbol{D}\left(\boldsymbol{u}^j\right) - \boldsymbol{D}\left(\boldsymbol{u}^{j+1}\right)\right)^T \boldsymbol{T}^{(\boldsymbol{w}^{j+1})} \boldsymbol{N}^j \right) \cdot \boldsymbol{T}^j =$$

$$\left(\boldsymbol{N}^j\right)^T \left(\boldsymbol{T}^{(\boldsymbol{w}^{j+1})}\right)^T \left(\boldsymbol{D}\left(\boldsymbol{u}^j\right) - \boldsymbol{D}\left(\boldsymbol{u}^{j+1}\right)\right) \boldsymbol{T}^j$$

Bibliography

[1] Abramowitz and Stegun, (1964), Handbook of Mathematical Functions.

[2] Aggelis D.G., Shiotani T.D. and Polyzos D. (2009), Characterization of surface crack depth and repair evaluation using Rayleigh waves, *Cement and Concrete Composites*, Vol. **31**(1), pp. 77-83.

[3] Aki K. (1988), Local site effects on strong ground motion, *Earthquake Engineering and Soil Dynamics* II: Recent Advances in Ground Motion evaluation, J.L. Von Thun (Ed.), Park City, Utah, ASCE, Geotechnical Special Publication, N.20.

[4] Aki K. & Richards P.G. (1980), Quantitative Seismology, Theory and Methods. Freeman, San Francisco.

[5] Assimaki D. and Kausel E. (2007), Modified topographic amplification factors for a single-faced slope due to kinematic soil-structure interaction, *Journal of Geotechnical and Geoenvironmental Engineering*, Vol. **133**(11), pp. 1414-1431.

[6] Bard P.Y. (1982), Diffracted waves and displacement field over two-dimensional elevated topographies, *Geophysical Journal of the Royal Astronomical Society*, Vol. **71**, pp. 731-760.

[7] Bard P.Y. and Gabriel J.C. (1986), The seismic response of two-dimensional sedimentary deposits with large vertical velocity gradients, *Bulletin Of The Seismological Society Of America*, Vol. **76**, pp. 343-366.

[8] Bard P.Y. (1994), Effects of surface geology on ground motion: recent results and remaining issues, *Proceedings of the X European Conference on Earthquake Engineering*, Vienna, Vol. **1**.

[9] Bard P.Y. and Bouchon M. (1985), The two-dimensional resonance of sediment-filled valleys, *Bulletin of the Seismological Society of America*, Vol. **75**, pp. 519-542.

[10] Bard P.Y. and Bouchon M. (1980b), The seismic response of sediment-filled valleys. Part 2. The case of incident P and SV waves, *Bulletin of the Seismological Society of America*, Vol. **70**, pp. 1921-1941.

[11] Bard P.Y. and Bouchon M. (1980a), The seismic response of sediment-filled valleys. Part 1. The case of incident SH waves, *Bulletin of the Seismological Society of America*, Vol. **70**, pp. 1263-1286.

[12] Bertsch C., Cisilino A.P., Calvo N. (2010), Topology optimization of three-dimensional load-bearing structures using boundary elements, *Advances in Engineering Software*, Vol. **41**, pp. 694-704.

[13] Beskos D.E., Leung K.L. and Vardoulakis I.G. (1986), Vibration Isolation of Structures From Surface Waves in Layered Soil, *Recent Applications in Computational Mechanics*, pp. 125-140.

[14] Beskos D.E., Dasgupta B. and Vardoulakis I.G. (1986), Vibration isolation using open or filled trenches, *Computational Mechanics*, Vol. **1**(1), pp. 43-63.

[15] Beskos D.E. (1987), Boundary Element Methods in Dynamic Analysis, *Applied Mechanics Reviews*, Vol. **40**(1).

[16] Boyles C.A. (1984), Acoustic Waveguides, *Applications to Oceanic Science*, John Wiley.

[17] Boore D.M. (1970), Love waves in nonuniform wave guides, *Journal of Geophysical Research*, Vol. **75**, pp. 1512-1527.

[18] Bouchon M. (1985), A simple, complete numerical solution to the problem of diffraction of SH waves by an irregular surface, *Journal of the Acoustical Society of America*, Vol. **77**, pp. 1-5.

[19] Bouckovalas G. and Kouretzis G. (2001), Stiff soil amplification effects in the 7 September 1999 Athens (Greece) earthquake, *International journal of Soil Dynamics and Earthquake Engineering*, Vol. **21**, pp. 671-687.

[20] Bravo M.A. and Sánchez-Sesma F.J. (1988), Seismic response of alluvial valleys for incident P, SV and Rayleigh waves, *International journal of soil dynamics and earthquake engineering*.

[21] Bravo M.A. Sánchez-Sesma F.J. and Chhvez-Garcia F.J. (1988), Ground motion on stratified alluvial deposits for incident SH waves, *Bulletin of the Seismological Society of America*, Vol. **78**, pp. 436-450.

[22] Brebbia C.A. & Dominguez J. (1992), Boundary Elements, An Introductory Course, Witt Press/Computational Mechanics Publications.

[23] Brebbia C.A., Tellers J.C.F. and Wrobel L.C. (1984), Boundary Element Techniques, Springer-Verlag, Berlin.

[24] Carretero L. N., Cisilino A. P. (2008), Topology Optimization of 2D Elastic Structures Using Boundary Elements, *Egineering Analysis with Boundary Elements*, Vol. **32**, pp. 533-544.

[25] Cheng A.H.D., Cheng D.T. (2005), Heritage and early history of the boundary element method, *Engineering Analysis with Boundary Elements*, Vol. **29**, pp. 268-302.

[26] Christensen, R.M. (1971), Theory of Viscoelasticity, Academic Press, New York .

[27] Crichlow J.M., Beckles D. and Aspinal, W.P. (1984), Two-dimensional analysis of the effect of subsurface anomalies on the free surface response to incident SH-waves, *Geophysical Journal of the Royal Astronomical Society*, Vol. **79**, pp. 495-511.

[28] Davis L.L. and West L.R. (1973), Observed effects of topography on ground motion, *Bulletin of the Seismological Society of America*, Vol. **63**, pp. 283298.

[29] De Noyer J. (1961), The effect of variations in layer thickness on Love waves, Bull. *Bulletin of the Seismological Society of America*, Vol. **81**, pp. 227-235.

[30] Dineva P., Manolis G. and Rangelov T. (2004), Transient seismic wave propagation in a multilayered cracked geological region, *Journal of Sound and Vibration*, Vol. **273**1-2), pp. 1-32.

[31] Dobry R. and Vucetic M. (1987), Dynamic Properties and Seismic Response of Soft Clay Deposits, *International Symposium on Geotechnical Engineering of Soft Soils*, Mexico City, Vol. **2**, pp. 51-87.

[32] Dominguez J. and Abascal R. (1984), On fundamental solutions for the boundary integral equations method in static and dynamic elasticity, *Engineering Analysis*, Vol. **1**(3), pp. 128-134.

[33] Dominguez J. and Meise T. (1991), On the use of the BEM for wave propagation in infinite domains, *Engineering Analysis with Boundary Elements*, Vol. **8**(3), pp. 132-138.

[34] Dominguez J. (1993), Boundary Elements in Dynamics. Computational Mechanics Publications and Elsevier Applied Science.

[35] Dravinski M. (2009), Influence of Cylindrical Harmonic SH Waves on Motion along a Random Interface between Two Elastic Half-Spaces, *Bulletin of the Seismological Society of America*, Vol. **99**(4), pp. 2582-2588.

[36] Dravinski M. (2007), Scattering of Waves by a Sedimentary Basin with a Corrugated Interface, *Bulletin of the Seismological Society of America*, Vol. **97**(1B), pp. 256-264.

[37] Dravinski M. (1983), Scattering of Plane Harmonic SH Waves By Dipping Layers of Arbitrary Shape, *Bulletin of the Seismological Society of America*, Vol. **73**(5), pp. 1303-1319.

[38] Dravinski M. and Moessian T.K. (1987), Scattering of Plane Harmonic P, SV and Raileigh Waves By Dipping Layers of Arbitrary Shape, *Bulletin of the Seismological Society of America*, Vol. **77**(1), pp. 212-235.

[39] Emad K. and Manolis G.D. (1985), Shallow Trenches and Propagation of Surface Waves, *Journal orf Mechanical Engineering*, Vol. **111**(2), pp. 279-282.

[40] Eringen A. C. and Suhubi E.S. (1975), Elastodynamics, Academic Press NY, Vol. **2**.

[41] Fawcett J. A. (1992), A derivation of the di erential equations of coupled-mode propagation, *Journal of the Acoustical Society of America*, Vol. **92**, pp. 290-295.

[42] Foda, A.M. and Yuh-Huei Chang, Y.H. (1995), Faraday resonance in thin sedimentary layers, *Geophysical Journal International*, Vol. **123**, pp. 559-571.

[43] Foti S. (2000), Multistation Methods for Geotechnical Characterization using Surface Waves, Ph.D. Dissertation presented at Politecnico di Torino.

[44] Fujiwara H. and Takenaka H. (1994), Calculation of surface waves for a thin basin structure using a direct boundary element method with normal modes, *Geophysical Journal International*, Vol. **117**, pp. 69-91.

[45] Geli L., Bard P.Y. and Julien B. (1988), The effect of topography on earthquake ground motion: a review and new results, *Bulletin of the Seismological Society of America*, Vol. **78**, pp. 4263.

[46] Gjevik, B. (1973), A Variational Method For Love Waves In Nonhorizzontally Layered Structures, *Bulletin of the Seismological Society of America*, Vol. **63**(3), pp. 1013-1023.

[47] Goldstein, H. (1980), Classical Mechanics, Addison-Wesley Publishing Company, 2nd Ed., pp. 672.

[48] Griffiths D.W. and Bollinger G.A. (1979), The effect of Appalachian mountain topography on seismic waves, *Bulletin of the Seismological Society of America*, Vol. **69**, pp. 1081-1105.

[49] Guzina B. B. and Chikichev I. (2006), From Imaging to material identification: A generalized concept of topological sensitivity, *Journal of the Mechanics and Physics of Solids*, Vol. **55**, pp.245-279.

[50] Guzina B. B. and Bonnet (2004), Topological Derivative for the Inverse Scattering of Elastic Waves, *Quaterly Journal Mechanics Appllied Mathematics*, Vol. **57**(2), pp.161-179.

[51] Graffi D. (1946-1947), Sul Teorema di Reciprocita nella Dinamica dei Corpi Elastici, *Memorie della Reale Accademia delle Scienze*, Vol. **4**, pp 103-109.

[52] Gucunski N. and Wood R.D. (1992), Numerical simulation of SASW test, *Soil Dynamics and Earthquake Engineering*, Vol. **11**(4), pp. 213-227.

[53] Heisey J. S., Stokoe K. H. II, Meyer A. H. (1982), Moduli of pavement systems from spectral analysis of surface waves, *Transportation research record*, Vol. **852**, pp. 22- 31.

[54] Hador R. B. and Buchen P. (1999), Love and Rayleigh waves in non-uniform media, *Geophysical Journal International*, Vol. **137**, pp. 521-534.

[55] Hardin B.O. (1978), The Nature of Stress-Strain Behavior of Soils, *Earthquake Engeneering and Soil Dynamics*, Vol. **1**, pp. 3-89.

[56] Herrmann R.B. (1996), Computer programs in seismology: an overview on synthetic seismogram computation, Users manual, StLouis University, Missouri.

[57] Hudson J. A. (1967), Scattered surface waves from a surface obstacle, *Geophysical Journal of the Royal Astronomical Society*, Vol. **13**, pp. 441458.

[58] Idriss I.M., Lysmer J., Hwang R. and Seed H.B. (1973), A Computer Program for Evaluating the Seismic Response of Soils Structures by Variable Damping Finite Elements, Earthquake Engineering Research Center, Report No. EERC 73-16, University of California, Berkeley.

[59] Ishibashi I. and Zhang X. (1993), Unified DynamicShear Moduli and Damping Ratios of Sand and Clay, *Soils and Foundations*, Vol. **33**(1), pp. 182-191.

[60] Kamalian M., Gatmiri B., Sohrabi-Bidar A. and Khalaj A. (2007), Amplification pattern of 2D semi-sine-shaped valleys subjected to vertically propagating incident waves, *Communications in Numerical Methods in Engineering*, Vol. **23**(9), pp. 871-887.

[61] Katsikadelis J.T. (2002), Boundary Elements: Theory and Applications, Elsevier Science, ISBN: 0080441076.

[62] Kausel E. and Roesset J. M. (1981), Stiffness matrices for layered soils, *Bulletin Of The Seismological Society Of America*, Vol. **71**, pp. 1743-1761.

[63] Kausel E. and Joonsang Park J. (2006), Response of Layered Half-Space Obtained Directly in the Time Domain, Part II: SV-P and Three-Dimensional Sources, *Bulletin of the Seismological Society of America*, Vol. **96**(5), pp. 1810-1826.

[64] Kennett B. L. N. and Engdahl E. R. (1991), Travel times for global earthquake location and phase identification, *Geophysical Journal International*, Vol. **105**, pp. 429-465.

[65] Kennett B. L. N., Koketsu K. and Haines A.J. (1990), Propagation invariants, reflection and transmission in anisotropic, laterally heterogeneous media, *Geophysical Journal International*, Vol. **103**, pp.95-101.

[66] Kennett B. L. N. (1986), Wavenumber and wavetype coupling in laterally heterogeneous media, *Geophysical Journal of the Royal Astronomical Society*, Vol. **87**, pp. 313-331.

[67] Kennett B. L. N. (1981-1983), Seismic Wave Propagation in Stratified Media, Cambridge University Press.

[68] Kennett B. L. N. (1979), Seismic waves in stratified half space, *Geophysical Journal of the Royal Astronomical Society*, Vol. **57**, pp. 557-583.

[69] Kennett B. L. N. (1974), Reflections, rays and reverberations, *Bullettin of the Seismological Society of America*, Vol. **64**(6), pp. 1685-1696.

[70] Kennet N. (1972), Seismic Wave Scattering by Obstacles on Interfaces, *Geophysical Journal of the Royal Astronomical Society*, Vol. **28**, pp. 249-266.

[71] Kerry N. J. (1981), Synthesis of seismic surface waves, *Geophysical Journal of the Royal Astronomical Society*, Vol. **64**, pp. 425-446.

[72] King J. and Tucker B.E. (1984), Observed variations of earthquake motion across a sediment-filled valley, *Bulletin of the Seismological Society of America*, Vol. **74**, pp. 137-151.

[73] Kitahara M. (1984), Applications of Boundary Integral Equation Methods to Eigenvalue Problems of Elastodynamic and Thin Plates, University of Kyoto.

[74] Knopoff L. and Mal A.K. (1967), Phase velocity of surface waves in the transition zone of continental margins, *Journal of Geophysical Research*, Vol. **72**, pp. 1769-1776.

[75] Jamilkowski M., Leroueil S. and Lo Presti D.C.F. (1991), Theme Lecture: Design Parameters from Theory to Practice, *Proceedings, Geo-Coast-91*, Yokohama, Japan, pp. 1.

[76] Jeffreys H. and Jeffreys, B.S. (1972), Methods of Mathematical Physics, 3Rd. Ed. Cambridge University Press.

[77] Lai C.G. (1998), Simultaneous Inversion of Rayleigh Phase Velocity and Attenuation for Near-Surface Site Characterization, Ph.D. Dissertation.

[78] Lanzo G. and Silvestri F. (1999), Risposta sismica Locale. Teoria ed esperienze, Hevelius Editore.

[79] Lo Presti D.C.F. and Pallara O. (1997), Damping Ratio of Soils from Laboratoryand In-Situ Tests. Proceedings of the 14^{Th} *International Conference on Soil Mechanics and Foundation Engineering*, Hamburg, Germany, pp. 6-12.

[80] Lo Presti D.C.F., Jamilkowski M., Pallara O. and Cavallaro A. (1996), Rate and Creep Effect On the Stiffness of Soils. *Proceedings of the Conference on Measuring and Modeling Time Dependent Soil Behavior*, Held in Conjuction with ASCE National Convention, Washinton, D.C.

[81] Louie N.J. (2001), Faster, Better: Shear-Wave Velocity to 100 Meters Depth From Refraction Microtremor Arrays, *Bulletin of the Seismological Society of America*, Vol. **91**(2), pp. 347-364.

[82] Lysmer J. and Drake L.A. (1971), The propagation of love waves across non-horizzontally layered structures, *Bulletin of the Seismological Society of America*, Vol. **61**(5), pp. 1233-1251.

[83] Manolis G.D. and Beskos D.E.(1981), Dynamic stress concentration studies by boundary integrals and Laplace transform, *International Journal for Numerical Methods in Engineering*, Vol. **17**(4), pp. 573-599.

[84] Manolis G.D. and Beskos D.E. (1983), Dynamic response of lined tunnels by an isoparametric boundary element method, *Computer Methods in Applied Mechanics and Engineering*, Vol. **36**(3), pp. 291-307.

[85] Manolis G.D. and Beskos D.E. (1988), Boundary Element Methods in Elastodynamics, Unwin Hyman Ltd.

[86] Maupin V. (2007), Introduction to mode coupling methods for surface waves, *Advances in Geophysics*, Vol. **48**, pp. 127-155.

[87] Maupin V. and Kennett B.L.N. (1987), On the use of truncated modal expansions in laterally varying media, *Geophysical Journal of the Royal Astronomical Society*, Vol. **91**, pp. 837-851.

[88] Menke W. (1989), Geophysical Data Analysis: Discrete Inverse Theory, revised edition; Academic Press. *International Geophysics Series*, Vol. **45**, ISBN 0-12-490921-3.

[89] Mucciarelli M., Dusi A. e Dusi C. (1998), GNGTS, *Atti del 17 convegno nazionale*, Vol. **02.11**.

[90] Mogi H. and Kawakami H. (2007), Analysis of Scattered Waves on Ground with Irregular Topography Using the Direct Boundary Element Method and Neumann Series Expansion, *Bulletin of the Seismological Society of America*, Vol. **97**(4), pp. 1144-1157; DOI: 10.1785/0120060178.

[91] Nazari A., Baziar M.H. and Shahnazari H. (2010), Seismic Effects of Two-Dimensional Semi-Sine Shaped Hills on Ground Motion Response, *The Electronic Journal of Geotechnical Engineering*, Vol. **15**(L).

[92] Nazarian S. and Stokoe K.H. In situ shear wave velocity from spectral analysis of surface waves, *Proceedings of the* 8^{Th} *Conference on Earthquake engineering*, St. Francisco, Vol. **3**, Prentice Hall, pp. 31-38.

[93] Novotny A.A., Feijoo R.A., Taroc E., Padra C.C. (2003), Topological sensitivity analysis, *Computer Methods Applied Mechanics Engineering*, Vol. **192**(7-8), pp. 803-829.

[94] Park C.B., Miller R.D. and Xia J. (1999), Multi-Channels analysis of surface waves, *Geophysics*, Vol. **64**(3), pp. 800-808.

[95] Park C.B., Miller R.D. and Xia J. (1997), Multi-Channels analysis of surface waves: A summary report of technical aspects, esperimental results, and perspective, *Kansas Geological Survey*.

[96] Park C.B. and Ryden N. (2007), Historical overview of the surface wave method, *Proceedings of the Symposium on the Application of Geophysics to Engineering and Environmental Problems* (SAGEEP 2007), Denver, CO, pp 897-909.

[97] Pierce A.D. (1965), Extension of the method of normal modes to sound propagation in an almost stratified medium, *Journal of the Acoustical Society of America*, Vol. **37**, pp. 19-27.

[98] Piwakowski B., Goueygou M., Fnine A. and Buyle-Bodin F. (2004), P-τ transformation as the efficient tool for determination of the velocity dispersion characteristics in complex structures, 16^{Th} *World Conference on NDT*, Montreal, Canada.

[99] Portela A., Aliabadi M.H. and Rooke D.P.(1992), The Dual Boundary Element Method: Effective Implementation For Crack Problems, *International Journal for Numerical Methods in Engineering*, Vol. **33**, pp. 1269-1287.

[100] Porter D. and Staziker D.J. (1995), Extension of the mild-slope equation, *Journal of Fluid Mechanics*, Vol. **300**, pp.367-382.

[101] Porter D. and Chamberlain P G. (1997), Linear wave scattering by two-dimensional topography.

[102] Rangelov T., Dineva P. and Gross D. (2003), A hyper-singular traction boundary integral equation method for stress intensity factor computation in a finite cracked body, *Engineering Analysis with Boundary Elements*, Vol. **27**(1), pp. 9-21.

[103] Raptakis D., Chavez-Garcia F.J., Makra K. and Pitilakis K. (2000), Site effects at Euroseistest-I, Determination of the valley structure and confrontation of observations with 1D analysis, *Soil dynamics and Earthquake Engineering*, Vol. **19**(1), pp. 1-22.

[104] Rayleigh J.W.S., (1985), On waves propagated along the plane surface of an elastic solid, *Proceedings of the London Mathematical Society*, Vol. **17**, pp. 4-11.

[105] Richart F.E. Jr, Wood R.D., Hall J.R. (1970), Vibration of soils and foundations, Prentice-Hall, New Jersey.

[106] Rix G.J., Lai C.G. and Foti S. (2001), Simultaneous Measurement of Surface Wave Dispersion and Attenuation Curves, *Geotechnical Testing Journal*, Vol. **24**(4), pp. 350-358.

[107] Rix G.J., Lai C.G. and Spang A.W. (2000), In Situ Measurement of Damping Ratio Using Surface Waves, *Journal of Geotechnical and Geoenvironmental Engineering*, Vol. **126**(5), pp. 472-480.

[108] Rix G. J., Lai C. G. (1998), Simultaneous inversion of surface wave velocity and attenuation, Geotechnical Site Characterization, Robertson & Mayne eds, Vol. **1**, Balkema, pp. 503-508.

[109] Roesset J. M., Chang D. W., Stokoe K. H. (1991), Comparison of 2-D and 3-D models for analysis of surface wave tests, *Prooceedings of the 5^{Th} International Conference on Soil Dynamic and Earthquake Engineering*, Kalsruhe, Vol. **1**, pp. 111-126.

[110] Ryden N. and Lowe M. (2004), Guided wave propagation in three-layer pavement structures, *Journal of the Acoustical Society of America*, Vol. **116**(5), pp. 2902-2913.

[111] Ryden N., Park C.B., Ulriksen P. and Miller R.D. (2004), Multimodal approach to seismic pavement testing, *Journal of Geotechnical and Geoenvironmental Engineering*, Vol. **130**(6), pp. 636-645.

[112] Ryden N., Park C.B., Ulriksen P. and Miller R.D. (2003), Lamb wave analysis for non-destructive testing of concrete plate structures, *Proceedings of the Symposium on the Application of Geophysics to Engineering and Environmental Problems* (SAGEEP 2003), San Antonio, TX.

[113] Sabina F.J., and Willis J.R. (1975), Scattering of SH waves by a rough half-space of arbitrary slope, *Geophysical Journal of the Royal Astronomical Society*, Vol. **42**, pp. 685703.

[114] Sánchez-Sesma F.J. and Luzón F. (1995), Seismic response of three-dimensional alluvial valleys for incident P, S and Rayleigh waves, *Bulletin of the Seismological Society of America*, Vol. **85**, pp. 269-284.

[115] Sánchez-Sesma F.J., Campillo M. (1993), Topographic effects for incident P, SV and Rayleigh waves, *Tectonophysics*, Vol. **218** pp. 113125.

[116] Sánchez-Sesma F.J. and Peréz-Rocha L.E. (1989), Diffraction of Elastic Waves by Three-Dimensional Surface Irregularities. Part II, *Bulletin of the Seismological Society of America*, Vol. **79**(1), pp. 101-112.

[117] Sánchez-Sesma F.J., Campillo M. and Irikura K. (1989), A note on the Rayleigh Hypotesis and The Aki-Larner Method, *Bulletin of the Seismological Society of America*, Vol. **79**(6), pp. 1995-1999.

[118] Sánchez-Sesma F.J., Bravo M.A. and Herrera I. (1985), Surface Motion Of Popographical Irregularities For Incident P, SV and Rayleigh Waves, *Bulletin of the Seismological Society of America*, Vol. **75**(1), pp. 263-269.

[119] Sánchez-Sesma F.J. and Esquivel J.A. (1979), Ground motion on alluvial valleys under incident plane SH waves, *Bulletin of the Seismological Society of America*, Vol. **69**, pp. 1107-1120.

[120] Savage W.Z. (2004), An Exact Solution for Effects of Topography on Free Rayleigh Waves, *Bulletin of the Seismological Society of America*, Vol. **94**(5), pp. 1706-1727.

[121] Schnabel B., Lysmer J. and Seed H. (1972), SHAKE: a computer program for earthquake response analysis of horizontally layered sites. Rep. E.E.R.C. 70-10, Earthquake Engineering Research Center, Univ. California, Berkeley.

[122] Sheriff R.E. and Geldart L.P. (1995), Exploration seismology, University Press, Cambridge.

[123] Shibuya S., Mitachi T., Fukuda F. and Degoshi T. (1995), Strain Rate Effects on Shear Modulus and Damping of Normally Consolidated Clay, *Geotechnical Testing Journal*, Vol. 1**8**(3), pp.365-375.

[124] Shi-Zhe Xu (2001), The Boundary Element Method in Geophysics. Society Of Exploration Geophysicists.

[125] Socco L.V., Foti S., and Boiero D. (2010), Surface-Wave analysis for building near-surface velocity models - Established approaches and new perspectives, *Geophysics*, Vol. **75**(5), pp. 83-102.

[126] Boiero D. and Socco L.V. (2010), Retrieving lateral variations from surface wave dispersion curves, *Geophysical Prospecting*, Vol. **58**, pp. 977-996.

[127] Stokoe K.H. II, Wright S.G., Bay J.A. and Roesset J.M. (1994), Characterization of geotechnical sites by SASW method, Geophysical Characterization of Sites (ISSMFE TC#10) by R.D. Woods, Oxford & IBH Publ., pp. 15-25.

[128] Strobbia C., Surface Wave Methods, Acquisition, processing and inversion. Ph. D. Dissertation presented at Politecnico di Torino.

[129] Strobbia C. and Foti S. (2006), Multi-offset phase analysis of surface wave data (MOPA), *Journal of Applied Geophysics*, Vol. **59**, pp. 300-313.

[130] Tadeu A.J.B., Santos P.F.A. and Kausel E. (1999), Closed-form integration of singular terms for constant, linear and quadratic boundary elements. Part 1. SH wave propagation, *Engineering Analysis with Boundary Elements*, Vol. **23**(8), pp. 671-681.

[131] Tadeu A.J.B., Santos P.F.A. and Kausel E. (1999), Closed-form integration of singular terms for constant, linear and quadratic boundary elements. Part 2. SV-P wave propagation, *Engineering Analysis with Boundary Elements*, Vol. **23**(9), pp. 757-768.

[132] Tarantola, A. (1987), Inverse problem theory: Methods for data fitting and model parameter estimation, Elsevier, ISBN 0444427651.

[133] Tikhonov A.N., and Arsenin V.Y.(1977), Solution of ill-posed problems: V. H. Winston and Sons.

[134] Tokimatsu K., Shinzawa K., Kuwayama S. (1992a), Use of short-period microtremors for Vs profiling, *Journal of Geotechnical Engineering*, Vol. **118**(10), pp. 1544-1558.

[135] Tokimatsu K., Tamura S., Kojima H. (1992b), Effects of multiple modes on Rayleigh wave dispersion characteristics, *Journal of Geotechnical Engineering*, Vol. **118**(10), pp. 1529-1543.

[136] Trefethen, L.N. (2000), Spectral Methods in MATLAB, SIAM Philadelphia.

[137] Trifunac M.D. (1971), Surface motion of a semi-cylindrical alluvial valley for incident plane SH waves, *Bulletin of the Seismological Society of America*, Vol. **61**, pp. 1755-1770.

[138] Tselentis G.A. and Delis G. (1988), Rapid assessment of S-waves profiles from the inversion of multichannel surface data, *Annali di Geofisica*, Vol. **41**(1).

[139] Viktorov I. A. (1967), Rayleigh and Lamb Waves: physical theory and applications, Plenum Press, New York.

[140] Vucetic M. and Dobry R. (1991), Effect of Soil Plasticity on Cyclic Response, *Journal of Geotechnical Engineering*, Vol. **117**(1), pp. 89-107.

[141] Vucetic M. (1994), Cyclic Threshold Shear Strain in Soil, *Journal of Geotechnical Engineering*, Vol. **120**(12), pp. 2208-2228.

[142] Wheeler L.T. and Sternberg E. (1938), Some Theorems in Classical Elastodynamics. *Archive for Rational Mechanics and Analysis*, Vol. **31**(1), pp 51-90, DOI: 10.1007/BF00251514.

[143] Whitham G.B. (1965), A general approach to linear and nonlinear dispersive waves using a Lagrangian, *Journal of Fluid Mechanics*, Vol. **22**, pp. 273-283.

[144] Whitham G.B. (1967), Variational methods and applications to water waves, *Proceedings of the London Mathematical Society*, Ser. A., Vol. **299**(6).

[145] Whitham G.B. (1967), Non-linear dispersion of water waves, *Journal of Fluid Mechanics*, Vol. **27**, pp. 399-412.

[146] Williams T.P., Gucunski N. (1995), Neural networks for backcalculation of moduli from SASW test, *Journal of Computing in Civil Engineering*, Vol. **9**(1) pp. 1-8.

[147] Wolf B. (1970), Propagation of Love waves in layers with irregular boundaries, *Pure Applied Geophysics*, Vol. **78**, pp. 48-57.

[148] Wong H.L., Trifunac M.D. (1974), Surface motion of a semi-elliptical alluvial valley for incident plane SH-waves, *Bulletin of the Seismological Society of America*, Vol. **64**(5), pp. 13891408.

[149] Wong H.L. (1982), Effects of Surface Topography on the Diffraction of P S_V and Rayleigh Waves, *Bulletin of the Seismological Society of America.* Vol. **72**(4), pp. 1167-1183.

[150] Yu C.W. and Dravinski M. (2009), Scattering of plane harmonic P, SV or Rayleigh waves by a completely embedded corrugated cavity, *Geophysical Journal International*, Vol. **178**(1), pp. 479-487.